Molecular-Level Approaches to Photosensitive Nanostructured Materials: High-Dimensional Quantum Dynamics and Kinetic Monte Carlo Simulations

Dissertation
zur Erlangung des Doktorgrades
der Naturwissenschaften

vorgelegt beim Fachbereich 14
der Johann Wolfgang Goethe-Universität
in Frankfurt am Main

von

Matthias Alexander Polkehn

aus

Hanau

Frankfurt am Main
2017

(D30)

vom Fachbereich 14 Biochemie, Chemie und Pharmazie
der Johann Wolfgang Goethe - Universität als Dissertation angenommen.

Dekan: Prof. Dr. Michael Karas
Gutachter: Prof. Dr. Irene Burghardt
Prof. Dr. Stefan Haacke

Datum der Disputation: .....

Abstract

The development of novel functional materials is a complex task, since the overall device performance is based on a variety of adjustable parameters. Given that the functionalisation at the molecular level via chemical engineering plays an as important role as the macromolecular arrangement in the bulk material, the question for an improvement of current generation nanomaterials cannot be addressed solely by one research area, or by either experiment or modeling. Therefore, this thesis presents complementary approaches to understand both the microscopic and mesoscopic aspects of novel functional nanostructured materials. The common denominator is our goal to characterize charge separation processes that drive the generation of electric currents in organic photovoltaic devices.

The relevant charge separation processes are often described in terms of the dissociation of an exciton, i.e., a bound electron-hole pair which is created within the donor domain of a donor-acceptor material. This process is highly sensitive to the material's nanomorphology, e.g., in so-called bulk heterojunction architectures. Therefore, it is necessary to investigate the effect of intermolecular interactions, both at the electronic-structure level and within dynamical treatments. This applies both to quantum dynamical approaches that are necessary at the shortest time scales, and to statistical methods that are suitable to describe the longer-time evolution.

In order to study the initial exciton dissociation step which is often ultrafast and coherent, a combination of (i) high-level *ab initio* and time-dependent density functional theory (TDDFT) electronic structure methods serving to parametrise a suitable model Hamiltonian, and (ii) the Multi-Configuration Time-Dependent Hartree (MCTDH) method and its multi-layer (ML-MCTDH) variant have been used. The MCTDH method is a powerful quantum dynamical method which typically allows the treatment of up to 100 full quantum degrees of freedom; the hierarchical ML-MCTDH approach can even go significantly

beyond this. The parametrisation of the model Hamiltonians upon which the quantum dynamical treatment is based has been carried out for small fragments of the overall material. These fragments are chosen such as to represent the relevant intramolecular and intermolecular interactions, while allowing as far as possible a high-level *ab initio* characterisation with electronic structure methods in a reasonable amount of time.

With the aid of these methods, two types of functional organic systems were studied. First, a novel donor-acceptor material composed of self-assembled oligothiophene-perylene block co-oligomers, synthesised and spectroscopically investigated in the groups of S. Haacke and S. Méry at Strasbourg University. The quantum dynamical simulations done on this system served to rationalize the results obtained from time-resolved pump-probe spectroscopy, and explain the lack of efficiency of this system. In particular, it could be shown that after exciton dissociation, the electron and hole remain on adjacent donor and acceptor molecules, leading to a spatial confinement of oppositely charged carriers and eventually to recombination. Second, a model for the well-known P3HT-PCBM material, i.e., a combination of poly(3-hexylthiophen-2,5-diyl) donor and [6,6]-phenyl C_{61} butyric acid methyl ester acceptor, was studied. Building upon a lattice model that was previously developed in our group, we focus here on the inclusion of charge transfer exciton states in the donor domain. The importance of such charge-separated species in regioregular oligothiophene assemblies has recently been highlighted in several experimental studies. Besides the description of the generation of charge-transfer excitons, our study is aimed at quantifying the influence of these pre-dissociated electron hole pairs on the charge separation between donor and acceptor species and on free carrier generation. This aspect of charge separation at P3HT-PCBM heterojunctions is here studied for the first time.

A second-generation block-co-oligomer donor-acceptor system designed by the Strasbourg group is found to be more efficient than the first generation mentioned above, but the charge transfer falls into a slower time regime around tens to hundreds of picoseconds. Therefore, Kinetic Monte Carlo (KMC) methods were used to address the charge separation process. To this end, a Fortran90 code has been developed, which uses the *First Reaction Method* algorithm to solve the relevant master equation. Additional information about the delocalisation of the exciton has also been integrated into the KMC code, beyond conventional implementations. It has been found that this delocalisation effectively lowers the energetic barrier for free charge carrier generation and hence, delocalisation raises the

overall power conversion efficiency. First simulations done with this code on idealised and randomly generated donor-acceptor morphologies have been carried out successfully, yielding realistic values for microscopic observables like charge carrier mobilities. Furthermore, simulations on a coarse-grained structure of the second-generation block-co-oligomer system designed by the Strasbourg group have been carried out, in view of investigating charge carrier mobility.

Zusammenfassung

Die Entwicklung von neuartigen, funktionellen Materialien ist eine komplexe Aufgabe, da die Gesamteffizienz der zu entwickelnden Materialien von einer Vielzahl von Faktoren abhängt. Während die auf einer molekularen Ebene durchgeführte Funktionalisierung via chemischer Reaktionsführung genauso wichtig ist wie die makromolekulare Anordnung, kann die Frage nach einer geeigneten Verbesserung von gegenwärtigen Materialien nicht nur auf einer dieser beiden Ebenen beantwortet werden. Die in dieser Arbeit präsentierten Ergebnisse basieren auf der mirkoskopischen aber auch markoskopischen Betrachtung von neuartigen, funktionellen Nanomaterialien und den daraus gewonnenen Erkenntnissen. Das übergeordnete Ziel ist dabei das Verständnis und die Charakterisierung von Ladungsseparationsprozessen und die daraus resultierende Erzeugung von elektrischen Strömen in organischen photovoltaischen Materialien.

Die relevanten Ladungsseparationsprozesse werden oft im Kontext der Dissoziation von Exzitonen, gebundenen Elektron-Loch Paaren, beschrieben, welche innerhalb der Donordomäne eines beliebigen Donor-Akzeptor-Materials erzeugt werden. Dabei ist der Prozess der Exzitonengenerierung abhängig von der Nanomorphologie des entsprechenden Materials, typischerweise so genannten Bulk-Heterojunctions. Dahingehend ist es notwendig, die Effekte von intermolekularen Wechselwirkungen sowohl mittels quantenmechanischer als auch dynamischer Methoden zu betrachten. Um alle relevanten Zeitskalen und Prozesse zu betrachten ist es weiterhin notwendig, auf sowohl eine deterministische Darstellung im Rahmen von quantendynamischen Methoden als auch statistischen Methoden zurückzugreifen.

Um die oft ultraschnellen und kohärenten Exzitonendissoziationsprozesse zu untersuchen wurde eine Kombination aus high-level *ab initio* Methoden und zeitabhängiger Dichtefunktionaltheorie (TDDFT) angewandt, um geeignete Modellhamiltonians zu parametrisieren, welche schließlich mittels der Multi-Configurational Time-Dependent Hartree

(MCTDH) und der Multilayer (ML-MCTDH) variante propagiert wurden. Die MCTDH Methode hat sich als geeignete Methode erwiesen um eine voll quantendynamische Beschreibung von bis zu 100 Freiheitsgraden durchzuführen; die ML-MCTDH Methode erlaubt gar bis zu 1000 Freiheitsgrade quantendynamisch zu behandeln. Die Parametrisierung der Modellhamiltonians, auf welchen die quantendynamische Behandlung basiert, wurde dabei für kleine, jedoch repräsentative Fragmente durchgeführt. Die geeignete Wahl dieser Fragmente sollte sicherstellen, dass zum einen alle relevanten intermolekularen als auch intramolekularen Wechselwirkungen enthalten sind, jedoch gleichzeitig eine möglichst akkurate Beschreibung mittels high-level elektronenstrukturtheoretischer Methoden in gegebener Zeit möglich ist.

Mit Hilfe dieser Methodenkombination wurden zwei Arten von funktionellen organischen Materialien untersucht. Das erste untersuchte System ist ein neuartiges Donor-Akzeptor System, bestehend aus selbstorganisierenden Oligothiophen-Perylenediimid Dimeren, welche in der Gruppe von S. Haacke und S. Méry der Universität Straßburg synthetisiert und spektroskopisch untersucht wurden. Die quantendynamischen Simulationen an diesem System sollten die Ergebnisse der experimentellen, zeitaufgelösten pump-probe Spektroskopie validieren und die dürftige Effizienz im Hinblick auf eine effektive Ladungstrennung erklären. Dabei konnte gezeigt werden, dass nach der Exzitonendissoziation Elektron und Loch auf räumlich benachbarten Donor- und Akzeptorfragmenten lokalisiert werden, was schließlich zu einem Rekombinationsprozess führen wird. Das zweite untersuchte System ist eine Kombination von Poly(3-Hexylthiophen-2,5-diyl) (P3HT) als Elektronendonor und [6,6]-Phenyl-C_{61} Butansäure Methyl-Ester (PCBM) als Elektronenakzeptor, welches schon hinreichend stark in diversen theoretischen und experimentellen Studien untersucht wurde. Aufbauend auf einem Gittermodell, welches in unserer Gruppe entwickelt wurde, wurde das Modellsystem um Charge Transfer Exzitonen in der Donordomäne erweitert. Die Bedeutung von solchen Charge Transfer Exzitonen in regioregulären Oligothiophenaggregaten ist ein aktuelles Thema in der Wissenschaft, sowohl in experimentellen aber auch theoretischen Abhandlungen. Neben der theoretischen Beschreibung zur Entstehung solcher Charge Transfer Exzitonen liegt ein besonderes Augenmerk auf dem Einfluss dieser predissoziierten Elektron-Loch Paaren auf die Ladungsseparationsdynamik zwischen Donor und Akzeptor sowie die Generierung von freinen Ladungsträgern. Dieser Aspekt der Ladungsseparation in einem P3HT-PCBM System wurde in dieser Art und Weise in dieser

Arbeit zum ersten mal untersucht.

Neben dem zuvor erwähnten Donor-Akzeptor System erster Generation der Universität Straßburg wurde eine zweite Variante dieses Systems entwickelt, welches sich bei bisherigen experimentellen Untersuchungen als wesentlich effizienter erwies. Der interessante Prozess der Ladungsseparation ist dabei allerdings auf einer Zeitskala von mehreren hundert Pikosekunden angesiedelt, sodass kinetische Monte Carlo Methoden verwendet werden mussten um diese Prozesse zu modellieren. Dazu wurde ein Fortran90 Code entwickelt, welcher den *First Reaction Method* Algorithmus verwendet und explizite Delokalisationsprozesse behandelt, welche in dieser Form in kommerziellen Programmpaketen nicht enthalten ist. In vorangehenden Arbeiten konnte gezeigt werden, dass die Delokalisation von Exzitonen zu einer effektiven Herabsetzung der energetischen Barriere der Ladungsseparation führt und somit die Effizienz zur Stromumwandlung gesteigert werden konnte. Erste Simulationen mit diesem Code an idealisierten und zufällig generierten Donor-Akzeptor Morphologien lieferten realistische Werte für makroskopische Observablen wie Ladungsträgermobilitäten. Weiterhin wurden Simulationen einer coarse-grained Struktur zur zweiten Generation des Donor-Akzeptor Systems durchgeführt, ebenfalls mit Hinblick zur Untersuchung der Ladungsträgermobilität.

Contents

List of Figures

List of Tables

List of Abbreviations

3PEPS 3 Pulse Photon Echo Peak Shift

ADC2 Algebraic Diagrammatic Construction to Second Order

BHJ Bulk Heterojunction

CC Coupled Cluster

CCLR Coupled Cluster Linear Response

CS Charge Separated

CT Charge Transfer

DA Donor-Acceptor

(TD)DFT (Time-dependent) Density Functional Theory

DOF Degree of Freedom

e-h electron-hole

EET Excitation Energy Transfer

EM Effective mode

EOM-CC Equations of Motion Coupled Cluster

ES Exctied State

eV electron Volt

FRET Foerster resonance energy transfer

FRM First Reaction Method

fs femto second

GS Ground state

HF Hartee Fock

HOMO Highest Occupied Molecular Orbital

ISR Intermediate State Representation

KMC Kinetic Monte Carlo

LUMO Lowest Unoccupied Molecular Orbital

LVC Linear Vibronic Coupling

(ML)MCTDH (Multi-Layer) Multi-configuration time-dependent Hartree

MEH-PPV poly[2-methoxy-5-(2'-ethylhexyloxy)-p-phenylene vinylene]

MP Moeller-Plesset

NM Normal mode

OT-4 Oligothiophene tetramer

P3HT Poly(3-hexylthiophen-2,5-diyl)

PCBM [6,6]-phenyl-C61- butyric acid methyl ester

ps pico second

RR Regioregular

RRa Regiorandom

SHF Single Hole Function

SPF Single Particle Function

SVP Single Valence Polarisation

TDH Time-dependent Hartree

TDSE Time-dependent Schroedinger Equation

TISE Time-independent Schroedinger Equation

TTAD Two-Time Anisotropy Decay

XT Exciton

1 — Deutsche Zusammenfassung

Der steigende Energieverbrauch der Weltwirtschaft sowie der immer weiter ansteigende Gehalt an Kohlendioxid in der Atmosphäre und der damit einhergehenden Erderwärmung hat zu einer verstärkten Wahrnehmung über die Folgen einer stark globalisierten und industrialisierten Welt geführt. Gleichwohl steigt das Interesse an der Verwendung und auch die wirtschaftliche Umsetzbarkeit von regenerativen Energien im Alltag immer weiter an. So sind Automobile mit einem Hybridantrieb, also einer Kombination aus konventionellem Verbrennungsmotor und emissionsfreiem Elektromotor, aus dem heutigen Alltag nicht mehr weg zu denken. Steigende Rohstoffpreise für fossile Brennstoffe sowie deren Verknappung in naher Zukunft führen zu einem großen allgemeinen und wissenschaftlichen Interesse an alternativer und emissionsfreier Energiegewinnung. Der Vorteil von regenerativer und alternativer Energiegewinnung liegt in den geographischen Begebenheiten der jeweiligen Länder begründet. Skandinavische Länder können ihren Energiebedarf beispielsweise mit Hilfe von Wasserkraftwerken decken. Nationen an der Atlantikküste profitieren von den starken Winden und sind theoretisch in der Lage, einen nicht unerheblichen Anteil des Energiebedarfs durch Windkraft zu decken. Wesentlich wichtiger sind allerdings Länder mit einer gleichbleibend starken Sonneneinstrahlung, aber niedriger industrieller Entwicklung, wie beispielsweise viele afrikanische Nationen. In dritte Welt- oder Schwellenländern würde eine zuverlässige Energieversorgung ebenso der humanitären Lage helfen, als das die Grundlagen für Kühlschränke, Wasseraufbereitung und die allgemeinen Hygienestandards gegeben wären. Doch nicht nur industriell gering entwickelte oder Schwellenländer würden von der Energiegewinnung durch Sonneneinstrahlung profitieren, auch hoch entwickelte Nationen wie beispielsweise Singapur könnten davon profitieren. Die aktuelle Energieversorgung Singapurs beruht zum Großteil auf der Verbrennung fossiler Brennstoffe, welche zu 100 % importiert werden müssen. Nicht nur die immense Luftverschmutzung könnte reduziert werden, auch könnte ein Großteil des Haushaltbudgets eingespart werden. Selbst in hoch entwickelten Nationen spielt ein besseres Verständnis von funktionellen Materalien

wie Solarzellen eine wichtige Rolle. So sind Smartphones aus dem heutigen Alltag nicht mehr weg zu denken. Jedoch ist die Haltbarkeit von Akkumulatoren sowie deren Flexibilität ein wichtiger Faktor im Design neuartiger Produkte. Dabei spielt das Verständnis der grundlegenden Prozesse auf einem mikroskopischen und molekularen Niveau eine ebenso große Rolle wie auf einer makroskopischen Skala.

Der Fokus dieser Arbeit liegt in der theoretischen Beschreibung ultraschneller Prozesse in halbleitenden, funktionellen Materialien mittels elektronenstrukturtheoretischer und quantendynamischer Methoden. Um diese Prozesse und zugehörige Materialien zu studieren, wurden hoch parametrisierte Modellhamiltonians verwendet, welche mit Hilfe von hoch akkuraten Elektronenstrukturmethoden parametrisiert wurden. In den meisten Fällen wurde eine Methodenevaluation durchgeführt, welche aus einer Kombination aus verschiedenen Dichtefunktionalen und der wellenfunktionsbasierten Methode der algebraischen diagrammatischen Konstruktion zweiter Ordnung (ADC(2)) basiert. Die Herangehensweise zur Methodenevaluation wurde schon erfolgreich in diversen Theoriearbeiten angewandt. Die zeitabhänginge Schrödingergleichung, welche die dynamische Evolution eines quantendynamischen Systems beschreibt, wurde anschließend mit der multikonfigurationellen zeitabhängigen Hartree Methode (MCTDH) gelöst. Die MCTDH Methode wurde schon erfolgreich im Zusammenhang mit dem Studium ultraschneller Prozesse und verschiedenen funktionellen Materialien angewandt und eignet sich vor allem zur Beschreibung der kohärenten Kurzzeitdynamik, wie sie oft in funktionellen Materialien auftritt. Prozesse auf längeren Zeitskalen, wie beispielsweise im Nanosekunden oder gar Millisekunden Regime, können aufgrund des Ressourcenbedarfs quantendynamischer Methoden nicht untersucht werden. Um trotzdem Informationen über die Langzeitdynamik und somit die mesoskopischen Eigenschaften funktioneller Materialien zu erhalten, wurde die kinetische Monte Carlo Theorie verwendet. Dazu wurde ein Fortran90 Programm geschrieben, welches explizit elektronenstrukturtheoretische Informationen wie den Effekt der Anregungsdelokalisation beinhaltet. Die Behandlung von Delokalisation ist nicht üblich in kommerziell erhältlichen Programmpaketen, stellt jedoch einen wichtigen Teil in der Beschreibung funktioneller Materialien dar.

Das erste Projekt dieser Arbeit bezieht sich auf eine Kollaboration mit der Gruppe von Prof. Dr. S. Haacke der Universität Straßburg. Hier wurde eine neuartige Kombination von Donor-Akzeptor System basierend auf einem Polyhexylthiophen als Elektronendonor

und einem Perylendiimid als Elektronenakzeptor synthetisiert und mittels zeitaufgelöster Pump-probe Experimente untersucht. Durch die kovalente Verbindung eines Elektronendonors und Elektronenakzeptors spielt dieses System eine wichtige Rolle im Design neuartiger Materialien für organische Halbleiter. Experimentell wurden hierbei zwei unterschiedliche Spezies untersucht. Zum einen wurde das System isoliert in einem Lösungsmittel, zum anderen an einer selbstorganisierten, flüssigkristallinen Phase untersucht. Die experimentellen Ergebnisse zu diesen beiden Fällen zeigten unterschiedliche Dynamiken. Während es im isolierten System in Lösung nach der Absorption eines Photons durch den Donor zunächst zu einem resonanten Energietransfer auf den Akzeptor kam, war dieser Prozess in der flüssigkristallinen Phase nicht detektierbar. Hier kam es direkt zur Erzeugung von Ladungsträgern, was im isolierten System erst nach dem resonanten Energietransfer geschah. Die beteiligten Prozesse gingen mit stark unterschiedlichen Zeitskalen einher, was nun durch elektronenstrukturtheoretische und quantendynamische Methoden interpretiert werden sollte. Aus den elektronenstrukturtheoretischen Rechnungen am isolierten Donor-Akzeptor System geht hervor, dass es nach der Photoanregung auf dem Donor zu einer Planarisierung im Thiophenrückgrat, was schon in anderen wissenschaftlichen Arbeiten ähnlicher Systeme als wichtiger Bestandteil der Dynamik identifiziert werden konnte. Ebenso konnten vermiedene Kreuzungen zwischen den beteiligten Zuständen identiziert werden, welche Teil der Ringatmungsmoden des Donors sind. Ein einfaches Modell zur Beschreibung der Dynamik des isolierten Systems in Lösung brachte vibrationell aufgelöste Kohärenzbeiträge hervor, welche mit der Frequenz einer Ringatmungsmode übereinstimmen. Elektronenstrukturrechnungen am System in einer flüssigkristallinen Phase zeigten einen starken Unterschied in der Energetik, im Vergleich zum isolierten System in Lösung. So ist nun der energetisch stabilste Zustand der ladungsseparierte Zustand, welcher ausgehend von der Anregung auf dem Donor schnell populiert werden kann. Das Modell zur Dynamik der flüssigkristallinen Phase beinhaltete zwölf Donor-Akzeptor Dimere mit insgesamt 156 elektronischen Zuständen und 47 Kernfreiheitsgraden. Die durchgeführte Dynamik reproduziert die experimentellen Ergebnisse, zudem sah man, dass hauptsächlich eine Konfiguration populiert wird, bei welcher die Ladungsträger räumlich nahe beieinander sind.

Das nächste Projekt dieser Arbeit betrifft regioreguläres Poly-3-Hexylthiophen (rr-P3HT), welches sehr oft in modifizierter Form als Elektronendonor in organischen Solarzellen verwendet wird. Aktuelle experimentelle Untersuchungen haben gezeigt, dass die

typische Annahme eines Frenkel-Bildes, räumlich gebundener Elektronen-Loch Paare, nicht universell zutreffend ist. In diesen experimentellen Untersuchungen wurden lang anhaltende Oszillationen beobachtet, welche Polaronpaaren zugewiesen wurden. Um dieses System zu untersuchen, wurde ein Modellhamiltonian auf Basis von elektronenstrukturtheoretischen Rechnungen sowie der spektralen Dichte des Systems parametrisiert. Die Verwendung der spektralen Dichte im Rahmen des harmonischen Oszillatormodells erlaubt es, das System ohne eine Vorauswahl an aktiven Koordinaten und somit einer eventuellen Beeinflussung der Dynamik zu untersuchen. Der Nachteil der verwendeten Darstellung ist allerdings das Ignorieren von Anharmonizitäten, hervorgerufen durch gekoppelte Oszillatoren sowie der gesteigerte Ressourcenbedarf durch eine wesentlich höhere Dimensionalität. Das Vernachlässigen von Anharmonizitäten spielt auf sehr kurzen Zeitskalen allerdings keine Rolle, sodass der verwendete Ansatz gerechtfertigt ist. Das komplette Modellsystem beinhaltet somit drei rr-P3HT Monomere mit insgesamt 120 harmonischen Oszillatoren sowie sieben elektronischen Zuständen, welche untereinander diabatisch-elektronisch gekoppelt sind. Eine anschließende Auswertung der mit der Multilayer-Variante von MCTDH (ML-MCTDH) durchgeführten Dynamik zeigte periodische Oszillationen sowohl in der Populationsdynamik als auch in der Dynamik der vibronischen Kohärenzen. Eine Analyse mittels Fouriertransformation zeigt, dass der Einfluss der beobachtetetn Oszillationen stark von der betrachteten vibronischen Kohärenz abhängt. Es konnte gezeigt werden, dass sowohl die Normalmoden in der harmonischen Darstellung als auch die elektronischen Kopplungen einen starken Einfluss auf die beobachteten periodischen Oszillationen haben. Zudem konnte gezeigt werden, dass ein nicht unerheblicher Anteil der Population in ladungsseparierte Zustände transferiert wird.

Das dritte Projekt basiert auf Erkenntnissen, welche aus der vorherigen Studie zur photoinduzierten Dynamik in rr-P3HT gewonnen wurden. Dazu wurde das experimentell und theoretisch bisher bereits gut untersuchte System bestehend aus rr-P3HT als Elektronendonor und dem Fullerenderivat [6,6]-phenyl-C_{61} Butansäure Methyl Ester (PCBM) als Elektronenakzeptor um intermolekulare ladungsseparierte Zustände in der Donordomäne erweitert. Bisher ging man davon aus, dass nach der Absorption eines Photons, ein gebundenes Elektron-Loch Paar an der Grenzfläche zwischen Donor und Akzeptor in freie Ladungsträger dissoziiert. Man ging bisher nicht davon aus, dass intermolekulare, ladungsseparierte Zustände eine wichtige Rolle in der Erzeugung von freien Ladungsträgern spielen. Aus dem vorherigen Projekt ist jedoch ersichtlich, dass solche Zustände sehr wohl möglich sind. Infol-

gedessen wurde ein typischer Modellhamiltonian um diese Zustandskonfigurationen erweitert und das Wellenpaket mittels MCTDH propagiert. Um die große Anzahl an Normalmoden zu reduzieren, jedoch die physikalischen Eigenschaften des Systems beizubehalten, wurde eine Transformation der Normalmodendarstellung in die Effektivmodendarstellung durchgeführt. Diabatische Elektronenstrukturrechnungen zur elektronischen Kopplung der verschiedenen Zustände zeigten deutlich, dass zwischen der Konfiguration der gebundenen Elektron-Loch Paare und den nicht gebundenen Elektron-Loch Paaren in der Donordomäne eine starke Kopplung existiert. Der schlussendliche Modellhamiltonian beschreibt ein Modellsystem bestehend aus 12 rr-P3HT als Elektronendonor sowie einem PCBM Molekül als Elektronenakzeptor, zusammen mit 112 Freiheitsgraden und bis zu 182 elektronischen Zuständen. Die Analyse der elektronischen Populationen zeigte eindeutlich, dass zwar die Effektivität zur Generierung freier Ladungsträger nicht stark beeinflusst wurde, das Zustandekommen dieser Populationen jedoch über einen anderen Mechanismus stattfindet als bisher angenommen. So zeigten Simulationen des gleichen Systems ohne homomolekulare Donor-ladungsseparierte Zustände, dass die Population von ladungsseparierten Zuständen an der Donor/Akzeptor Schnittstelle wesentlich höher ist als mit homomolekularen Donorladungsseparierten Zuständen. Diese Ergebnisse zeigen vor allem, dass zwar das allgemein anerkannte und oft angewendete Frenkel-Modell zur Wellenfunktionsbeschreibung die korrekte Dynamik in gemischten Donor-Akzeptor Solarzellen darstellt, der Mechanismus wie es zur Erzeugung von freien Ladungsträgern kommt jedoch noch nicht eindeutig geklärt ist.

Der letzte Teil dieser Arbeit beschäftigt sich mit der Dynamik auf den langen Zeitskalen und der mesoskopischen Beschreibung dieser Dynamik. Um diese statistischen Simulationen durchzuführen wurde ein Fortran90 Programm zur Lösung der Mastergleichung unter Verwendung des *First Reaction Method* (FRM) Algorithmus geschrieben. Weiterhin wurde explizit der Effekt der Exzitonendelokalisation über mehrere Fragmente betrachtet, was standardmäßig nicht in kommerziell erhältlichen kinetischen Monte Carlo Programmen enthalten ist. Um eine geeignete Morphologie für die anschließende statistische Behandlung im Rahmen des FRM Algorithmus zu erhalten, wurden verschiedene binäre Elektronendonor-Elektronenakzeptor Mischungen erstellt. Zum einen wurden wohldefinierte Morphologien erstellt, welche eine klar definierte Schnittstelle zwischen Donor und Akzeptor vorweisen können, zum anderen wurden zufällig generierte Morphologien mittels Energieminimierung des Ising Hamiltonians erhalten. Dies resultierte in zwei unterschiedlichen Strukturen, welche entweder über eine maximal phasenseparierte oder pha-

senaggregierte Morphologie verfügten. Die Simulationen der idealisierten Donor-Akzeptor Morphologien zeigten, dass es unter bestimmten Umständen möglich ist, ein idealisiertes Elektronengas zu erzeugen, welches sich durch sehr geringe Beeinflussung durch die Coulombkräfte der anderen Ladungsträger auszeichnet. So waren in diesen Simulationen die Ladungsträgermobilitäten als Funktion der Teilchendichte untersucht worden. Die Ergebnisse zeigten, dass die Ladungsträgermobilitäten sowohl für das idealisierte als auch reale Elektronengas nahezu identisch sind. Für die Simulation der zufällig generierten Morphologien wurden sowohl Einteilchensimulationen als auch Mehrteilchensimulationen durchgeführt. Im Rahmen der Einteilchensimulationen wurde untersucht, wie sich die energetischen Fluktuationen des Materials und die Temperatur auf die Exzitonendissoziationseffizienz sowie Ladungsträgermobilitäten auswirken. Während der Einfluss der energetischen Unebenheit und der Temperatur auf die phasenaggregierte Morphologie stark war, so war dies nicht der Fall für die maximal phasenseparierte Morphologie. Eine Besonderheit der Ladungsträgermobilitäten konnte für die phasenaggregierte Morphologie entdeckt werden, bei welcher für niedrige Temperaturen eine Frenkel-Poole-artige Abhängigkeit von der Feldstärke beobachtet werden konnte. Die Mehrteilchensimulationen zeigten im phasenaggregierte Fall, dass die Ladungsträgermobilität als Funktion der Teilchenanzahl stetig abnimmt. Für die phasenseparierte Morphologie konnte hingegen beobachtet werden, dass die Elektronenmobilität sowohl für das reale als auch ideale Elektronengas nahezu identisch ist, was auf die strukturellen Besonderheiten der gegebenen Morphologie zurückzuführen ist.

Zusätzlich zu Simulationen an idealisierten als auch zufällig generierten Nanomorphologien wurden Ergebnisse aus einer Röntgenstrukturanalyse als auch Molekularmechanik verwendet, um die zweite Generation einer kovalent gebundenen Donor-Akzeptor Dyade mittels statistischen Simulationen zu untersuchen. Um möglichst akkurate Parameter für die anschließenden Simulationen zu erhalten, wurden Transferintegrale aufgrund von elektronischen Strukturrechnungen bestimmt. Dabei stellte sich heraus, dass die Transferintegrale für den Elektronentransfer entlang der π-Stapelung der Akzeptormoleküle um den Faktor 50 beziehungsweise 10^6 größer sind als entlang der nächst möglichen Transferpfade. Aus dieser Betrachung lässt sich schlussfolgern, dass die dreidimensionale Simulationsbox zu einem nahezu eindimensionalen Elektronentransferpfad reduziert wird. In den anschließenden Simulationen zeigte sich, dass die Ladungsträgermobilität als Funktion der Teilchendichte stetig zu nimmt. Dies lässt sich dadurch erklären, dass das Teilchen, welches am nähesten zur Detektorelektrode ist, einen starken Schubeffekt der dahinter liegenden

Teilchen spürt und somit in Richtung Detektorelektrode geschoben wird. In Kombination mit dem hohen Transferintegral entlang der π-Stapelung ergibt sich somit ein nahezu eindimensionaler Transferpfad durch das Nanomaterial.

Die im Rahmen dieser Arbeit erhaltenen Ergebnisse zeigen, dass die Dynamik photogenerierter Exzitonen sowie der Prozess der Exzitonendissoziation ultraschnell sowie von quanten-kohärenter Natur sind. Weiterhin konnte gezeigt werden, dass im Rahmen einer stochastischen Behandlung die mesoskopische Anordnung von Donor- und Akzeptorpaaren eine entscheidende Rolle in der Dynamik der Ladungsträger spielt. Die Ergebnisse können daher als Grundlage für eine weitergehende Behandlung ultraschneller Prozesse in funktionellen Materialien im Hinblick auf eine multiskalen Modellierung dienen.

2 — Introduction

What Took You So Long?

Kazuhira Miller

In recent years, the cost of fossil fuels has experienced a major increase. For example, the price of imported raw oil rose from 65 Euro/tSKE in 1995 to 441 Euro/tSKE in 2012 [1]. Unfortunately, not only the cost of fossil fuels has risen, the greenhouse effect became a major problem [2]. Therefore, in order to reduce the effects of global warming caused by the greenhouse effect, alternative and regenerative energy sources have become a topic of major interest [3, 4]. Due to geological and meteorological constraints, the availability of the different regenerative energy sources depends on the country it is supposed to be used. Norway for example has huge ressources to cover its energy needs by hydrodynamic power. In fact, Norway is the only industrialised country that is able to cover its total energy expenses by hydrodynamic power [5, 6]. On the other hand, solar energy has a lot of potential, especially in countries with a high rate of solar radiation. In the beginning of the developement of solar cells based on silicon, the energy-to-power conversion efficiency was rather poor. Since then, a lot of progress has been made and typical solar cells based on inorganic compounds can reach peak efficiencies of 45% [7]. The drawback of these solar cells is the production cost due to the demand of high purity of the base material, i.e. silicon [8]. On the other hand, photovoltaic devices made up from organic compounds have emerged as a cheaper alternative in recent years [9–11]. Due to intense research conducted to organic photovoltaic devices, dramatic increases in the power conversion efficiency could be made and organic solar cells are now an affordable alternative to silicon based devices. Furthermore, organic functional materials are also important for electronic devices such as transistors, since such devices can be build on a molecular scale, rather than on a nanoscale, as it is typical for silicon based functional materials [12].

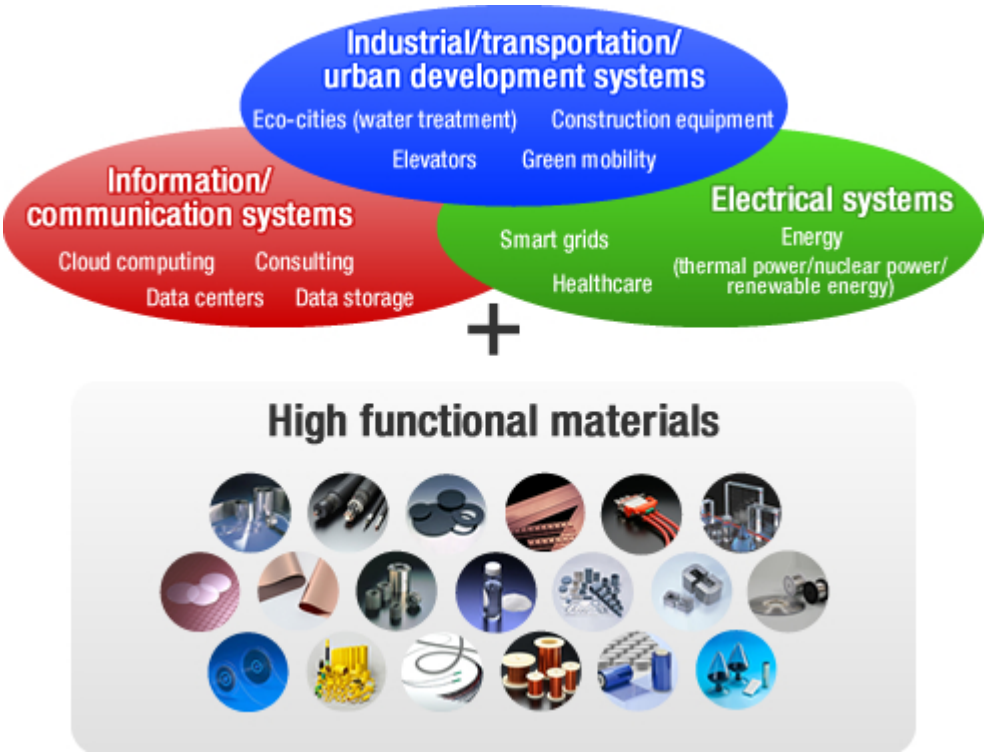

Figure 2.1: Overview over the field of applications for functional materials. Taken from reference [13].

A scientific understanding of the functionality of these materials is of crucial importance in order to build more efficient devices. The research for these kind of materials is going into a variety of directions, ranging from the correlation between morphology and efficiency to the molecular properties of the individual building blocks [14–19]. The aim of this work is to provide an insight into the aforementionend correlation between the structure of the functional materials and the properties resulting from that. To reach that goal, different methods have been employed to study the photophysical properties of typical organic functional materials. While the short time dynamics shortly after photoirradiation are dominated by quantum effects and coherent processes, suitable model Hamiltonians have been parametrised by high level electronic structure calculations. The dynamical treatment has been done with the aid of the Multiconfigurational Time Dependend Hartree (MCTDH) method in the multilayer formalism. Amongst others, a new type of donor-acceptor (DA) co-polymer, experimentally developed and investigated in the group of S. Haacke from Strasbourg University, has been investigated with the before mentioned combination of methods. The novel DA system consists of a bis-thiophene derivative as an

electron donor and a perylene-diimide derivate as an electron acceptor. As a special point of emphasis, the correlation between the liquid crystal (LC) structure and the resulting photophysical properties have been investigated. The second project covered in this thesis is based on recent experimental results on regioregular poly-3-hexyl-thiophene (rr-P3HT), where periodic time resolved signals have been attributed to long lived polaronic species. This particular point of view leads to a new perspective when investigating functional materials, since so far the appearance of polaronic signals in the standard Frenkel-type description of organic semiconductors is not very common. The third project is tied up to the second project, as the results from the investigation of RR-P3HT have been connected to investigations covering a rr-P3HT domain as an electron donating unit and a [6,6]-phenyl-C_{61}-butyric-acid-methyl-ester (PCBM) molecule as an electron accepting unit. The combination of P3HT/PCBM is an extensively studied organic solar cell, both on the theoretical and experimental side [20–23]. In previous theoretical investigations, the appearance of polarons within the P3HT donor domain have been neglected. Therefore, a typical model Hamiltonian describing the photophysical properties of a P3HT/PCBM system has been used and extended to treat also polaronic effects within the P3HT domain. The last project covers the long time dynamics and statistical methods in the framework of a given bulk heterojunction (BHJ) nanomaterial. Specifically for this topic, a kinetic monte carlo algorithm has been implemented into an efficient Fortran90 code, which should enable to do first simulations on functional BHJ nanomaterials. As a result of the quantum mechanical nature of such materials, delocalisation effects have been incorporated explicitly into the program. In order to obtain a suitable and experimentally comparable observable, the charge carrier mobility has been calculated as a function of particle density in the system, both for idealised BHJ morphologies as well as randomly generated morphologies.

The thesis is organised as follows. First, a general introduction to the understanding of organic photovoltaic devices will be given. Along with a phenomenological description of the different processes in such materials, the basic equations to treat these processes will be given and explained. Then, the theoretical background behind the applied methods will be explained and the advantages and disadvantages of the different calculation schemes will be emphasized. The last part of the thesis covers the results obtained for the four studied topics, with the aim of understanding the principle processes following the photogeneration of an exciton and the subsequent processes.

Part I

Theoretical Background

3 — Energy & Charge Transfer in Organic Polymers

The purpose of this chapter is to explain the basic principles of organic photovoltaic devices and their associated properties and characteristics. The first section will provide a general overview over the field of organic photovoltaic devices. Furthermore, the different morphological realisations of these devices will be presented and discussed.

The second section will deal with the generation of bounded electron-hole pairs after photoexcitation, so called excitons, and their dissociation into free charge carriers at a donor-acceptor interface. Along these lines, the physical and mathematical treatment of these processes will be viewed from different perspectives. Depending on which aspects of the system one is interested in, one can either use a detailed molecular approach or a coarse grained approach, which neglects the microscopic details, but allows the treatment of an entire nanoscale domain.

The third and last section is about the theoretical treatment of these dynamical phenomena, either at a quantum level or within a molecular site based representation. Therefore, different theories will be introduced which, by the end of the day, describe the same dynamical phenomena, yet from different perspectives.

3.1 Organic Photovoltaic Devices

Organic photovoltaic devices have become a promising alternative to conventionally used silicon-based solar cells. The main drawback of conventional silicon-based organic photovoltaic devices is their production cost. In order to obtain an efficient photovoltaic cell made of silicon, one needs natural resources of very high purity, with a maximum percent-

age of impurities below 0.01 % [24]. This quality standard is called solar grade silicon. In order to obtain such clean silicon one needs a huge amount of energy. Usual methods for the purification process are the Czochralski process [25] and the Siemens process [26].

The Czochralski process requires as an input resource already silicon of very high purity. The input ressources are then melted inside a quartz crucible at around 1400 degrees Celsius. Afterwards, a seed crystal is dipped into the molten silicon and slowly pulled upwards. By controlling the rotation of the mounted seed crystal around its own axis and the speed at which the crystal is being pulled out of the liquid, it is possible to obtain a large single-crystal made of very pure silicon [27].

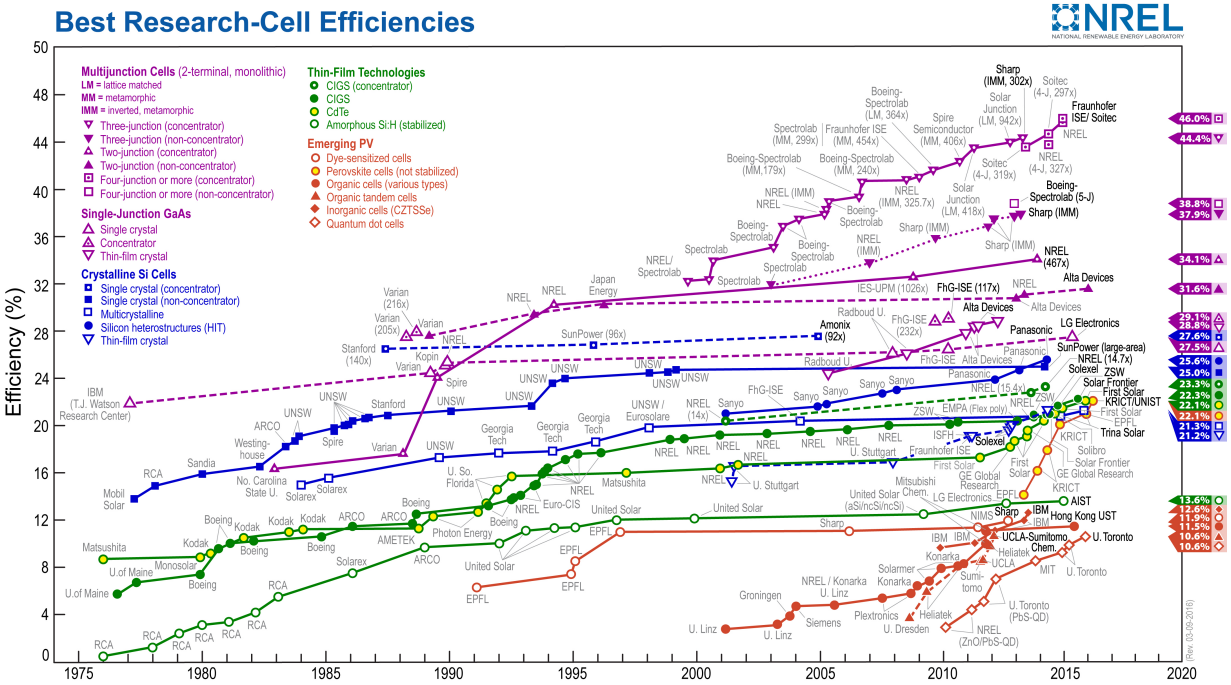

Figure 3.1: Overview over a wide variety of organic & inorganic solar cells and their efficiencies. Taken from reference [7].

Today's best known process for obtaining solar-grade silicium is the Siemens process. Here, metallic silicon is treated with gaseous hydrochlorid acid, which forms liquid trichlorsilane at a temperature of 600 K. Afterwards, a chemical vapor deposition technique is applied by which the liquid trichlorsilane is vaporised at 1400 K and blown over pre-existing silicon seeds. This procedure can be repeated over and over again, until the desired purity

of the silicon is achieved.

One can imagine that the energy consumption of these methods to produce solar grade silicon is very high. A promising and cheaper alternative for photovoltaic devices are solar cells based on organic compounds. At the beginning of the development of solar cells based on organic compounds, these materials had an efficiency of below 5%. Due to intense research an immense progress was made during the last decades and todays organic-based solar cells reach efficiencies of up to 20%. In comparison to that, most silicon based solar cells reach efficiences of about 25%.

Figure 3.1 shows a comparison of the efficiencies of different solar cells made of different materials. Comparing the orange and blue traces, one can see that the advances of crystalline silicon became smaller and smaller. One reason for the increase in efficiency of the organic solar cells are new morphological realisations of these cells. In contrast to silicon-based solar cells, which consist only of silicon as a material, typical organic solar cells consist of at least two different compounds, one of which is an electron donating material and one which is an electron accepting material. Hence, there also exist different realisations of the morphological appearance of organic solar cells [28].

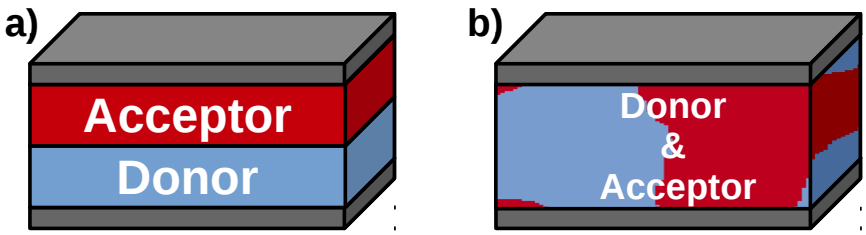

Figure 3.2: Schematic illustrations of two different morphologies of donor/acceptor solar cells. a) Bilayer morphology with a clear phase separation and b) Bulk-Heterojunction (BHJ) morphology with intermixing donor/acceptor phases and larger interfacial area.

Figure 3.2 shows a sketch of two representative morphological realisations of organic donor-acceptor solar cells. Figure 3.2a shows the simplest approach when combining an electron donating material (blue) and an electron accepting material (red), resulting in a bilayer solar cell. Figure 3.2b shows a sketch of a so-called Bulk Hetero-Junction (BHJ) solar cell. Here, the donor (blue) and acceptor (red) materials are strongly mixed, which leads to an increase of the donor-acceptor interface. This results in an increased efficiency

for BHJ solar cells compared to the bilayer approach. In both figures, the grey area represents the cathode and anode, respectively.

The first organic solar cells exhibiting a bilayer morphology were produced by Tang et al. in 1986, which used copper phthalocyanines and a perylene tetracarboxylic derivative combined to a bilayer solar cell [29]. During the next few years, the efficiency of these materials increased steadily by finding new combinations of organic compounds for the fabrication of bilayer solar cells. In 1992 it was shown that the electron transfer from conjugated polymers to fullerenes is very effective [30]. However, the bilayer morphology of the constructed solar cells was limiting the power conversion efficiency due to poor exciton dissociation efficiencies and various other reasons. The most important reason was that the free diffusion length of the excitons (of the order of 10 nm) was smaller than the width of the domain size of the electron donating material. This leads to the effect that only excitons which were generated near the donor/acceptor interface were able to dissociate into free carriers. To overcome these drawbacks, Yu et al. strongly mixed the donor and acceptor areas in order to increase the donor/acceptor interfacial area [31]. This reduced the average distance the excitons have to travel until they reach the interface and the exciton dissociation effiency was enhanced drastically. Much research is conducted to the exploration of different processing techniques in order to enhance the interfacial area and mixing of the donor and acceptor phases to further enhance exciton dissociation efficiencies.

After a brief overview over the different morphological realisations of donor-acceptor BHJ nanomaterials, the key steps in the generation of free charge carriers from exciton diffusion and dissociation will be explained in the following.

Figure 3.3a shows a schematic representation of the charge carrier generation in a typical BHJ morphology. Here, red is the electron donating material and blue is the electron accepting material. The different processes leading to the generation of free charge carriers can be broken down into four steps:

1. After irradiation by light, a localised (or partially delocalised) electron-hole pair – i.e., an exciton – is created in the donor material.

2. Through random exciton diffusion the exciton pair eventually reaches the donor/acceptor interface.

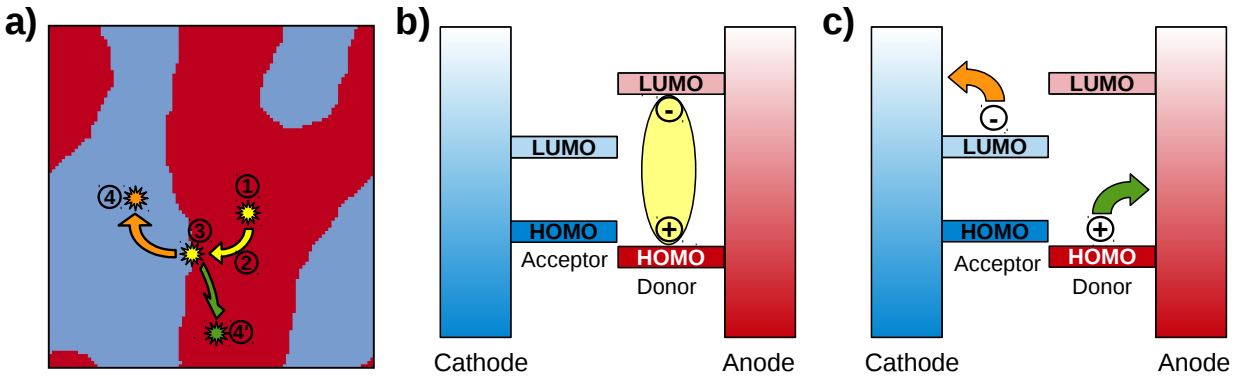

Figure 3.3: Working principle of a BHJ solar cell. a) Cartoon of a BHJ solar cell with a percolation network connecting the donor phase (red) to the anode and the acceptor phase (blue) to the cathode (both not shown here). b) Bound electron-hole pair (exciton) after photoexcitation of the donor phase. c) Generation of free charge carriers upon exciton dissociation and transfer to the respective electrodes.

3. At the interface, the exciton can dissociate into electron (orange) and hole (green).

4. Both types of carriers remain in their respective domains, i.e. the electron will be transported in the acceptor material (blue) whereas the hole will be transported in the donor material (red).

Due to different work functions of the respective electrodes (i.e. cathode and anode) or the application of an external electric field, the electrons will diffuse towards the cathode whereas the holes will diffuse to the anode.

Figures 3.3b and c show a more detailed description in terms of molecular energy levels of the processes after photoirradiation. As it has been pointed out above, a bound electron/hole pair is created in the donor material after photoexcitation. Within an energy level type description, one can say that the hole is located on the donor's highest occupied molecular orbital (HOMO), while the electron is associated with the donor's lowest unoccupied molecular orbital (LUMO). If the exciton reaches the donor/acceptor interface ((3) in figure 3.3 a)), the bound electron-hole pair will dissociate into free charge carriers. Therefore, the electron will be transferred from the donors LUMO to the acceptors LUMO, while the hole remains in the donors HOMO. The charges will then hop between the different HOMO/LUMO levels of different donor/acceptor molecules until they reach the respective electrode. As shown in figure 3.3c, the respective charge carriers will be

collected at the electrodes, upon which a current can be measured.

Within this chain of processes, there are also several loss mechanisms associated with the exciton and the free charge carriers, which will reduce the power conversion efficiency. Notably, losses occur due to the following effects:

- Delayed dissociation of the exciton, i.e., a significant portion of the excitons may not reach the interface and will eventually recombine. This factor can be controlled by tuning chemical design, and by optimizing the donor domain size, i.e. creating highly dispersed donor/acceptor mixtures and hence, increasing the donor/acceptor interfacial area as in BHJ architectures.

- Depending on the material, exciton migration across the donor/acceptor interface may occur. That is, after the exciton has reached the interface, it will not dissociate into electrons and holes, but the bound electron-hole pair will be transfered from the donor to the acceptor. Since there is no driving force anymore to separate electrons and holes due to the energetically lower lying nature of the HOMO and LUMO on the acceptor (see also figure 3.3b & c), the exciton will eventually decay without being dissociated.

- A third loss mechanism relates to recombination at the interface. After the exciton has dissociated at the interface, the electron and hole remain coulombically bound to each other. This opens the pathway to geminate recombination, where electron and hole will recombine into the ground state.

Even though much research has been done in order to reduce the loss mechanisms associated with BHJ morphologies, there is still a lot of work to do, as can be seen by the huge gap in power conversion efficiencies between standard organic solar cells (orange in figure 3.1) and multijunction cells (purple in figure 3.1).

As it has been pointed out earlier, the morphology of the donor and acceptor phases is crucial for an efficient device performance. Various types of nanomorphologies have recently been explored, including highly ordered (regioregular) domains and covalently bound block-co-oligomer architectures [32–34]. With regard to the latter direction, our collaboration partners at the University of Strasbourg have designed perylenediimide-based donor-acceptor co-oligomers which form highly ordered lamellar mesophases, enhancing exciton dissociation and charge transport to the electrodes [35, 36].

3.2 The Generation of Excitons and Charges

The previous section was dealing with the overall device characteristics of organic photovoltaic cells and the impact of the morphology on the device performance. In this section I will focus on a more in-depth characterisation of the fundamental processes in the material and the definition of excitons and charge transfer states.

When a molecular crystal is irradiated with light, it absorbs a photon which is in resonance with the energy gap between the HOMO and LUMO. Therefore, an electron is promoted from the HOMO level to the LUMO level, leaving an unpaired electron and a hole behind in the HOMO while the other electron is now located in the LUMO. This state is called an excited state in a molecular context, or in the framework of semiconductors, an exciton. An exciton is an electrically neutral quasiparticle in which the excited electron and the resulting hole are bound to each other via Coulomb attraction.

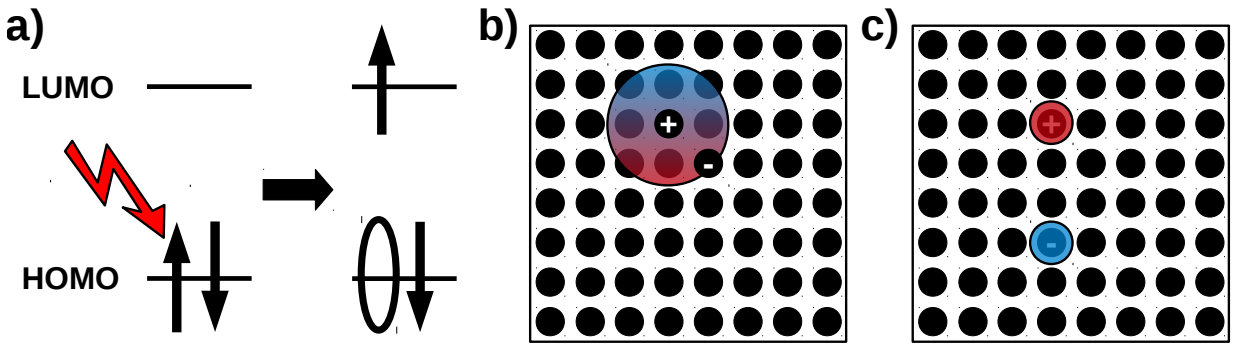

Figure 3.4: a) Molecular energy levels before (left) and after (right) photoexcitation, creating a bound electron-hole pair. b) Schematic illustration of an exciton on a molecular lattice. Electron and hole remain bounded by Coulomb forces. c) Charge transfer state, where electron and hole are not bound anymore and act as independent particles.

Figure 3.4 shows a sketch of the process after photoexcitation (a) as well as a cartoon of an exciton and a charge transfer state (b & c). Figure 3.4 a) shows a sketch of the creation of an exciton. Irradiation of a neutral molecule or molecular crystal with light results in the creation of an exciton. Excitons, as an electron hole pair, can move through a molecular system and hence, transport energy. From the sketch in figure 3.4b it is evident that an exciton can have different sizes. These sizes are determined, amongst other factors, by the dielectric constant of the medium. As for photovoltaic devices made of organic molecules,

the dielectric constant is small and thus, the size of the exciton is rather small and confined, usually limited to several molecular units within the donor or acceptor domain. In such a case, one speaks of *Frenkel excitons* [37]. Figure 3.4b shows a case in which the exciton is spread over a small number of monomers. Within the Frenkel picture, delocalization is accounted for by coherent superpositions of site-local electron-hole pairs.

If the exciton reaches a donor-acceptor interface, it is able to dissociate into free charge carriers. In between those two cases, i.e. a localised and bound electron-hole pair and free electron and hole, an intermediate state is formed. This intermediate state is usually called interfacial charge transfer state (or charge transfer state, or else interfacial charge transfer exciton). In a charge transfer state, electron and hole occupy adjacent donor vs. acceptor molecules. This is shown in figure 3.4c. Here, the electron and the hole remain strongly coupled, due to their spatial proximity. A Coulomb barrier has to be surmounted to separate the interfacial charge transfer state into free carriers.

As discussed in the recent literature [38], charge transfer states not only occur at the donor/acceptor interface, but can also be generated in a pure donor domain. If this pre-dissociation happens close to the donor/acceptor interface, it may increase the exciton dissociation efficiency and hence, increase the overall power conversion efficiency. This effect may also reduce the loss processes such as exciton recombination and charge recombination.

The transfer of excitons within a given material can be described at different levels of description:

- full quantum dynamical level, using the MCTDH method mentioned above. Our recent study in reference [39] is an example of this – computationally very expensive – approach;
- hopping type transfer, relying on Förster theory applied to neighboring sites [40, 41];
- diffusive transport, relying on diffusion equations for longer length scales [42].

In the following, we briefly comment upon the second and third approaches, which are used in standard treatments.

The Förster resonance energy transfer (FRET) type description of excitation transfer is based on a molecular description involving Coulomb couplings and the spectral overlap between two molecular aggregates [40, 43]. This approach is suitable if one is interested in the behaviour on small length scales, but coherent effects intrinsic to the quantum regime are neglected. If one is interested in the simulation and modeling of complete photovoltaic devices, it is more suitable to think in terms of a diffusion type process, where one can use classical equations. Figure 3.5 shows a sketch of the molecular based FRET process and a macroscopic diffusion type process.

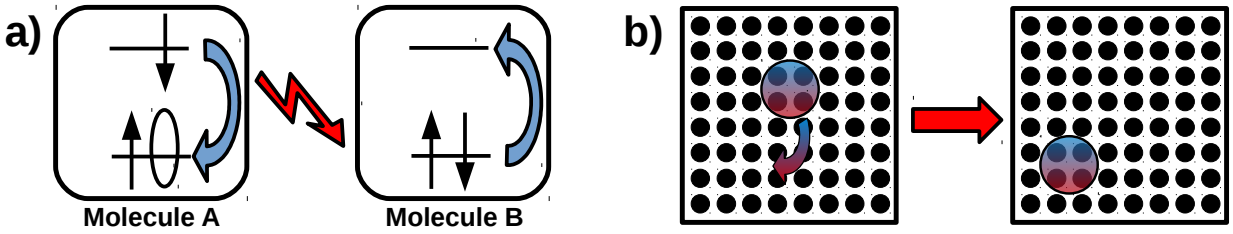

Figure 3.5: Cartoons of different exciton transport mechanisms. a) A FRET processes between molecule A & molecule B. b) Diffusion type process, where the exciton diffuses through a molecular lattice.

The FRET process shown in figure 3.5a is based on a molecular description. Here, molecule A is in the excited state whereas molecule B is in the ground state. If the exciton located on molecule A recombines into the ground state, it emits a virtual photon of wavelength λ. If the wavelength of this virtual photon is in resonance with the energy gap between the HOMO and LUMO level of the acceptor, an excitation on that molecule will occur. Hence, the excitation energy has been transferred from the donor molecule A to the acceptor molecule B.

In contrast to this molecular orbital type description, figure 3.5b shows a diffusion type process of excitation energy transfer within a given macromolecular assembly. Here, the excitation can be localised or delocalised over various fragments and the diffusion of the excitation obeys ordinary diffusion equations known from classical mechanics.

The computational modeling of exciton diffusion in nanoscale BHJ materials is of crucial importance to simulate the overall device performance. Since excitons are the precursors of free charge carriers, exciton diffusion and its associated time and length scales have to be modeled appropriately. In recent literature it has been shown that a FRET type description and a diffusion type description of exciton migration within a given material yields

the same results in terms of exciton dissociation efficiency and exciton diffusion length [44]. However, it has also been shown that the distribution of the exciton lifetimes for a given BHJ material is not constant, but it follows an exponential distribution. Simulations taking this behaviour into account are able to explain the too high exciton dissociation efficiency usually obtained in statistical simulations such as KMC [41].

After the exciton has reached the donor/acceptor interface, it can dissociate into free charge carriers. As mentioned above, before the free charge carriers are formed, an intermediate state is created, which is usually called a charge transfer state. Here, electron and hole are located on different fragments, but they still remain close to each other. From figure 3.3b & c one can see that the energy level of the electron accepting material is lower than the energy level of the electron donating material. Hence, it is energetically favourable that the electron is transferred from the donor to the acceptor. Recently it could be shown that the higher the energy of the initially created charge transfer state (also called "hot" charge transfer state), the higher the exciton dissociation efficiency [45, 46]. Not only is the exciton dissociation efficiency influenced by the energetics of the charge transfer state, but also the overall process of charge separation. Charge separation takes place if the electron and hole can be treated as separate particles. Usually one refers to charge separated states as soon as the charges overcome the Coulomb barrier or reach a material dependent spatial separation. The process of charge separation does not only depend on the gain in energy upon exciton dissociation, but also depends on the external and internal electric fields, molecular arrangements and the associated transfer efficiencies [47–49]. If the step between the creation of a charge transfer state and subsequent charge separation is not efficient enough, recombination between the two attracting charges will take place, which will ultimately lead to a loss process. If charge separation has occurred, the transfer of the charges depends on multiple material dependent properties and again, different theories can be applied to describe these process.

Figure 3.6a shows a sketch of the correlation between the structural order of the BHJ nanomaterial and the associated charge carrier mobility and the theory best suited to describe the charge migration. For low structural order (and hence, a large energetic disorder), one is within the hopping regime of charge migration [50]. Here one can apply classical theories such as Marcus theory or semi-classical theories such as Marcus-Levich-Jortner theory. As the name implies, in this regime the charges are localised on specific

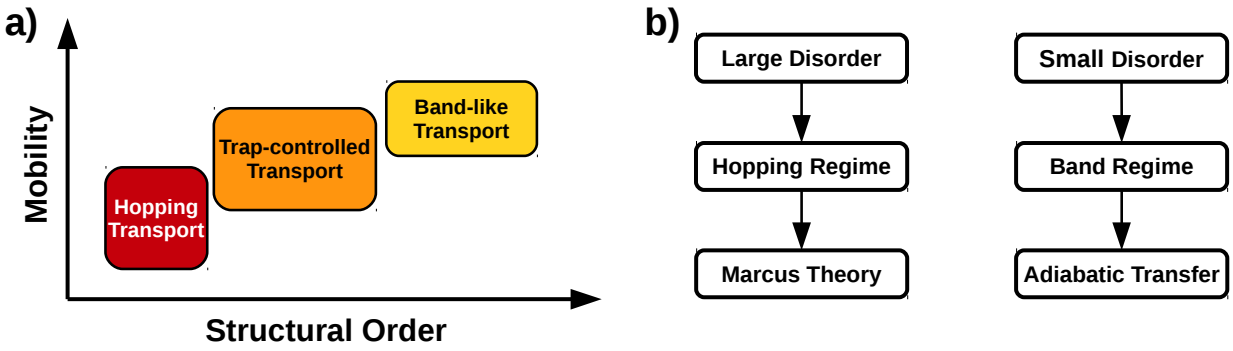

Figure 3.6: a) Correlation between the structural order of a BHJ nanomaterial and the associated charge carrier mobility. b) Theories describing the structural disorder of a given system.

molecular sites due to the low structural order and charges are hopping between the different sites. For high structural order (and hence, a low energetic disorder), the wave function of the charge carrier is delocalised over various fragments and hence, one has a coherent or band-like transfer [51]. The charge can move mostly without any obstacles and charge carrier mobilities are very high. This is the regime pertaining to inorganic semiconductors. Figure 3.6b shows a summary of the two limiting regimes describing either a hopping transport or a band-like transport.

Although it may sound as if only the band-like regime allows for large charge carrier mobilities, this is not the case. In real organic photovoltaic devices, and most noticeably BHJ nanomaterials, there are domains with high and low structural disorder caused by the huge flexibility of the large molecules. This leads to the result of domains in the material where one has to use either theories explaining the transfer within the hopping regime on long time scales or theories that explain the transfer within the band regime – involving quantum coherent transport – on short time scales. Hence, in order to fully understand the mechanisms in organic photovoltaic devices, one has to employ multiscale modeling techniques that cover both extreme ends of the time scales [52–54].

3.3 Theoretical Description of Exciton & Charge Transport

As pointed out in the previous section, in order to gain an overall understanding of the fundamental processes taking place in organic BHJ nanometerials, it is inevitable to con-

sider not only the dynamics on short time scales, but also the behaviour on longer time scales. The problem is that there are many different processes happening on different time scales and even single processes like charge transport contribute to different time scales and length scales. From a molecular point of view, the transport of excitation energy is usually described within a kinetic description in terms of a FRET [40] process, as pointed out in the previous section. The FRET transfer rate is given as

$$k_{FRET} = \frac{1}{\tau}\left(\frac{R_0}{r}\right)^6 \tag{3.1}$$

with

$$R_0^6 \propto \int_0^\infty F_D(\lambda)\epsilon_A(\lambda)\lambda^4 d\lambda \tag{3.2}$$

Equation 3.1 states that the rate for excitation energy transfer depends on the inverse lifetime of the donor state as well as a term depending on a system specific "Förster radius" R_0, which is shown in equation 3.2. The latter term is proportional to the overlap of the fluorescence (or emission) spectrum of the donor ($F_D(\lambda)$) and the absorption spectrum of the acceptor ($\epsilon_A(\lambda)$). Hence, in order to have an efficient excitation energy transfer, the molecules have to be spatially close to each other and their respective energy gaps for donor flourescence and acceptor absorption have to be of the same order of magnitude. Equation 3.1 can readily be employed in large scale methods such as molecular dynamics or KMC simulations. When dealing with small systems and short length scales, quantum effects play a non-negligible role and one has to use more appropriate methods.

Usually one employs Hamiltonian based methods and resorts to a site-based Hamiltonian, [55–57].

$$\hat{H} = \epsilon \sum_n a_n^\dagger a_n + J \sum_n \left(a_n^\dagger a_{n+1} + a_{n+1}^\dagger a_n\right) \tag{3.3}$$

Equation 3.3 is a typical Hamiltonian to treat the exciton transfer on a lattice within a quantum mechanical framework. Here, ϵ is the energy of the exciton in the molecular system, $a_n^\dagger$ (a_n) is the creation (annihilation) operator of an exciton at molecular site n, written in terms of second quantisation. The second term describes the transfer of an exciton from one site to its neighbor, mediated by the coupling J. In a quantum mechanical representation, the exciton transfer is mediated by the coupling of the individual transi-

tion dipole moments. Note that the Hamiltonian shown in equation 3.3 is representend in a purely electronic picture. This representation can be extended with electron-phonon couplings, introducing additional terms, which will result in a more detailed representation of the molecular properties. The introduction of phonon modes and electron-phonon couplings will influence the energetic landscape of the system under study. The reason is that modified resonance effects will appear, along with dynamically trapped molecular sites and energy barriers in the energetic landscape, requiring the description of exciton transfer on different time scales.

The theoretical treatment of electron transfer within a classical framework is usually done by Marcus theory [58]. Here, one assumes that the electron is transferred from a spherical donor to a spherical acceptor molecule, which is mediated by a classical intermolecular coordinate, or polarization coordinate [59–61]. Along with these assumption and some mathematical operations, one obtains for the Marcus transfer rate

$$k_{ij} = \frac{2\pi}{\hbar} J_{ij}^2 \sqrt{\frac{1}{4\pi k_B T}} exp\left(-\frac{(\Delta G_0 + \lambda)^2}{4\lambda k_B T}\right) \tag{3.4}$$

Here, the transfer of a charge from molecule i to j depends on the electronic coupling J_{ij} between the two molecules, the temperature T, the difference in Gibbs free energy ΔG_0 and the reorganisation energy λ. Pictorially, this can be represented as shown in the graphical representation of Figure 3.7.

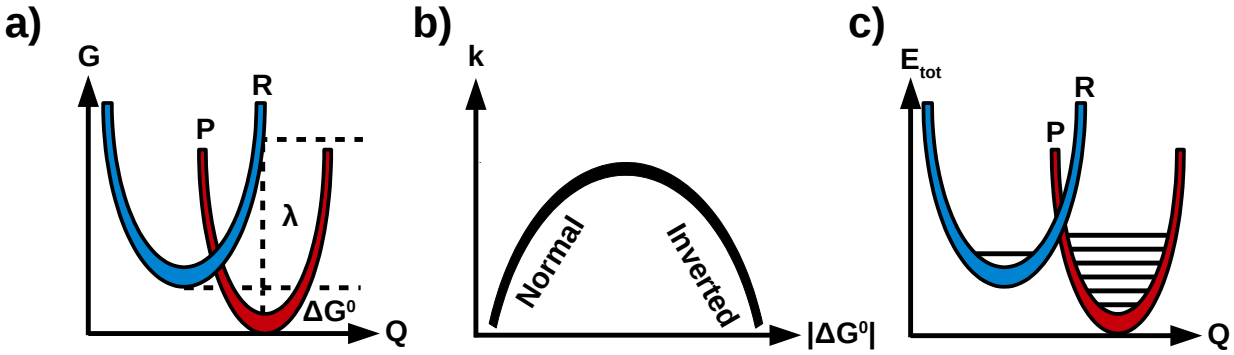

Figure 3.7: a) Classical Marcus-Theory, where a charge is being transported from the reactant to the product. Additionally, the reorganisation energy λ and the Gibbs free energy ΔG_0 are shown. b) Correlation between normal region and inverted region with the associated Gibbs free energy. c) Semi-classical Marcus-Levich-Jortner-Theory including the splitting of the final accessible product state into several states.

Figure 3.7a illustrates classical Marcus theory, where a charge is being transferred from a reactant R to a product P. The magnitude of ΔG_0 as compared with λ plays an important role in classical Marcus theory [62]. If the value of ΔG_0 is smaller than λ, then the rate increases as $|\Delta G_0|$ increases. In a Marcus-type transfer, one usually refers to that kind of behaviour as the normal regime, see also figure 3.7b. As soon as $|\Delta G_0|$ is larger then λ, the transfer rate decreases again with increasing $|\Delta G_0|$, which is called inverted regime. The reason for this behaviour is that the intersection between the two parabolas associated with P and R moves upwards with increasing $|\Delta G_0|$ and hence, the activation energy for the reaction becomes higher.

An extension of the classical Marcus theory is the semi-classical Marcus-Levich-Jortner theory [63], pictorially represented in figure 3.7c. Here, one assumes that the charge transfer is coupled to a low-frequency intermolecular classical coordinate as well as to a high-frequency intramolecular coordinate. By imposing that one has a single initial state but several final states, indicated by the vertically spaced energy levels in figure 3.7c, one has several possible pathways to charge transfer, instead of only a single pathway in classical Marcus theory.

As an analogue to the classical (or semi-classical) representation of charge transfer given in the Marcus-Theory and Marcus-Levich-Jortner-Theory, several model Hamiltonians for a quantum description have been developed. In particular, the Su-Schrieffer-Heeger (SSH) [64, 65] Hamiltonian has been succesfully used to describe charge phenomena in molecular crystals.

$$\hat{H} = \frac{M}{2}\sum_i \dot{x}^2 + \frac{k}{2}\sum_i (x_{i+1} - x_i)^2 - \sum_{i,\sigma} t_{i+1,i}\left(c^\dagger_{i+1,\sigma}c_{i,\sigma} + h.c.\right) \tag{3.5}$$

Here, the first term is the kinetic energy of the nuclei, expressed in terms of the time-derivative of the coordinates, also called group displacement in the context of *poly*-acetylene. The second term is the potential energy associated with a bond deformation in an harmonic approximation, with the force constant k. The last term is the electron interaction energy associated with a hopping process. In particular, $t_{i+1,i}$ is the transfer integral between two fragments, $c^\dagger_{i+1,\sigma}$ ($c_{i\sigma}$) is the creation (annihilation) operator of an electron of spin σ at site $i+1$ (i). In the case of strong electron-phonon coupling, the transfer integral can be influencend by bond deformation of the associated transfer channel.

Even though different multiscale modeling approaches have been employed successfully to simulate loss processes in BHJ nanomaterials [66], open questions still remain. A challenge remains the treatment of the eliminated degrees of freedom, which one has to sacrifice by going from a small length scale, and hence from an atomistic point of view, to a large length scale [67]. Nevertheless, there are already successful applications of such methods that model overall device performances using a coarse grained approach to obtain reliable results from simulations [68, 69].

3.4 The Role of Coherent Quantum Dynamical Effects

Until a few years ago, the standard approach for the description of excitation energy transfer (EET) and charge transfer (CT) relied entirely on classical kinetic equations describing a hopping-type transport [63].While this assumption is valid to a certain degree and especially forstatistical modeling like Kinetic Monte Carlo approaches, important deviations froma kinetic description were observed in recent time-resolved experiments,highlighting the influence of coherence effects on the short time dynamics [70–72].

Previously, the generally accepted assumption for π conjugated polymeric systems was that exciton transport lies in an incoherent hopping type regime since the relevant electronic couplings were assumed to be small. Therefore, decoherence effects were taken to be pronounced and a hopping type mechanism was thought to be appropriate to model exciton transport in conjugated materials. However, recent investigations on functional materials show that electronic couplings tend to be strong enough to retain quantum coherent effects in such systems. As a result, a description of EET via a hopping mechanism is not always appropriate. In particular, recent studies include photon echo experiments — more specifically, three-pulse photon echo peak shift (3PEPS) experiments [73, 74] – that have been used to study quantum coherent effects in poly[2-methoxy-5-(2'-ethylhexyloxy)-p-phenylene vinylene] (MEH-PPV) and related materials. In order to interprete the experimental results, theoretical calculations employing the SSH Hamiltonian have been performed. The analysis revealed that first a delocalised excitonic state has been formed, which is subjected to dynamic localisation based on an initial decay of the 3PEPS signal. The dynamic localisation could be explained by decoherence effects that act on a timescale of 100-200 femtoseconds. Following this localisation, the subsequent

transfer of the localised exciton can be described by classical hopping theories.

Based upon the 3PEPS photon echo experiment, it could be shown that the initial exciton transfer in systems exhibiting an intermediate electronic coupling is indeed of quantum coherent nature. An open question is, though, whether the initial coherent transfer is limited along a conformational subunit, i.e., whether the transfer is intramolecular, or whether the transfer proceeds between different conformational subunits, i.e., whether it is intermolecular. To answer this question, two-time anisotropy decay (TTAD) [70, 71] experiments have been carried out, again on MEH-PPV phases. The results show again that a quantum coherent transfer could be observed, which was interpreted as an intrachain transfer along the polymer backbone, rather than an interchain transfer between different chains of the polymer. The conclusion of this study was that the low frequency polarons of the polymer backbone play a significant role in the coherent exciton transport since they effectively reduce decoherence effects along the chain [75]. Theoretical calculations support the perspective of a quantum coherent transfer within the first 200 femtoseconds [76]. In the latter study, a description by the Redfield equations [77] was used for a model dimer system, involving certain limitations of the theoretical treatment (notably, Redfield theory assumes a separation of "system" and "bath" time scales which is not appropriate for the systems under study). These theoretical simulations showed that short-lived coherent transport tends to lead to a higher exciton dissociation yield. On the other hand, the same studies conclude that an increased disorder in functional materials implies shorter coherence lifetimes, which leads to energetic trapping effects, thereby limiting the excitons' ability to reach an interface and dissociate into free charge carriers [76].

The observations summarized above have led to a shift in perception, such that it is today generally accepted that coherent transfer of delocalised excitons takes place on the shortest time scale, of about 100-200 femtoseconds. This first, coherent phase is followed by localisation of the excitation on a conformational subunit of the polymer and a subsequent hopping type transport. The occurence of both quantum dynamical effects and a classical hopping type transfer to describe the exciton transport in such systems leads to the necessity of employing complementary quantum and classical-statistical techniques – and, eventually, multiscale modeling techniques – to describe the elementary transport processes in functional nano materials.

4 — The Born-Oppenheimer Approximation and Beyond

4.1 The Schrödinger Equation and Born-Oppenheimer Approximation

In order to describe a microscopic system appropriately, one has to go from a classical approach to an approach which is capable of treating systems quantum mechanically, according to their quantum nature. While a classical system is completely described by Newtons laws, the quantum mechanical counterpart has been proposed by Erwin Schrödinger in the beginning of the 20th century [78]. In the very general form, Schrödingers equation resembles wave-like equations of motions.

$$i\hbar\frac{\partial}{\partial t}\left|\Psi(\vec{r},\vec{R},t)\right\rangle = \hat{H}\left|\Psi(\vec{r},\vec{R},t)\right\rangle \tag{4.1}$$

Equation 4.1 states that a quantum mechanical system is fully described by the time dependent function $|\Psi(\vec{r},\vec{R},t)\rangle$. In this particular case, the wave function is a function of the electrons $\vec{r}$, the nuclei $\vec{R}$ and time t.

The operator $\hat{H}$ is the Hamiltonian of the system and contains all particle interactions. For a molecular system, the Hamiltonian looks as follows (in atomic units, i.e. $m_e = 4\pi\epsilon_0 = \hbar = 1$)

$$\hat{H} = \underbrace{\sum_k^M -\frac{1}{2m_k}\nabla_k^2}_{\hat{T}_n} + \underbrace{\sum_i^N -\frac{1}{2}\nabla_i^2}_{\hat{T}_e} - \underbrace{\sum_k^M\sum_i^N \frac{Z_k}{|\vec{r_i}-\vec{R_k}|}}_{\hat{V}_{en}} + \underbrace{\sum_k^M\sum_{l\neq k}^M \frac{Z_k Z_l}{|\vec{R_k}-\vec{R_l}|}}_{\hat{V}_{nn}} + \underbrace{\sum_i^N\sum_{j\neq i}^N \frac{1}{|\vec{r_i}-\vec{r_j}|}}_{\hat{V}_{ee}} \tag{4.2}$$

Here, the first two terms ($\hat{T}_n$ and $\hat{T}_e$) describe the kinetic energy of the nuclei and the electrons, respectively. The third term ($\hat{V}_{en}$) describes the electron-nuclei attraction, whereas the last two terms describe the nuclei-nuclei repulsion ($\hat{V}_{nn}$) and the electron-electron repulsion ($\hat{V}_{ee}$).

In the case that the Hamiltonian is not time-dependent, one can perform a separation ansatz of the wave function into a product of a spatial dependence $\vec{x}$ and a temporal dependence t.

$$|\Psi(\vec{x},t)\rangle = |\psi(\vec{x})\rangle \cdot |\theta(t)\rangle \,. \tag{4.3}$$

By inserting the wave function given in 4.3 into the Schrödinger equation 4.1 and performing some rearrangements, one obtains the time-independent Schrödinger equation

$$\hat{H}\,|\psi(\vec{r},\vec{R})\rangle = E\,|\psi(\vec{r},\vec{R})\rangle \,, \tag{4.4}$$

with the complete time dependent wave function $|\Psi(\vec{x},t)\rangle$ taking the form

$$|\Psi(\vec{x},t)\rangle = |\psi(\vec{x})\rangle \cdot e^{-iEt/\hbar}. \tag{4.5}$$

One can easily see that by substitution of equation 4.5 into equation 4.1, one obtains the time independent Schrödinger equation in 4.4.

The proposed Schrödinger equations 4.1 and 4.4 are only analytically solvable for small two body systems. Since chemical systems consist in most cases of more than two bodies, various approximations can be made. The most important approximation is called the Born-Oppenheimer [79] approximation and relies on the mass differences between electrons and nuclei ($m_k \approx 1800\ m_e$). The result of this approximation is that the electrons move in the static coulombic potential created by fixed nuclei positions. Since the nuclei are supposed to be spatially fixed, their kinetic energy is equal to zero. In the so-called adiabatic approximation, the potential energy V_{nn} (see equation 4.2) is a constant and one obtains an electronic Schrödinger equation with an Hamiltonian that only depends parametrically on the nuclei positions.

$$\hat{H}_{el}(R) = \hat{T}_e + \hat{V}_{ee} - \hat{V}_{en} \tag{4.6}$$

Using the above stated Hamiltonian and inserting it into equation 4.4 while using a wave function that is a product of an electronic term which depends only parametrically on the nuclei positions $\vec{R}$ and a nuclei term, i.e. $|\psi(\vec{r},\vec{R})\rangle = |\phi_e(\vec{r};\vec{R})\rangle \otimes |\varphi_n(\vec{R})\rangle$, one obtains the so-called Born-Oppenheimer surfaces.

$$\hat{H}_{el}(R)(|\phi_e(\vec{r};\vec{R})\rangle \otimes |\varphi_n(\vec{R})\rangle) = E(R)(|\phi_e(\vec{r};\vec{R})\rangle \otimes |\varphi_n(\vec{R})\rangle) \tag{4.7}$$

Due to the Born-Oppenheimer approximation it was possible to separate the electronic degrees of freedom from the nucleic degrees of freedom. With this ansatz it is now possible to construct the Born-Oppenheimer surfaces, which play a central role in chemistry and especially in parametrised model Hamiltonians used for quantum dynamical simulations.

In spite of the Born-Oppenheimer approximation, it is still not possible to solve systems consisting of more than one interacting electron due to the $\hat{V}_{ee}$ term. An approximation based on the Born-Oppenheimer formalism are the Hartree-Fock equations, which reduce the problem of solving a coupled N-dimensional differential equation into N uncoupled differential equations.

4.2 Beyond Born-Oppenheimer: Non-Adiabatic Effects

As pointed out in the previous section, the Born-Oppenheimer approximation is of crucial importance to study the dynamics of molecular systems. However, many phenomena in molecular physics cannot be described in the framework of the Born-Oppenheimer approximation, especially in photochemistry and photophysics. Such phenomena include the dynamics at avoided crossings and conical intersections. In this context, it is inevitable to go beyond the Born-Oppenheimer approximation to study excited-state quantum dynamical evolution of molecular systems.

By solving equations 4.6 and 4.7 one obtains a set of electronic eigenfunctions $\{\phi_i(\vec{r};\vec{R})\}$, which carry a parametric dependence on the nuclear coordinates. The total wave function

$\Psi(\vec{r}, \vec{R}, t)$ can be written as a sum over products of these electronic eigenfunctions and nuclear wave functions $\varphi_i(\vec{R})$,

$$\Psi(\vec{r}, \vec{R}, t) = \sum_i \varphi_i(\vec{R})\phi_i(\vec{r}; \vec{R}). \tag{4.8}$$

Inserting equation 4.8 into the time dependent Schrödinger equation 4.1, multiplication from the left by a chosen electronic eigenfunction $\phi_e(\vec{r}; \vec{R})$ and integration over the electronic degrees of freedom, one obtains coupled equations for the nuclear wave functions $\varphi(\vec{R})$.

$$\left[\hat{T}_n + E(R)\right] \varphi_j(\vec{R}) - \sum_i \hat{\Lambda}_{ji}\varphi_i(\vec{R}) = i\hbar\frac{\partial}{\partial t}\varphi_j(\vec{R}) \tag{4.9}$$

with the off-diagonal matrix elements

$$\hat{\Lambda}_{ji} = -\langle\phi_j(\vec{r}; \vec{R})|\hat{T}_n|\phi_i(\vec{r}; \vec{R})\rangle. \tag{4.10}$$

Equation 4.10 defines the nonadiabatic coupling operators, which are neglected when applying the Born-Oppenheimer approximation. One can see immediately from equation 4.10 that the operator $\hat{\Lambda}_{ji}$ describes the coupled motion and dynamical interaction of the electronic degrees of freedom and the nuclear degrees of freedom. In a more intuitive fashion, a matrix representation can be used, i.e. in this case for a two-state model,

$$i\hbar\frac{\partial}{\partial t}\begin{pmatrix}\varphi_1(\vec{R})\\ \varphi_2(\vec{R})\end{pmatrix} = \begin{pmatrix}\hat{T}_n + E_1(\vec{R}) & \hat{\Lambda}_{12}(\vec{R})\\ \hat{\Lambda}_{21}(\vec{R}) & \hat{T}_n + E_2(\vec{R})\end{pmatrix}\begin{pmatrix}\varphi_1(\vec{R})\\ \varphi_2(\vec{R})\end{pmatrix} \tag{4.11}$$

Note that equation 4.11 has been formulated in an adiabatic representation. The nonadiabatic couplings are calculated in various electronic structure packages. These couplings become very large at avoided crossings, and diverge at conical intersections.

For quantum dynamical simulations, it is often more intuitive and preferable from a numerical point of view to use a diabatic representation of the matrix formulation shown in equation 4.11, where the kinetic energy couplings $\hat{\Lambda}_{ij}(\vec{R})$ are replaced by potential

type couplings. To this end, the electronic wave functions are transformed by a unitary transformation,

$$\Phi^{dia}(\vec{r};\vec{R}) = S(\vec{R})\phi^{adia}(\vec{r};\vec{R}) \tag{4.12}$$

which leads to the following equation

$$i\hbar\frac{\partial}{\partial t}\begin{pmatrix}\tilde{\varphi}_1(\vec{R})\\ \tilde{\varphi}_2(\vec{R})\end{pmatrix} = \begin{pmatrix}\hat{T}_n + V_1^{dia}(\vec{R}) & V_{12}(\vec{R})\\ V_{21}(\vec{R}) & \hat{T}_n + V_2^{dia}(\vec{R})\end{pmatrix}\begin{pmatrix}\tilde{\varphi}_1(\vec{R})\\ \tilde{\varphi}_2(\vec{R})\end{pmatrix} \tag{4.13}$$

As mentioned above, the diabatic representation is generally more convenient, since the derivative couplings can be ill-behaved and show a singularity at conical intersections, such that integration is more difficult than for a continous function such as the potential type couplings in equation 4.13. Furthermore, the diabatic states have a well defined electronic character, which is more intuitive to understand than the adiabatic representation. For a more detailed derivation and discussion, see reference [80].

4.3 Diabatization Strategies

4.3.1 Quasi-diabatic representations

Following the discussion in the previous section, the question arises if it is always possible to define a adiabatic-to-diabatic transformation

$$\Phi^{dia}(\vec{r};\vec{R}) = S(\vec{R})\phi^{adia}(\vec{r};\vec{R}) \tag{4.14}$$

in such a way that the kinetic energy coupling terms $\hat{\Lambda}_{ji}$ are eliminated. An analysis by Mead and Truhlar [81] shows that a strictly diabatic basis does not exist, except for special cases such as diatomics or isolated two state systems in polyatomics. This results in the construction of a quasi-diabatic representation, where one constructs a non-unique basis which approximately eliminates the derivative couplings $\hat{\Lambda}_{ji}$.

In many situations of interest, it is justified to consider an isolated two-state system, focussing on a particular two-state avoided crossing or conical intersection. For this particular case, an adiabatic-to-diabatic transformation exists [81], as pointed out above. When performing a Taylor expansion of the potential energy surface around the intersection, only

the lowest order terms are found to be responsible for the singularity of the coupling terms $\hat{\Lambda}_{ji}$ [82]. This dominant contribution is thus eliminated via an unitary transformation, which yields as quasi-diabatic basis.

A wide variety of methods exists which perform a unitary transformation of the adiabatic representation to a quasi-diabatic representation [83–85], yielding besides the on-diagonal potential energies also the off-diagonal potential energy terms, see also equation 4.13. Molecular properties such as dipole moments are found to be smooth with respect to the chosen quasi-diabatic basis, further justifying the use of this particular basis.

4.3.2 Diabatization by projection onto reference states

The off-diagonal couplings are of crucial importance for the quantum dynamic modeling of the properties of functional polymeric materials. In the studies reported in the present work, these couplings were obtained by a diabatization procedure described by H. Tamura [86], who has been collaborating on the projects reported in this thesis. This procedure is especially suited for interacting molecular fragments, especially for cases where these fragments are not covalently bound.

In the approach of reference [86], the quasi-diabatic states Φ_I are expressed as mixtures of adiabatic states Ψ_J, i.e. $\Phi_1 = \Psi_1 cos\theta - \Psi_2 sin\theta$ and $\Phi_2 = \Psi_1 sin\theta + \Psi_2 cos\theta$, here shown for a two state system. The off-diagonal coupling is expressed as the energy gap between the adiabatic states Ψ_J, i.e. E_J and the adiabatic to quasi-diabatic state mixing θ. Written in matrix form

$$\begin{pmatrix} V_1 & V_{12} \\ V_{12} & V_2 \end{pmatrix} = \begin{pmatrix} E_1 cos^2\theta + E_2 sin^2\theta & \frac{1}{2}(E_1 - E_2)\sin 2\theta \\ \frac{1}{2}(E_1 - E_2)\sin 2\theta & E_1 cos^2\theta + E_2 sin^2\theta \end{pmatrix} \tag{4.15}$$

One possibility to solve equation 4.15 is by determining the state mixing θ via integration of the non-adiabatic coupling along the reaction coordinate R, i.e.

$$\frac{d\theta}{dR} = \langle \Psi_1 | \frac{\partial}{\partial R} | \Psi_2 \rangle \tag{4.16}$$

with the constraint that the state mixing θ is zero at the initial state and $\pi/2$ at the final state.

The method by H. Tamura [86] works as follows, e.g., for a molecular dimer:

(i) Reference states $\Phi_{ref,I}$ are prepared, which consist of molecular orbitals localized on the isolated molecules of the dimer, i.e. of the non-interacting system.

(ii) Adiabatic excited states Ψ_J of the interacting system are calculated.

(iii) The quasi-diabatic states Φ_I are expressed as a linear combination of the adiabatic states of the interacting system Ψ_J prepared at (ii) in such a way that the overlap between Φ_I and $\Phi_{ref,I}$ is maximized.

Thus, the diabatic states are represented as

$$\Phi_I = \sum_J C_{IJ}\Psi_J \qquad \text{with} \qquad C_{IJ} = \langle \Psi_J | \Phi_{ref,I} \rangle \tag{4.17}$$

Finally, the diabatic on-diagonal potential energy terms and off-diagonal diabatic coupling terms are obtained via

$$V_I^{dia}(\vec{R}) = \langle \Phi_I | \hat{H} | \Phi_I \rangle \qquad \text{and} \qquad V_{IJ}^{dia}(\vec{R}) = \langle \Phi_I | \hat{H} | \Phi_J \rangle \tag{4.18}$$

where $\hat{H}$ is the electronic Hamiltonian of the system.

5 — Electronic Structure Theory

This chapter provides an overview of the methods used in order to parametrize the model Hamiltonians for the quantum dynamic simulations. Therefore, a short introduction will be given to basic concepts in quantum chemistry such as the Hartree-Fock [87] equations. Furthermore, the concept of density functional theory [88, 89] and the linear response of a density [90, 91] to an external perturbation will be explained, as it is an efficient way to reduce computational costs of quantum chemical calculations. Special emphasis will be laid on the charge transfer error caused by the application of several TD-DFT functionals. The chapter will be concluded with a short overview over state of the art wave function based methods [92–94], which are commonly used as benchmark tools for density functional theory methods.

5.1 The Hartree-Fock Method

Even though the Born-Oppenheimer approximation reduces the computational effort for the calculation of molecular systems quite extensively, the remaining critical term is the electron-electron repulsion. Therefore, systems with more than two electrons (i.e. most systems of chemical relevance) are not analytically solveable. The Hartree-Fock method is capable of reducing this problem in an elegant fashion. The obtained Hartree-Fock equations are a result of the application of the variational principle to a Slater determinant. A Slater determinant is a wave function ansatz which obeys Pauli's antisymmetry principle. A time-independent wave function with coordinates $\vec{r_1}$, $\vec{r_2}$ and spin σ_1 and σ_2 can thus be expressed via a Slater determinant as follows (for a two electron problem):

$$|\phi_e(\vec{r},\sigma;\vec{R})\rangle^{SD} = \frac{1}{\sqrt{2!}}\begin{vmatrix}\chi_1(1) & \chi_2(1)\\ \chi_1(2) & \chi_2(2)\end{vmatrix} \tag{5.1}$$

The Pauli principle requires that a wave function changes sign upon changing the coordinates of the electrons. If one would use a simple product ansatz for a wave function, this property would not be fulfilled. For a simple Hartree product ansatz, i.e.

$$|\phi_e(\vec{r},\sigma;\vec{R})\rangle^{HP} = \chi_1(1)\chi_2(2) \tag{5.2}$$

one obtains for exchanging the coordinates (which is the same as if one would put electron one in orbital two and vice versa) of two electrons:

$$|\phi_e(\vec{r},\sigma;\vec{R})\rangle^{HP'} = \chi_1(2)\chi_2(1). \tag{5.3}$$

One can easily see that $|\phi_e(\vec{r},\sigma;\vec{R})\rangle^{HP} \neq -|\phi_e(\vec{r},\sigma;\vec{R})\rangle^{HP'}$, hence the Pauli principle is not valid. A Slater determinant therefore ensures that $|\phi_e(\vec{r},\sigma;\vec{R})\rangle^{SD} = -|\phi_e(\vec{r},\sigma;\vec{R})\rangle^{SD'}$.

When applying the variational principle to a Slater determinant (with the constrained that the spin orbitals χ are orthonormal to each other), one obtains the Hartree-Fock equations for the individual spin orbitals χ. For a single spin orbital, the equation looks as follows:

$$\left(\hat{h}(1) + \sum_{k\neq i}\left[\hat{J}_k(1) - \hat{K}_k(1)\right]\right)\chi_i(1) = \epsilon_i\chi_i(1) \tag{5.4}$$

with the Coulomb operator $\hat{J}_k$ and the exchange operator $\hat{K}_k$ defined as

$$\hat{J}_k(1)\chi_i(1) = \left[\int \chi_k^*(2) r_{12}^{-1}\chi_k(2)d\tau_2\right]\chi_i(1) \tag{5.5}$$

$$\hat{K}_k(1)\chi_i(1) = \left[\int \chi_k^*(2) r_{12}^{-1}\chi_i(2)d\tau_2\right]\chi_k(1) \tag{5.6}$$

The Coulomb operator in equation 5.5 describes the averaged potential that electron (1) in spin orbital i experiences. The exchange operator in equation 5.6 describes the exchange of electron (1) in orbital i with an arbitrary electron (2) in orbital k. From this point, two things should be made clear. First, the exchange operator 5.6 is a purely quantum mechanical phenomenon and does not have a classical analogon. Second, the Coulomb potential that a single particle experiences is a mean potential, as one can see from the summation

over all orbitals k in equation 5.4. Hence, the Hartee-Fock equation is a mean field equation since one particle experiences only an averaged potential of all other particles.

5.2 Density Functional Theory

An alternative to the Hartree-Fock method is the Density Functional Theory (DFT). Whereas the wave function depends on 4N variables (three spatial coordinates and a spin coordinate, with N being the number of electrons), the density of a given system of N electrons depends only on the three spatial coordinates. The relation between a density and a wave function is given as follows

$$\rho(\vec{r}) = N \int \cdots \int \langle \phi_e(\vec{r_1} \ldots \vec{r_N}, \sigma_1 \ldots \sigma_N; \vec{R}) | \phi_e(\vec{r_1} \ldots \vec{r_N}, \sigma_1 \ldots \sigma_N; \vec{R}) \rangle d\vec{r_2} \ldots d\vec{r_N} d\sigma_1 \ldots d\sigma_N \tag{5.7}$$

By integrating the density ρ with respect to the index r, one obtains the overall number of the electrons, i.e. $N = \int \rho(\vec{r}) d\vec{r}$. Very important for the applicability of density functional theory to quantum chemistry and molecular problems in general, are the two Hohenberg-Kohn theorems [95]. The first Hohenberg-Kohn theorem proofs the existence of an unique mapping of the ground state density of a given system to a wave function of a given system. In DFT, the electrons of a system interact with each other via an external potential. To show that a mapping of the wave function to a density is valid, consider the two potentials $\hat{V}_1$ and $\hat{V}_2$. Both of these potentials are supposed to lead to the same degenerate density $\rho_0(\vec{r})$. Furthermore, assume that

$$\begin{aligned} E_1 = \langle \psi_1 | \hat{H}_1 | \psi_1 \rangle &< \langle \psi_2 | \hat{H}_1 | \psi_2 \rangle \\ &= \langle \psi_2 | \hat{H}_2 | \psi_2 \rangle + \langle \psi_2 | \hat{H}_1 - \hat{H}_2 | \psi_2 \rangle \\ &= E_2 + \langle \psi_2 | V_1 - V_2 | \psi_2 \rangle \\ &= E_2 + \int \rho(\vec{r}) \left(V_1(\vec{r}) - V_2(\vec{r}) \right) d\vec{r}. \end{aligned} \tag{5.8}$$

By performing the same mathematical procedure for $E_2 = \langle \psi_2 | \hat{H}_2 | \psi_2 \rangle < \langle \psi_1 | \hat{H}_2 | \psi_1 \rangle$, one obtains

$$E_2 = E_1 + \int \rho(\vec{r}) \left(V_2(\vec{r}) - V_1(\vec{r}) \right) d\vec{r}. \tag{5.9}$$

Taking the sum of 5.8 and 5.9 yields the unequality $E_1 + E_2 < E_2 + E_1$, which is a *reductio ad absurdrum*. Unfortunately, the first Hohenberg-Kohn theorem does not predict how to obtain the density of a given system. Therefore, the second Hohenberg-Kohn theorem shows that a given trial density $\tilde{\rho}$ obeys the variational principle and hence, minimises the energy E of the system, resulting in E_0. Since the first Hohenberg-Kohn theorem proofed that there is a unique mapping of a given wave function to a density, one can write

$$E_0[\tilde{\rho}] = \langle \tilde{\psi} | \hat{H} | \tilde{\psi} \rangle \geq \langle \psi | \hat{H} | \psi \rangle = E_0[\rho_0]. \tag{5.10}$$

The second Hohenberg-Kohn theorem proofs that the energy calculated with a corresponding density is always larger then the exact energy E_0. Therefore, one can determine the density that yields the smallest energy.

To reduce the computational cost of the calculation of molecular systems, the so-called Kohn-Sham equations have been derived [96]. The Kohn-Sham equations resemble a Schrödinger type of equation, valid for a fictious system of non-interacting electrons with the constraint that the obtained density is the same density as for the interacting system. The corresponding Hamiltonian can be expressed as a sum of one electron operators and the resulting energy functional takes the following form:

$$\begin{aligned} E[\rho(\vec{r})] = \sum_i^N \left(\langle \chi_i | - \frac{1}{2} \nabla_i^2 | \chi_i \rangle - \langle \chi_i | \sum_k^M \frac{Z_k}{|\vec{r}_i - \vec{R}_k|} | \chi_i \rangle \right) \\ + \sum_i^N \langle \chi_i | \frac{1}{2} \int \frac{\rho(\vec{r'})}{|\vec{r}_i - \vec{r'}|} d\vec{r'} | \chi_i \rangle + E_{xc}[\rho(\vec{r})] \end{aligned} \tag{5.11}$$

The above stated equation is the Kohn-Sham equation. The first term on the right is the kinetic energy of the electrons. The second term is the Coulomb attraction between electrons and nuclei. The third term is the Coulomb repulsion between the density of electron i and the remaining density. The last term is the so-called exchange-correlation functional. It contains all non classical corrections to the electron-electron repulsion, such as exchange and the kinetic energy operator. Employing the same formalism to find the

set of orbitals χ that yield the lowest energy of the system, one obtains the differential equations for the Kohn-Sham orbitals

$$K_{\mu\nu} = \langle\chi_\mu| - \frac{1}{2}\nabla^2 - \underbrace{\sum_k^M \frac{Z_k}{|\vec{r_i} - \vec{R_k}|}}_{v_{ext}(\vec{r})} + \underbrace{\int \frac{\rho(\vec{r'})}{|\vec{r_i} - \vec{r'}|} d\vec{r'}}_{V[\rho,\vec{r'}]} + V_{xc}|\chi_\nu\rangle \tag{5.12}$$

The key difference between Hartree-Fock theory and DFT is that it is exact. One just has to know E_{xc} as a function of the density ρ. Hohenberg and Kohn proved that a functional of the density must exist and thus, a lot of effort has gone into finding a suitable exchange correlation functional. In reality there exists a wide variety of different functionals in order to solve that particular problem, like the well known DFT functional B3LYP [97].

5.3 Linear Response and The Charge Transfer Error

As it has been pointed out in the chapter before, the Hohenberg-Kohn theorems and also the Kohn-Sham equations are time-independent equations. They can be used to obtain a ground state density and the corresponding properties of a molecular system associated with such a density. In order to perform time-dependent calculations, analogue theorems to the Hohenberg-Kohn theorems and a set of working equations comparable to the Kohn-Sham equations have to be obtained. The time-dependent analogue to the first Hohenberg-Kohn theorem is the Runge-Gross theorem [98]. The Runge-Gross theorem is comparable to the first Hohenberg-Kohn theorem, except that an additional action functional of the time-dependent density is necessary, i.e. $A[\rho]$. For this particular action functional, the exact time-dependent density is a stationary point. Unfortunately, there seems to be a proof that the Runge-Gross theorem is erroneous and the use of the action functional is not appropriate to derive a set of time-dependent working equations [99].

However, the linear response formalism as an *ad hoc* extension of time-independent DFT can still be used to extract time-dependent information such as excited states. Due to the linear response formalism, the same exchange correlation functionals used for time-

independent DFT can be used for linear response DFT. First, the density will be expressed in terms of time-dependent Kohn-Sham orbitals $\chi(\vec{r},t) = c(t) \cdot \varphi(\vec{r})$

$$\rho(\vec{r},t) = \sum_i |\chi(\vec{r},t)|^2 = \sum_{i,j} \underbrace{c_i^*(t)c_j(t)}_{P_{ij}(t)} \varphi_i^*(\vec{r})\varphi_j(\vec{r}). \tag{5.13}$$

The time dependency of the system has been transferred to the so-called reduced density matrix $P_{ij}(t)$. Inserting the reduced density matrix $P_{ij}(t)$ into the time-dependent analogue of the Kohn-Sham equation, one obtains

$$i\frac{\partial}{\partial t}P_{ij}(t) = \sum_k \left(K_{ik}[\rho]P_{kj}(t) - P_{ik}(t)K_{kj}[\rho]\right) \tag{5.14}$$

with $K_{ij}[\rho]$ being the time-independent Kohn-Sham Hamiltonian of the ground state (see also equation 5.12). Suppose now that the external potential $v_{ext}(\vec{r})$ in equation 5.12 comprises of a small time-dependent perturbation $g(\vec{r},t)$, then $K_{ij}[\rho]$ (which becomes then time-dependent as well) and $P_{ij}(t)$ can be expanded in a time-series. Inserting these time-series into equation 5.14 and collecting all terms of zeroth, first, second and higher orders, one obtains several differential equations. The zeroth order terms yield the differential equations for ground state DFT. In first order, one obtains the differential equations for linear response DFT, which look like

$$i\frac{\partial}{\partial t}P_{ij}^{(1)}(t) = \sum_k \left[K_{ik}^{(0)}P_{kj}^{(1)} - P_{ik}^{(1)}K_{kj}^{(0)} + K_{ik}^{(1)}P_{kj}^{(0)} - P_{ik}^{(0)}K_{kj}^{(1)}\right] \tag{5.15}$$

The first-order change of the Kohn-Sham Hamiltonian $K_{ij}^{(1)}$ is given by

$$K_{ij}^{(1)} = g_{ij}(\vec{r},t) + \Delta F_{ij}^{(0)}. \tag{5.16}$$

The first-order change for the reduced density matrix $P_{ij}^{(1)}(t)$ are non-zero only if i refers to an occupied and j to an unoccupied orbital, which is caused by the idempotency relation ($\rho^2 = \rho$). As a result, equation 5.15 splits into two coupled equations which are complex conjugate to each other, i.e. $P_{ij}^{(1)}(t) = P_{ji}^{(1)*}(t)$. Taking the Fourier transformation of these

equations, one obtains the TD-DFT working equations. For a better understanding, the indices i, j label occupied orbitals whereas the indices a, b label virtual orbitals.

$$\begin{aligned}\omega\Delta P_{ia}(\omega) = (\epsilon_a - \epsilon_i)\Delta P_{ia}(\omega) + \sum_{jb}\left[\langle aj|ib\rangle + \langle aj|\delta v_{xc}|ib\rangle\right]\Delta P_{jb}(\omega) \\ + \sum_{jb}\left[\langle ab|ij\rangle + \langle ab|\delta v_{xc}|ij\rangle\right]\Delta P_{bj}(\omega)\end{aligned} \tag{5.17}$$

and

$$\begin{aligned}-\omega\Delta P_{ia}(\omega) = (\epsilon_a - \epsilon_i)\Delta P_{ia}(\omega) + \sum_{jb}\left[\langle ib|aj\rangle + \langle ib|\delta v_{xc}|aj\rangle\right]\Delta P_{jb}(\omega) \\ + \sum_{kl}\left[\langle ij|ab\rangle + \langle ij|\delta v_{xc}|ab\rangle\right]\Delta P_{jb}(\omega)\end{aligned} \tag{5.18}$$

The above states equations 5.17 and 5.18 can be rewritten as a pseudo eigenvalue equation, also known as the Casida equations [100]

$$\begin{pmatrix} A & B \\ B^* & A^* \end{pmatrix}\begin{pmatrix} \Delta P_{ia} \\ \Delta P_{ai} \end{pmatrix} = -\omega\begin{pmatrix} 1 & 0 \\ 0 & -1 \end{pmatrix}\begin{pmatrix} \Delta P_{ia} \\ \Delta P_{ai} \end{pmatrix} \tag{5.19}$$

with the matrix elements A and B defined as

$$A_{ia,jb} = (\epsilon_a - \epsilon_i)\delta_{ij}\delta_{ab} + \langle ia|jb\rangle + \langle ia|\delta v_{xc}|jb\rangle \tag{5.20}$$

$$B_{ia,jb} = \langle ia|bj\rangle + \langle ia|\delta v_{xc}|bj\rangle \tag{5.21}$$

Taking a closer look at equation 5.20, one can gain some fundamental insight into TD-DFT. The first term of $A_{ia,jb}$ describes the energy difference between an occupied and a virtual orbital to which the excitation occurs. The second term arises from the response of the Coulomb integral $\hat{J}$, see also equation 5.5. The last term describes the linear response of the exchange-correlation functional v_{xc}. Within the time-dependent Hartree-Fock scheme, the last term would correspond to the response of the exchange integral $\hat{K}$ (equation 5.6). From equation 5.20 and 5.21 one can also see why the TD-DFT scheme fails to accurately predict charge transfer energies and states. Assume that an electron is transfered from the occupied orbital i located on molecule 1 to the virtual orbital a located on molecule 2. If the spatial overlap between those two orbitals is zero, then the product $\langle ia|$ is also zero. Hence, the second and third term in equation 5.20 are zero and the only quantity that remains is the difference in orbital energies, at least for particular exchange correlation

functionals, which is a fairly bad first estimate. To overcome these drawbacks, hybrid approaches combining the linear response of density functional theory and Hartree-Fock theory have been developed. Equations 5.20 and 5.21 are then modified to

$$\begin{aligned} A_{ia,jb} &= (\epsilon_a - \epsilon_i)\delta_{ij}\delta_{ab} + \langle ia|jb\rangle - c_{HF}\langle ij|ab\rangle + (1 - c_{HF})\langle ia|\delta v_{xc}|jb\rangle \\ B_{ia,jb} &= \langle ia|bj\rangle - c_{HF}\langle ib|aj\rangle + (1 - c_{HF})\langle ia|\delta v_{xc}|bj\rangle \end{aligned} \tag{5.22}$$

In addition to equations 5.20 and 5.21, the hybrid approach shown in equation 5.22 introduces now the response of the Hartree-Fock exchange. The magnitude to which this Hartree-Fock exchange is included in hybrid TD-DFT functionals is determined by the coefficient c_{HF}, which depends on the used hybrid exchange-correlation functional. A detailed derivation of the linear response TD-DFT equations can be found in reference [91].

5.4 Post Hartree-Fock Methods

As it has been outlined in the previous section, time-dependent Density Functional Theory (TD-DFT) is not a suitable approach to treat charge transfer states in a satisfying manner. In order to overcome the drawbacks of TD-DFT, the focus of this section is put on Post-Hartree-Fock methods, i.e. methods that require a converged Hartree-Fock wave function. These self-consistent Hartree-Fock wave functions are used as a starting point for different methods such as Møller-Plesset perturbation theory (MP) [101], Coupled-Cluster theory (CC) [102] or the Algebraic Diagrammatic Construction (ADC) [103]. Here we will focus on the usage of the ADC method to second order, i.e. ADC(2). The reason for focussing on ADC(2) is that it is a reliable and accurate method to determine excited states. Even though CC with perturbatively corrected double excitations (CC2) yields reliable results and sometimes even better results then ADC(2), it is not the method of choice here. The reason is that CC2 treats double excitations only perturbatively, while ADC(2) treats double excitations explicitly.

The easiest way to derive the ADC(2) equations is via the intermediate state representation (ISR) [104]. The intermediate states $|\Psi_I^{\#}\rangle$ are orthogonalised with respect to the ground state and all other states obtained from applying the excitation operator $\hat{C}_I$ to the ground state $|\Psi_0\rangle$. The excitation operator looks as follows

$$\hat{C}_I \in \left\{\hat{c}_a^\dagger \hat{c}_i; \hat{c}_b^\dagger \hat{c}_j \hat{c}_a^\dagger \hat{c}_i, a < b, i < j; \ldots\right\} \tag{5.23}$$

Applying the excitation operator $\hat{C}_I$ on some wave function, one obtains all classes of singly, doubly, etc. excited states, i.e. $|\Psi_I^{\#}\rangle = \hat{C}_I|\Psi_0\rangle$. As it has been mentioned before, the states $|\Psi_I^{\#}\rangle$ are neither orthogonal to each other nor are they orthogonal to the ground state. A step wise Gram-Schmidt orthogonalisation of these states has to be performed in order to obtain orthonormal states. Along with these intermediate states, a shifted Hamiltonian matrix $\hat{H} - E_0^N$ is constructed.

$$M_{I,J} = \langle\tilde{\Psi}_I|\hat{H} - E_0^N|\tilde{\Psi}_J\rangle \tag{5.24}$$

Here, $|\tilde{\Psi}_I\rangle$ labels a Gram-Schmidt orthogonalised intermediate state. By choosing now the Nth order Møller-Plesset ground state as the starting point for the calculation of the shifted Hamiltonian matrix, one arrives at the Nth order ADC(n) equation. Diagonalising equation 5.24 yields the ADC(n) eigenvalues and the corresponding eigenvectors. The eigenvectors are needed for further calculation of observables, such as transition dipole moments and oscillator strength. In general, the expectation value of any operator is defined as

$$\langle\hat{O}\rangle_{mn} = \langle\Psi_m|\hat{O}|\Psi_n\rangle \tag{5.25}$$

Due to the diagonalisation of equation 5.24, one obtains the corresponding eigenvectors $X_{I,n}$ of the corresponding intermediate state $\tilde{\Psi}_I$. By multiplication of the eigenvector with the corresponding intermediate state basis, one obtains the excited state wave functions $|\Psi_n\rangle$

$$|\Psi_n\rangle = \sum_I X_{I,n}|\tilde{\Psi}_I\rangle \tag{5.26}$$

By inserting the completeness relation of quantum mechanics, i.e. $\sum_I |\tilde{\Psi}_I\rangle\langle\tilde{\Psi}_I|$, into equation 5.25 and using equation 5.26, one obtains an expression for the calculation of expectation values in terms of the eigenvectors of the shifted Hamiltonian

$$\langle\hat{O}\rangle_{mn} = X_m^\dagger \hat{O} X_n. \tag{5.27}$$

After outlining the principles of the ADC calculation scheme, it is worth to discuss the differences between ADC and other excited states methods, e.g. coupled cluster in particular. The main disadvantage of the CC approach is the calculation of excited state properties. While all available CC methods such as equation-of-motion coupled cluster (EOM-CC) or coupled cluster linear response (CCLR) are size-consistent, the main drawback is the non-hermiticity. This leads to a twofold wave function representation, one *left* and *right* eigenvector as solution of the CC secular matrix. In contrast, the ADC methods are Hermitian and fully size-consistent and hence, require the calculation of the ADC secular matrix only once. With respect to scaling, both CC(2) and ADC(2) scale with n^5 (with n being the number of the orbitals), resulting in the same computational effort for the computation of the excited states.

It should be emphasized that while the calculation of excited states is more efficient for the ADC scheme, the treatment of the ground state wave function $|\Psi_0\rangle$ is better for CC methods due to the direct accessibility of the ground state wave function within the CC scheme. As it has been pointed out earlier, the ground state wave function for the ADC(n) scheme is represented by the corresponding perturbative treatment of the ground state wave function, i.e. the MP(n) ground state. This hinders the calculation of molecules with a strong multi-reference ground state character, such as molecules with a low HOMO-LUMO gap. Here, CC methods might be more advantageous due to the usage of the corresponding CC ground state wave function.

6 — Dynamical Methods

In order to follow the time evolution of a molecular system, one first has to answer the question which time and length scales one is interested in. If one is interested in atomic length and time scales, one has to resort to deterministic methods such as quantum dynamics or molecular dynamics. In these deterministic methods, typical time scales range from attoseconds and femtoseconds (quantum dynamics) to picoseconds or microseconds (classical molecular dynamics). These methods require the calculation of either the wavefunction or else positions and momenta for a given trajectory at each time point. This can be very challenging as the amount of information one obtains becomes very large. Hence, one is restricted to the study of small molecular systems. For example, in the context of exciton migration, only small moleuclar lattices can be studied.

On the other hand, if one wants to study mesoscopic or macroscopic observables, one has to use stochastic methods, such as Monte Carlo theory. In these stochastic methods, the positions and momenta are random variables which define a point in phase space. To gather information about macroscopic observables one has to adequately sample the phase space of a given system.

In the following, a brief outline of the relevant deterministic and stochastic methods employed in this thesis will be presented. Also, the differences between the various methods will be highlighted and discussed.

6.1 Quantum Dynamics and the Multi-Configuration Time-Dependent Hartree Method

The previous section dealt with solving the time-independent Schrödinger equation (TDSE) in order to obtain information about the distribution of energy levels, the construction of potential energy surfaces, and properties like bond lengths, dipole moments, etc. In the present section, we are concerned with the solution of the time dependent Schrödinger equation,

$$i\hbar\frac{\partial}{\partial t}\Psi(\vec{x},t) = \hat{H}\Psi(\vec{x},t) \tag{6.1}$$

where $\vec{x}$ typically refers to a set of nuclear coordinates. Eq. (6.1) describes the time evolution of non-stationary states, i.e., wavepackets – coherent superpositions of the system's eigenstates – that are created in pulsed optical laser experiments. Solutions to the time-dependent Schrödinger equation enable us to visualize the movement of wavepackets in many dimensions.

6.1.1 Numerical Representation of the Wave function

The numerical solution of the time-dependent Schrödinger equation is feasible by representing the time-evolving wave function on a multidimensional discretized grid. However, this strategy is limited to few degrees of freedom, due to the exponential scaling of the procedure with dimensionality. Therefore, more approximate methods need to be considered. Among these, the time-dependent Hartree approach is a very approximate, single-configurational scheme. The multi-configurational time-dependent Hartree (MCTDH) approach plays an outstanding role since this scheme interpolates between the exact solution for small systems, and approximate solutions for large systems.

To give an overview, the following approaches are most relevant in our context:

i) Standard approach: Expansion of the wave function in a time-independent product basis,

$$\begin{aligned}\Psi(x_1, x_2, \ldots, x_N, t) &= \sum_{i_1}^{K_1}\sum_{i_2}^{K_2}\ldots\sum_{i_N}^{K_N} A_{i_1,i_2,\ldots,i_N}(t)\,\chi_{i_1}^{(1)}(x_1)\chi_{i_2}^{(2)}(x_2)\ldots\chi_{i_N}^{(N)}(x_N) \\ &= \sum_{i_1}^{K_1}\sum_{i_2}^{K_2}\ldots\sum_{i_N}^{K_N} A_{i_1,i_2,\ldots,i_N}(t)\prod_{n=1}^{N}\chi_{i_n}^{(n)}(x_n) \qquad (6.2)\end{aligned}$$

Based on the above form of the wave function, differential equations for the time-dependent coefficients are formulated. This scheme scales exponentially as a function of the number of degrees of freedom, and is typically able to handle 5-6 degrees of freedom.

ii) Time-dependent Hartree (TDH) approach: Representation of the wave function as a single configuration with a time-evolving coefficient and time-evolving so-called single particle functions (SPFs) for each degree of freedom,

$$\begin{aligned}\Psi(x_1, x_2, \ldots, x_N, t) &= A(t)\,\phi_1(x_1, t)\phi_2(x_2, t)\ldots\phi_N(x_N, t) \\ &= A(t)\prod_{i=1}^{N}\phi_i(x_i, t) \qquad (6.3)\end{aligned}$$

This scheme scales linearly as a function of the number of degrees of freedom and is therefore computationally advantageous. However, the method is a mean-field scheme that is not able to describe correlations correctly.

iii) Multi-configuration Time-dependent Hartree (MCTDH) approach: Representation of the wave function as a sum of TDH type configurations,

$$\Psi(x_1, x_2, \ldots, x_N, t) = \sum_{i_1}^{K_1}\sum_{i_2}^{K_2}\ldots\sum_{i_N}^{K_N} A_{i_1,i_2,\ldots,i_N}(t)\prod_{n=1}^{N}\phi_{i_n}^{(n)}(x_n, t) \qquad (6.4)$$

This form of the wave function, which employed time-dependent coefficients and time-dependent basis functions (SPFs), combines the merits of the standard approach and the time dependent Hartree approach. Indeed, this method turns out to be capable of producing accurate results for high-dimensional, correlated systems. Since the MCTDH method is the "workhorse" in the quantum simulations shown in the following chapters, we will

address this approach in some more detail below.

Before proceeding, we point out that equations of motion can be derived in all of the three cases from the time-dependent variational principle, i.e., the Dirac-Frenkel variational principle,

$$\langle \delta\Psi | \hat{H} - i\frac{\partial}{\partial t} | \Psi \rangle = 0 \tag{6.5}$$

where $\delta\Psi$ refers to the linear variation of the wave function, involving time-dependent coefficients and/or time-dependent basis functions.

6.1.2 The Multi-configuration Time-Dependent Hartree Approach

This section presents the equations of motion of the MCTDH approach. A detailed derivation and review over the MCTDH method can be found in references [105, 106].

For ease of notation, we re-write the wave function of Eq. (6.4) in two different forms. First,

$$\Psi(x_1, x_2, \ldots, x_N, t) \;=\; \sum_I A_I(t)\Phi_I(x_1, x_2, \ldots, x_N, t) \tag{6.6}$$

where the multi-index $I = (i_1, i_2, \ldots, i_N)$ was introduced, along with the configurations $\Phi_i(x_1, x_2, \ldots, x_N, t)$.

Second, we re-write Eq. (6.4) in the form

$$\Psi(x_1, x_2, \ldots, x_N, t) \;=\; \sum_i \phi_i^{(\kappa)}(x_\kappa)\Psi_i^{(\kappa)}(x_1, \ldots x_{\kappa-1}x_{\kappa+1}\ldots x_N) \tag{6.7}$$

where the SPFs $\phi_i^{(\kappa)}$ are multiplied by the so-called single-hole functions (SHFs) $\Psi_i^{(\kappa)}$ that absorb all information regarding the remaining degrees of freedom.

With these definitions, the equations of motion of the MCTDH method, derived from the Dirac-Frenkel variational principle, read as follows:

$$i\dot{A}_J(t) = \sum_L \langle \Phi_J(\vec{x},t)|\hat{H}|\Phi_L(\vec{x},t)\rangle A_L(t) \tag{6.8}$$

$$i\dot{\phi}^{(\kappa)}_{j_\kappa}(\vec{x},t) = (1-P^{(\kappa)})(\rho^{(\kappa)})^{-1}\langle\hat{H}\rangle^{(\kappa)}\phi^{(\kappa)}_{j_\kappa}(\vec{x},t). \tag{6.9}$$

with the projector within the κth subspace,

$$P^{(\kappa)} = \sum_{j=1}^{n_\kappa} |\phi^{(\kappa)}_j\rangle\langle\phi^{(\kappa)}_j| \tag{6.10}$$

the reduced density matrix in the κth subspace,

$$\rho^{(\kappa)}_{jl} = \langle\Psi^{(\kappa)}_j|\Psi^{(\kappa)}_l\rangle \tag{6.11}$$

and the mean-field Hamiltonian operator,

$$\langle\hat{H}\rangle^{(\kappa)} \equiv \langle\hat{H}\rangle^{(\kappa)}_{jl} = \langle\Psi^{(\kappa)}_j|\hat{H}|\Psi^{(\kappa)}_l\rangle \tag{6.12}$$

Note that if one uses a complete basis of SPFs, the r.h.s. of the EOM for the SPFs is zero, and one obtains the exact result in a time-independent basis set.

The density matrix $\rho^{(\kappa)}$ is similar to the one-particle density commonly used in electronic structure theory. Diagonalisation of the density matrix yields the so called natural populations and natural orbitals, which can be used as a tool to check whether a calculation is converged.

The mean fields Hamiltonian shown in equation 6.12 is also defined via the SHFs. Expressing the Hamiltonian with the aid of the SHFs, one obtains the mean field expectation value except for the κth degree of freedom. In conjunction with equation 6.9, this means that the wave function $\phi^{(\kappa)}_{j_\kappa}(\vec{x},t)$ experiences a field caused by all other remaining degrees of freedom, similar to the mean field approach in Hartee-Fock theory.

6.1.3 Multi-Layer MCTDH

Even though the MCTDH method is very efficient compared to the standard method, it only allows a propagation of up to 20-100 degrees of freedom and only a few electronic states (generally using the so-called multi-set formulation).

In comparison with the standard method, the MCTDH method does not eliminate the exponential scaling problem, but it significantly reduces the subspace dimensions for which the exponential scaling occurs. The key reason for the more efficient scaling of the MCTDH method in comparison with the standard method is the use of a "second layer" in the wave function representation, since the SPFs (in the "first layer") are in turn represented in a time-independent basis (i.e., the "second layer").

The "layered" approach can be used to extend the MCTDH wave function to even more layers with time-dependent coefficients. This results in the so-called Multilayer MCTDH (ML-MCTDH) method, which allows to treat up to 1000 degrees of freedom [107]. The ML-MCTDH wave function is a modified MCTDH wave function, which looks as follows:

$$\Psi(\vec{x},t) = \sum_{j_1 \dots j_f}^{N} A_{j_1}(t) \dots A_{j_f}(t) \prod_{\kappa}^{f} \phi_{j_\kappa}^{(\kappa)}(\vec{x},t) \tag{6.13}$$

where the SPFs are now representated in a second layer of time-dependent 2nd-layer SPFs,

$$\phi_{j_\kappa}^{(\kappa)}(\vec{x},t) = \sum_{i_1 \dots i_f}^{N} B_{i_1}(t) \dots B_{i_f}(t) \prod_{\kappa}^{f} \chi_{i_\kappa}^{(\kappa)}(\vec{x}',t) \tag{6.14}$$

The first layer wave function Eq. (6.13) is the same as in the standard MCTDH method. Whereas in standard MCTDH, the single particle functions ϕ are expressed in terms of a primitive basis, the single particle functions in the ML-MCTDH method are expressed in another set of single particle functions χ. This recursive scheme can in principle be extended to a huge number of layers. In combination with the multi-dimensional problem under investigation, it is possible to construct a variety of different layering schemes for the ML-MCTDH wave function. The partitioning often corresponds to the "natural" partitioning of the system (e.g., if the system is defined in terms of a number of electronic states or lattice sites), but often trial-and-error is necessary to obtain the best partitioning scheme.

In the subsequent chapters following the introductory part, a diagrammatic representation of the ML-MCTDH wave function will be shown for the respective simulations. In these representations, each node represents a set of vectors of coefficients which are connected to each other without loops. This allows for an efficient graphical representation of the ML-MCTDH wave function.

6.2 Monte-Carlo Theory

In contrast to the deterministic theory behind the previously proposed quantum dynamical methods, statistical methods have also been employed in this thesis. In particular the Kinetic Monte Carlo (KMC) [89] theory has been used to study charge carrier and exciton transport. One important point is that by going to the macroscopic scale, one has to be aware that the point of view on the dynamics changes as well. For deterministic theories one has the full resolution of position and momenta for a given trajectory and hence, gets information about the detailed dynamics. In stochastic theories such as KMC, one specifies at which time the configuration in phase space changes from one configuration to another. The fundamental equation that has to be solved is the so called Master Equation,

$$\frac{dP_\alpha}{dt} = \sum_\beta \left[W_{\alpha\beta}P_\beta - W_{\beta\alpha}P_\alpha\right] \tag{6.15}$$

In equation 6.15 t is the time, α and β are arbitrary configurations in phase space with their corresponding probabilities P_α and P_β. $W_{\alpha\beta}$ and $W_{\beta\alpha}$ are the transition probabilities to go from one point in phase space to another and vice versa. As one can see, the Master Equation is a gain/loss equation. Summing equation 6.15 with respect to time for all configurations α, i.e. $\sum_\alpha \frac{dP_\alpha}{dt}$ one can see that the total probability is conserved.

The derivation of equation 6.15 is straightforward and can be accomplished by the classical Hamiltonian's equations of motion. The probability P of finding a configuration α in the phase space density ρ at any time is given by

$$P_\alpha(t) = \int_{R_\alpha} \frac{\rho(\mathbf{p},\mathbf{q},t)}{h^D} d\mathbf{p}d\mathbf{q} \tag{6.16}$$

Here, the integration is over the region R_α that corresponds to a discretized configuration α. As a result, the explicit information about individual trajectories containing position

and momenta are not important. Since we lose information about the phase space density $\rho(\mathbf{p}, \mathbf{q}, t)$, it is only possible to define a probability that the system is in a certain configuration α. Furthermore, h^D shows up in the denominator, which is Planck's constant to the power of the dimensionality D of the system.

In order to obtain the equations of motion to monitor the time evolution of a system, equation 6.16 has to be differentiated with respect to time.

$$\frac{dP_\alpha}{dt} = \int_{R_\alpha} \frac{1}{h^D} \frac{\partial \rho(\mathbf{p}, \mathbf{q}, t)}{\partial t} d\mathbf{p} d\mathbf{q} \tag{6.17}$$

Since only the phase space density $\rho(\mathbf{p}, \mathbf{q}, t)$ depends on time, one can apply the Liouville equation for the time derivative of a density

$$\frac{\partial \rho}{\partial t} = -\sum_{i=1}^{D} \left[\frac{\partial \rho}{\partial q_i} \frac{\partial H}{\partial p_i} - \frac{\partial \rho}{\partial p_i} \frac{\partial H}{\partial q_i} \right] \tag{6.18}$$

where $H = \frac{p^2}{2m} + V(q)$ is the Hamiltonian of the system. Inserting 6.18 into equation 6.17, one obtains the following equation

$$\frac{dP_\alpha}{dt} = \int_{R_\alpha} \sum_{i=1}^{D} \frac{1}{h^D} \frac{\partial \rho}{\partial p_i} \frac{\partial H}{\partial q_i} d\mathbf{p} d\mathbf{q} - \int_{R_\alpha} \sum_{i=1}^{D} \frac{1}{h^D} \frac{\partial \rho}{\partial q_i} \frac{\partial H}{\partial p_i} d\mathbf{p} d\mathbf{q} \tag{6.19}$$

The first term of equation 6.19 becomes then

$$\int_{R_\alpha} \sum_{i=1}^{D} \frac{1}{h^D} \frac{\partial \rho}{\partial p_i} \frac{\partial H}{\partial q_i} d\mathbf{p} d\mathbf{q} = \sum_{i=1}^{D} \int_{-\infty}^{+\infty} \frac{1}{h^D} \frac{\partial \rho}{\partial p_i} d\mathbf{p} \int_{R_\alpha} \frac{\partial V}{\partial q_i} d\mathbf{q} \tag{6.20}$$

By making the assumption that the region R_α is defined entirely by the positions $\mathbf{q}$, one can extend the integration over the momenta to $\pm\infty$. This allows one to go from phase space to configuration space (see reference [108] for a detailed derivation). In turn, this means that equation 6.19 and 6.20 becomes zero.

$$\int_{-\infty}^{+\infty} \underbrace{\frac{1}{h^D} \sum_{i=1}^{D} \frac{\partial \rho}{\partial p_i} d\mathbf{p}}_{=0} \cdot \int_{R_\alpha} \frac{1}{h^D} \sum_{i=1}^{D} \frac{\partial V(q_i)}{\partial q_i} d\mathbf{q} = 0 \tag{6.21}$$

The remaining second term of equation 6.19 becomes then

$$\int_{R_\alpha} \sum_{i=1}^{D} \frac{1}{h^D} \frac{\partial \rho}{\partial q_i} \frac{\partial H}{\partial p_i} d\mathbf{p} d\mathbf{q} = \int_{R_\alpha} \sum_{i=1}^{D} \frac{1}{h^D} \frac{\partial}{\partial q_i} \left(\frac{p_i}{m_i} \rho \right) d\mathbf{p} d\mathbf{q} \tag{6.22}$$

Exploiting the divergence theorem for the integration over the coordinates, one obtains for the time derivative of the probability of configuration α

$$\frac{dP_\alpha}{dt} = - \int_{R_\alpha} dS \int_{-\infty}^{+\infty} \frac{1}{h^D} \sum_{i=1}^{D} n_i \dot{\mathbf{q}}_i \rho(\mathbf{p}, \mathbf{q}, t) d\mathbf{p} \tag{6.23}$$

In equation 6.23, the first integration is a surface integral over the area R_α. The second integral describes the flux through the surface S_α separating the region R_α from some other region R_β.

The final step in order to obtain the master equation proposed in equation 6.15 is to decompose the flux in two ways, once an inward flux and once an outward flux. This results in the following equation

$$\frac{dP_\alpha}{dt} = \sum_\beta \int_{S_{\alpha\beta}} dS \frac{1}{h^D} \left(\sum_{i=1}^{D} n_i \dot{\mathbf{q}}_i \right) \Theta \left(\sum_{i=1}^{D} n_i \dot{\mathbf{q}}_i \right) \rho(\mathbf{p}, \mathbf{q}, t) d\mathbf{p} \tag{6.24}$$

$$- \sum_\beta \int_{S_{\beta\alpha}} dS \frac{1}{h^D} \left(\sum_{i=1}^{D} n_i \dot{\mathbf{q}}_i \right) \Theta \left(\sum_{i=1}^{D} n_i \dot{\mathbf{q}}_i \right) \rho(\mathbf{p}, \mathbf{q}, t) d\mathbf{p} \tag{6.25}$$

Equation 6.25 has already some similarities to the master equation proposed above (6.15). The first term of equation 6.25 describes the flux from region R_β into region R_α, whereas the second term describes the opposite. Furthermore, Θ is the Heaviside step function.

One important point when calculating observables with stochastic methods like KMC is the validicty of the Ergodic hypothesis, meaning that every point in phase space can be reached with a single trajectory in the course of the time evolution. Alternatively, instead of having a long simulation time to ensure the ergodic hypothesis, it is also possible to calculate many independent trajectories with a shorter simulation time. This means that the time-averaged observable $\bar{O}$ should be equal to the phase space averaged observable $\hat{O}$.

$$\hat{O} = \frac{1}{N} \sum_{i=1}^{N} O(i) = \lim_{t \to \infty} \frac{1}{t} \int_0^t O(t) dt = \bar{O} \tag{6.26}$$

To ensure that the ergodic hypothesis in equation 6.26 is valid, one has to make sure that during the simulation time t, all possible configurations in phase space can be visited once. One can already see that one would have to run a simulation for $t = \infty$, which is numerically not possible. Therefore, one has to choose a simulation time (or equivalent a huge number of shorter trajectories) that are sufficiently representative for the global behaviour of the system.

One possible way to solve the master equation 6.15 is the First Reaction Method (FRM) algorithm. Even though there are a lot of different methods and algorithms to solve the master equation, the FRM has been successfully used for the simulation of charge carrier phenomena in photovoltaic devices [32, 109–112]. In FRM, an initial configuration i changes to another configuration j within the time interval Δt_{ij} according to

$$\Delta t_{ij} = -\frac{\ln r}{k_{ij}} \tag{6.27}$$

with r being a random number uniformally distributed between 0 and 1. The advantage of the FRM is the generation of a list of all possible changes for configuration i. From the generated list of possible events, the event with the shortest waiting time is going to happen. This also ensures that at every iteration, a change in configuration occurs and a new configuration in phase space is populated. In general, the propagation scheme for such a KMC calculation looks as follows:

1. Generate an initial configuration and set the time to some initial value
2. Generate a queue of events that are allowed to happen. Each event is associated with its characteristic waiting time Δt_{ij}
3. Choose the event with the shortest waiting time and perform the change in configuration
4. Go back to step 2 until the stop criterion is reached

This procedure can be applied to a variety of different events, ranging from exciton diffusion to exciton dissociation and exciton recombination. In particular, this scheme has been applied to the following events: (i) Exciton diffusion, (ii), exciton recombination, (iii) exciton dissociation, (iv) charge transfer, (v) charge collection.

At the end of a given simulation, the macroscopic observables can be calculated. In particular, the charge mobilities μ have been calculated, as they are defined via

$$\mu = \frac{d}{t \cdot F}. \tag{6.28}$$

Here, d is the traveled distance of the charge, from its point of origin (i.e. where the exciton was dissociated) to the electrode. t is the time until the charge was collected at the electrode and F is the applied electric field. The charge mobility has been calculated for every simulated charge and in the end, the average of all mobilities has been determined.

7 — Lattice Model Hamiltonians

In this section, we introduce a typical electron-hole lattice Hamiltonian employed for quantum dynamical simulations of photoinduced processes in aggregated functional materials. Our concept is to use a *first-principles* parametrized version of such a Hamiltonian in order to faithfully represent the excited-state properties of aggregate species. Accurate supermolecular calculations are usually not available for the system sizes of interest, such that a fragment-based representation – based on reasonably accurate calculations for monomer or oligomer fragments – is a sensible approach.

When constructing a lattice model [113–117], each lattice point typically represents a specific monomer (or else oligomer), which is characterised by its on-site potential energy terms as well as couplings to neighboring lattice points. The construction of these on-diagonal and off-diagonal potential terms – usually from electronic structure calculations for small oligomer species – is a crucial ingredient in the lattice model. In sections 4.2 and 4.3 the importance of these electronically on-diagonal and off-diagonal potential energy terms was highlighted. In particular, the off-diagonal potential-type coupling terms describe, e.g., excitation energy transfer and charge transfer processes.

From the perspective of molecular aggregates, the off-diagonal electronic coupling elements have a direct influence on the electronic stucture of aggregated chromophores. In this context, the difference between H- and J-aggregates [118] will be highlighted and explained in the context of so-called Frenkel states [37, 119].

7.1 Electron-Hole Lattice Model

In order to treat excitation energy transfer and charge transfer phenomena on equal footing, we use a lattice representation in an electron-hole (e-h) basis. Each lattice point

corresponds to a molecular fragment that carries a local excitation or a charge. To translate electronic structure information – typically from potential energy surface cuts of small oligomer species – to this electron-hole representation, a diabatization procedure has to be employed (see section 4.3). In figure 7.1, the construction of the e-h lattice representation is illustrated for two cases: (i) an oligothiophene tetramer which is discretized into four identical monomer sites, (ii) two stacked oligothiophene tetramers, where each tetramer is now taken as an individual oligomeric lattice site.

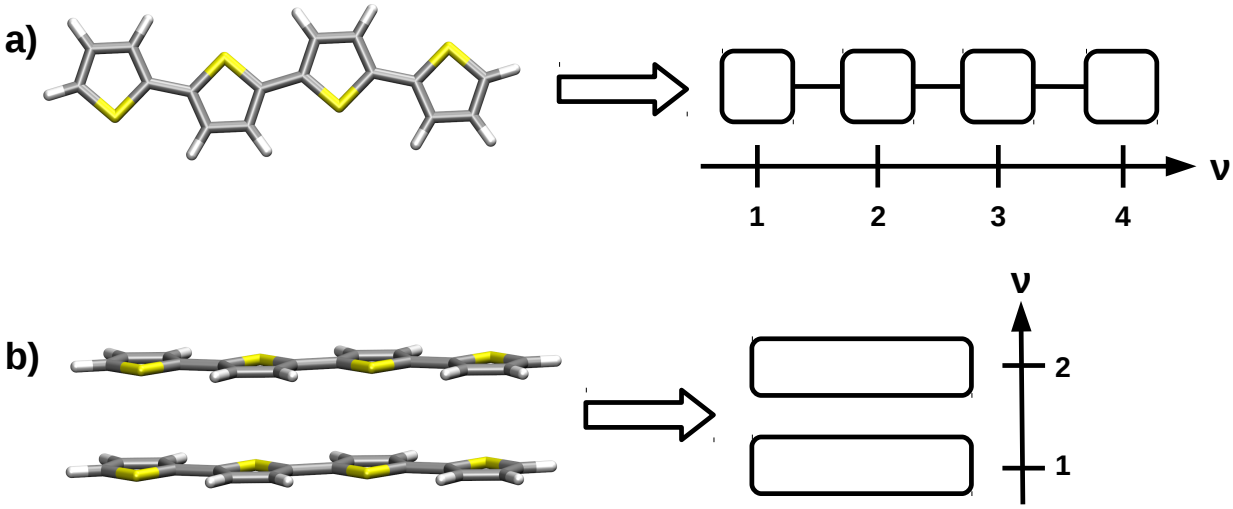

Figure 7.1: a) Sketch of a monomer resolved discretization of the electron-hole lattice Hamiltonian. b) Sketch of an oligomer resolved discretization of the electron-hole lattice Hamiltonian.

In the following, we will label e-h states $|\nu\mu\rangle$, with the convention that electrons are located at site ν while holes are located at site μ. Electrons and holes are usually allowed to occupy all sites of the lattice. Simultaneous occupation of the same lattice site corresponds to a Frenkel exciton configuration (i.e., a localized e-h state). Restrictions may apply if one is not dealing with homogeneous systems such as the oligothiophene tetramer shown above, but rather heterogeneous systems such as donor-acceptor systems (see chapter 8) where holes are located on the donor species while electrons are located on the acceptor species.

7.2 Frenkel Hamiltonian: H and J Aggregates

As has been mentioned in the previous section, discrete lattice points represent a specific site. The overall molecular Hamiltonian describing the system is therefore a sum of the invidivual site Hamiltonians, including off-diagonal coupling-type contributions, i.e.,

$$\hat{H} = \sum_{\nu\mu} \sum_{\nu'\mu'} \hat{H}_{\nu\mu\nu'\mu'} |\nu\mu\rangle\langle\nu'\mu'| \tag{7.1}$$

with

$$\hat{H}_{\nu\mu\nu'\mu'} = \delta_{\nu\nu'}\delta_{\mu\mu'} \left(\hat{H}^0_{\nu\mu\nu'\mu'}\right) + \hat{H}^{coup}_{\nu\mu\nu'\mu'}. \tag{7.2}$$

Equation 7.2 can be split up into an electronically diagonal zeroth-order part (first term) and an off-diagonal part containing electronic couplings describing excitation energy transfer (EET) as well as exciton to charge transfer couplings (second term). In particular, these terms look as follows

$$\hat{H}^0_{\nu\mu\nu\mu} = \hat{H}^{eh}_{\nu\mu\nu\mu} + \hat{H}^{vibr}_{\nu\mu\nu\mu}. \tag{7.3}$$

and

$$\hat{H}^{coup}_{\nu\mu\nu'\mu'} = \hat{H}^{EET}_{\nu\mu\nu'\mu'} + \hat{H}^{CT}_{\nu\mu\nu'\mu'} \tag{7.4}$$

As it has already been mentioned, equation 7.3 is electronically diagonal in the e-h basis specified earlier. The first term in this equation describes the intrinsic electron-hole interaction energy, i.e. the energetics of the system that can often be derived from an effective Coulomb barrier. The second term is related to vibronic contributions, arising from the coupling of the electronic subsystem to the vibrational ("phonon") subsystem. The potentials appearing in the second term of equation 7.3 can either be obtained by (i) a direct *ab initio* calculation of selected potential energy surface cuts and a subsequent diabatic mapping procedure [83–85] or (ii) from a linear vibronic coupling approach [80, 120, 121], as it will be shown later. Typically, the vibronic part of the Hamiltonian looks as follows

$$\hat{H}^{vibr}_{\nu\mu\nu\mu} = \delta_{\nu\nu'}\delta_{\mu\mu'} \sum_i \left(\frac{1}{2}\hat{p}_i^2 + \hat{V}_{i,\nu\mu}\right). \tag{7.5}$$

Equation 7.5 is the very general form of a vibrational Hamiltonian with the kinetic energy operator and a state-specific potential energy operator. As mentioned previously, the potential energy operator $\hat{V}$ can be obtained via different techniques, among which the linear vibronic coupling approach will be highlighted later.

The electronically off-diagonal part of the Hamiltonian, i.e. equation 7.4, contains two types of site-to-site couplings. First, there are Frenkel-type couplings between localized e-h pairs. Second, there are electron/hole transfer integrals, corresponding to the transfer of electrons and holes between different sites. Usually one assumes that only nearest neighbor couplings are relevant for the dynamical evolution of a system. In particular, the first term of equation 7.4 takes the explicit form of

$$\hat{H}^{EET}_{\nu\mu\nu'\mu'} = \delta_{\nu\mu}\delta_{\nu'\mu'}\left(\delta_{\nu'\nu+1}J + \delta_{\nu'\nu-1}J\right) \tag{7.6}$$

while the second term takes the form

$$\hat{H}^{CT}_{\nu\mu\nu'\mu'} = \delta_{\nu\nu'}\left(\delta_{\mu'\mu+1}t_{hole} + \delta_{\mu'\mu-1}t_{hole}\right) + \delta_{\mu\mu'}\left(\delta_{\nu'\nu+1}t_{elec} + \delta_{\nu'\nu-1}t_{elec}\right) \tag{7.7}$$

The explicit calculation of the excitonic coupling J occurring in equation 7.6 and the transfer integrals t_{hole} and t_{elec} occurring in equation 7.7 is of crucial importance to accurately model functional nano-structured materials [86].

Besides the accurate calculation of the excitonic coupling J appearing in equation 7.6, it is also crucial to determine the correct sign of the calculated coupling constant J. Depending on the sign of the excitonic coupling J, the chromophore is either of H-aggregate type or else of J-aggregate type [118]. This implies that the bright state, i.e. the state that is experimentally prepared due to a vertical excitation, is either higher or lower in energy than the monomeric state.

To highlight the above point, consider a general two-state system of the form

$$\hat{H} = \begin{pmatrix} \epsilon_{XT} & J \\ J & \epsilon_{XT} \end{pmatrix} \tag{7.8}$$

The eigenvalues are given as $E_{1/2} = \epsilon_{XT} \pm J$. Let us first consider the case $J > 0$. By inspecting the eigenvectors of this system, one notices that the eigenvector corresponding

to the higher energy state, i.e. $(\epsilon_{XT} + J)$, reads $\vec{E}_1 = (1, 1)^T$, while the eigenvector corresponding to the lower energy state, i.e., $(\epsilon_{XT} - J)$, reads $\vec{E}_2 = (1, -1)^T$. One can see that the eigenvector describing the lower energy state exhibits a nodal plane, while the eigenvector corresponding to the higher energy state does not. Transferring this picture to transition dipole moments for these two states, which are composed in an additive way of monomeric transition dipole moments, one can say that the oligomer transition dipole moments show constructive (in the case of $\vec{E}_1$) or destructive interference (in the case of $\vec{E}_2$). Now, if one assumes that the excitonic coupling J takes a negative value, the argument is reversed: One obtains as eigenvector for the higher energy state $\vec{E}_1 = (1, -1)^T$ and for the lower energy state $\vec{E}_2 = (1, 1)^T$.

Relating these observations to electronically coupled organic chromophores, one refers to an H-aggregate if the optically allowed transition takes the system to the higher excited state ($J > 0$), while an optically allowed excitation to the lower energy state corresponds to a J-aggregate ($J < 0$). The optical excitation in either an H aggregate or a J-aggregate also has a direct influence on the dynamical evolution of the system. In the case of an H-aggregate, the system carries a certain amount of excess energy, which can help to overcome energetic barriers. On the other hand, this energy can be dissipated in the course of internal conversion processes. For the same reason, bright states of H-aggregates often have a very short lifetime.

7.3 Vibronic Effects: Linear Vibronic Coupling Model

As has been mentioned earlier, the linear vibronic coupling (LVC) [121] model represents a simple approximation to the nonadiabatically coupled potential energy surfaces of the molecular system. The LVC approach is based on a shifted harmonic oscillator model, and is usually formulated in the normal mode basis. Here, one assumes that the photoexcitation of the normal mode in the ground state generates a wave packet in the Franck-Condon [122–124] region of the excited state, with the excited state being shifted from the ground state equilibrium geometry.

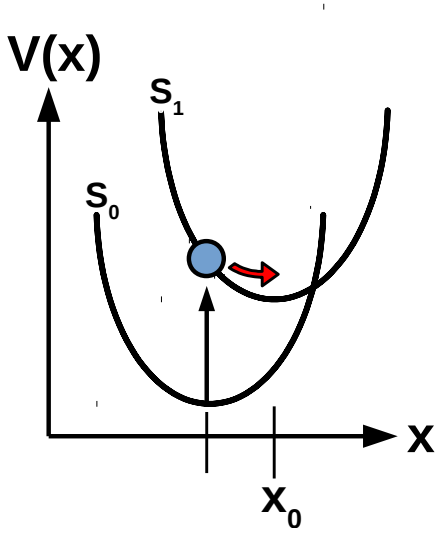

Figure 7.2: Sketch of the shifted harmonic oscillator approach used for the quantum dynamics in this chapter. A wave packet is excited from the optimised ground state to the Franck-Condon region in the excited state and can evolve free.

Figure 7.2 shows a sketch of the LVC scheme, also called the shifted harmonic oscillator approach. The overall potential is given as a sum of contributions of the ground state (S_0) and the excited state (here, S_1),

$$\begin{aligned}\hat{V}(x) &= \frac{1}{2}\omega x^2|S_0\rangle\langle S_0| + \frac{1}{2}\omega(x-x_0)^2|S_1\rangle\langle S_1| \\ &= \frac{1}{2}\omega x^2|S_0\rangle\langle S_0| + \left(\frac{1}{2}\omega x^2 - \omega x_0 x + \frac{1}{2}\omega x_0^2\right)|S_1\rangle\langle S_1| \\ &= \frac{1}{2}\omega x^2|S_0\rangle\langle S_0| + \left(\frac{1}{2}\omega x^2 + \kappa x + \Delta\right)\rangle|S_1\rangle\langle S_1| \qquad (7.9)\end{aligned}$$

where mass and frequency-weighted coordinates were used. In equation 7.9, the first term describes the non-shifted ground-state potential, whereas the remaining terms describe a shifted potential, with the linear coordinate dependent term κx, where κ is referred to as vibronic coupling constant. The last term in equation 7.9 is a vertical shift.

In order to obtain the vibronic coupling constant κ, one can either calculate the Franck-Condon gradient or else the optimized excited-state geometry (by geometry optimization). Within the LVC model, both give identical information about κ. Usually, one refers to ground state normal modes, such that the scalar product of the excited-state gradient and the normal-mode vector yields the vibronic coupling constant κ.

7.4 Effective-Mode Transformation

The effective-mode approach to study short-time dynamics in nonadiabatically coupled systems is based on previously introdcued linear vibronic coupling approach. The starting point for the derivation of an effective mode description are the vibronic coupling coefficients κ_i as well as the corresponding set of normal modes $\{x_i\}$ [125]. In the following, the effective mode decomposition will be explained for a two-state system. The LVC Hamiltonian, written in matrix formalism, looks as follows

$$\hat{H} = \sum_{i=1}^{N} \frac{\omega_i}{2} \left(\hat{p}_i^2 + \hat{x}_i^2\right) \mathbb{1} + \begin{pmatrix} \kappa_i^{(1)} x_i & \lambda_i^{(12)} x_i \\ \lambda_i^{(12)} x_i & \kappa_i^{(2)} x_i \end{pmatrix}. \tag{7.10}$$

where the diagonal entries of the matrix correspond to the shifted potentials of Eq. (7.9). Equation 7.10 shows the molecular Hamiltonian for an arbitrary two state system with N normal modes. Here, ω, $\hat{p}$ and $\hat{x}$ describe the frequency, momentum and position operator of a given normal mode, respectively. $\mathbb{1}$ is the unit matrix. Note that the given Hamiltonian also accounts for conical intersections, due to the coordinate dependence of the off-diagonal coupling term.

In order to reduce the dimensionality of the system from $N = N_{NM}$ normal modes to $N = N_{EM}$ effective modes, one has to apply an orthogonal coordinate transformation of the form $\boldsymbol{X} = \boldsymbol{T}\boldsymbol{x}$, with $\boldsymbol{T}$ being the transformation matrix [125, 126]. This scheme leads to a decomposition of a general Hamiltonian $\hat{H}$ into two terms:

$$\hat{H} = \hat{H}_{EM} + \hat{H}_{res} \tag{7.11}$$

Here, $\hat{H}_{EM}$ is the Hamiltonian containing the effective modes which couple directly to the electronic subsystem, with a dimensionality that is smaller compared to the full normal mode approach. The term $\hat{H}_{res}$ contains the residual modes which do not couple to the electronic subsystem, but to the effective modes. Due to the orthogonal transformation, the N_{EM} effective modes entirely define the coupling to the electronic subsystem. Thus, the effective Hamiltonian $\hat{H}_{EM}$ reads as follows.

$$\hat{H}_{EM} = \sum_{i=1}^{N_{EM}} \frac{\Omega_i}{2} \left(\hat{P}_i^2 + \hat{X}_i^2\right) \mathbb{1} + \begin{pmatrix} C_i^{(1)} X_i & \Lambda_i^{(12)} X_i \\ \Lambda_i^{(12)} X_i & C_i^{(2)} X_i \end{pmatrix} + \sum_{i,j=1,j>i}^{N_{EM}} d_{ij} \left(\hat{P}_i \hat{P}_j + \hat{X}_i \hat{X}_j\right), \tag{7.12}$$

with $N_{EM} < N_{NM}$. Comparing equations 7.10 and the first two terms of 7.12, one can easily see that both Hamiltonians describe the same physical behaviour of the system. The last term in equation 7.12 describes the bilinear coupling between the N_{EM} effective modes. The residual part of the Hamiltonian in equation 7.11 contains the remaining $N - N_{EM}$ residual effective modes and their bilinear coupling to the first layer of effective modes, which couple to the electronic subsystem.

$$\hat{H}_{res} = \sum_{i=N_{EM}+1}^{N} \frac{\Omega_i}{2} \left(\hat{P}_i^2 + \hat{X}_i^2 \right) \mathbb{1} + \sum_{i=1}^{N} \sum_{j=4, j>i}^{N} d_{ij} \left(\hat{P}_i \hat{P}_j + \hat{X}_i \hat{X}_j \right) \tag{7.13}$$

Along with the residual Hamiltonian shown in equation 7.13, additional transformations can be carried out. The subspace of the residual modes can now be coupled to the first layer of effective modes, described by equation 7.12 via different schemes:

- In the first scheme, the remaining residual bath is coupled to all effective modes, where the residual bath can be seen as a separate bath for the effective modes.
- The second scheme is closely related to a Mori-type description [127], where one creates a band-like structure of underlying residual baths. The dimensionality of the resulting Hamiltonian is a multiple of the first layer of effective modes. With each successive order, the dynamics of the system is captured on longer time scales.
- In the third and last scheme, one employs again a Mori-type description, but truncates the chain at a chosen order M. The remaining bath modes are then diagonalised and act as a dissipative bath for the M-th layer of effective modes.

The following figure shows a schematic representation of the three different schemes for a two effective mode approach. An overview of the different schemes can be found in references [128–130].

Figure 7.3a shows a graphical representation of the first scheme of the bath Hamiltonian. The diagonal terms represent the effective mode frequencies and the off-diagonal terms the effective mode couplings d_{ij}. Here, only the first two effective modes couple directly to the electronic subsystem, whereas the remaining effective modes act as a residual bath. The second mentioned scheme is shown in figure 7.3b and is related to a Mori-type description. The d_{ij} coupling matrix has a band diagonal form and the couplings between each subblock correspond to effective mode pairs. As more layers of effective-mode pairs are added, the better is the long-time description of the resulting dynamics. The last

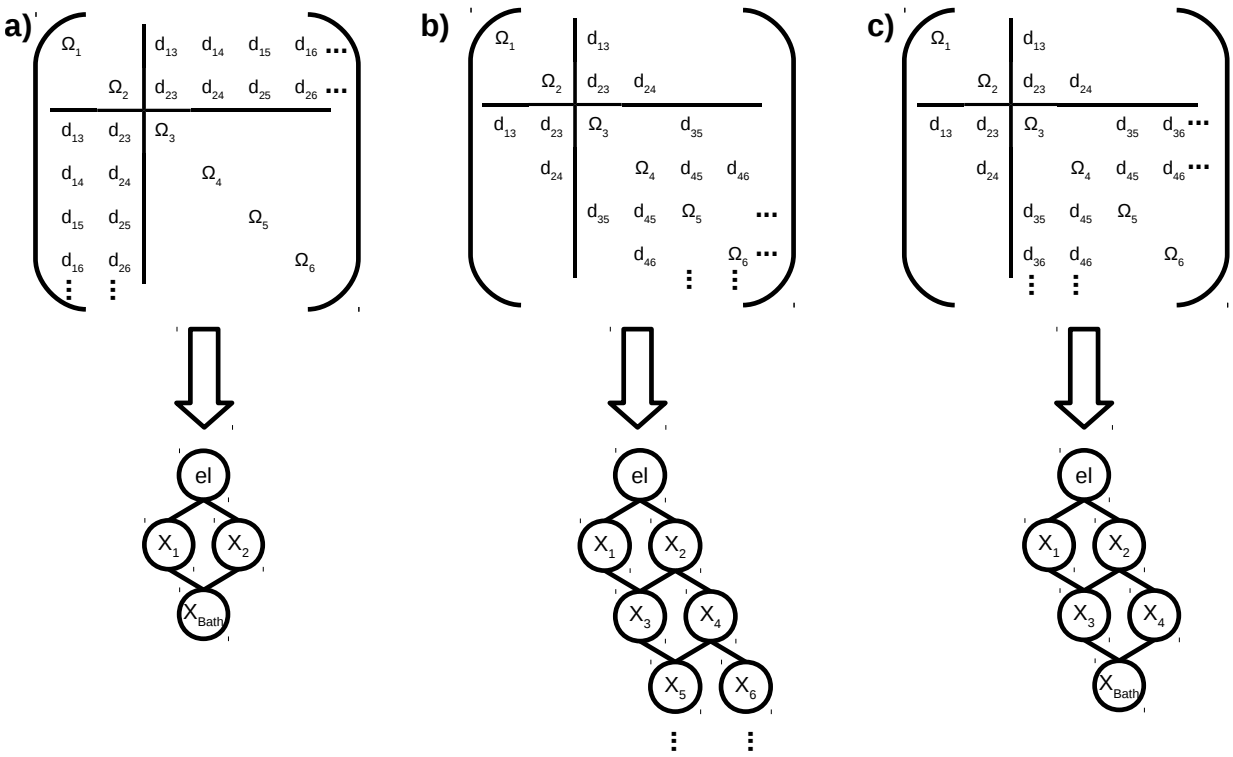

Figure 7.3: Sketch of the three different realisations of the decomposition into effective modes and residual modes. a) A secondary bath is coupled to the primary effective modes. b) Mori-type description of the effective mode construction. c) Truncated Mori-type chain with a Markovian closure.

scheme mentioned previously is schematically shown in figure 7.3c and can be understood as a combination of the first and second scheme shown in figures 7.3a and b, respectively. Here, the Mori chain is truncated at a certain order and the remaining bath modes are diagonalised in order to yield a dissipative residual bath.

The dynamical calculations employed in this thesis have been performed using the third scheme. The simulations employing the effective mode description shown in the first half of this chapter have been done for various truncations of the residual effective mode chain. The chains have usually been truncated at low orders, say at the 4th or 5th order, which has been shown to give sufficiently accurate results for the short time as well as the longer time dynamics [131, 132]. In addition, we employ a rediagonalization step, by which the truncated band-diagonal representation in a reduced effective-mode space is re-transformed to a normal-mode like form. This approach has proven to be favorable numerically in conjunction with MCTDH calculations.

7.5 The Ising Model

In the previous sections, lattice models have been used for the generation of Hamiltonians for quantum dynamical simulations. In a complementary approach, the purpose of this chapter is the application of these lattice models for statistical modeling via the Kinetic Monte Carlo (KMC) methodology. Typically, an Ising Hamiltonian is used for creating model bulk heterojunction (BHJ) morphologies, which can then be used for subsequent propagation using classical-statistical techniques.

Originally, the Ising Hamiltonian has been developed to study ferromagnetism in solid phases, such as crystals [133]. Many years later, in a pioneering study performed by Watkins et al. [111], the same Hamiltonian was employed to create suitable model morphologies for subsequent use in a KMC algorithm. This set-up has been successfully applied to study a wide range of phenomena, ranging from exciton diffusion and dissociation [44, 134] to surface recombination [135] and even complete current-voltage curve modeling [136–138].

The original formulation of the Ising Hamiltonian, with nearest-neighbor spin interactions, is given as follows,

$$\hat{H} = -\frac{1}{2}\sum_{ij} J_{ij} s_i^z s_j^z \tag{7.14}$$

with the sum over all spins i and j of the system. J_{ij} is the interaction between the spins and s_i^z the z-component of spin i. As reported in reference [111], this methodology can also be applied to general molecular systems involving interacting sites; the mapping to the Ising Hamiltonian is appropriate when a coarse graining approach of the individual sites is carried out, as in the generation of suitable morphologies for KMC simulations. As originally proposed by Watkins et al., one calculates the energy of a two adjacent sites with opposite charge character, i.e., donor and accceptor, with the Hamiltonian shown in equation 7.14. The energy difference $\Delta\epsilon$ then determines the probability of a swapping event, i.e.

$$P(\Delta\epsilon) = \frac{exp[-\Delta\epsilon/kt]}{1 + exp[-\Delta\epsilon/kt]} \tag{7.15}$$

However, this method of calculation is not straightforward to apply in practice [111]. Therefore, an alternative but mathematically equivalent description developed by Heiber et al. [139] has been used in this thesis. The idea behind this approach is that the change in energy is thought of as breaking "bonds" in the initial state and the formation of new "bonds" in the final state. Then, the change in energy is calculated as the difference between the total energy of the initial bonds and the final bonds, i.e.

$$\Delta\epsilon = -\Delta N_1 J - \Delta N_2 \frac{J}{\sqrt{2}} \tag{7.16}$$

where J is the interaction energy and ΔN_i is the change in nearest neighbor bonds and next-nearest neighbor bonds, respectively. Once the change in energy is known, the probability of a swap in site character, i.e. swapping a donor site and an acceptor site or vice versa, according to equation 7.15 is calculated. Finally, a random number generator is used to determine if a change in site character is performed or not. This scheme is then repeated until a desired morphology has been created. By choosing the sign of the interaction energy J one can choose between a phase aggregated or phase separated morphology, as shown in chapter 12.

Part II

High Dimensional Quantum Dynamical Simulations

8 — Charge Separation in a Liquid Crystalline Donor-Acceptor Material

The first project presented addresses studies on a liquid crystalline donor-acceptor (DA) material, employing state-of-the-art electronic structure and high level quantum dynamical methods. The theoretical studies on this system are motivated by experimental work by the groups of S. Méry and S. Haacke at Strasbourg University, with whom our group has shared a joint DFG/ANR project on "Molecular Level Approaches to Photosensitive Naonstructured Materials".

In particular, in an experimental paper published by Roland et al. [140, 141], the group of S. Haacke reports on a charge transfer on a sub-100 femtosecond time scale in a novel DA system for organic solar cells. The study of the syste focuses on ultrafast transient UV/VIS absorption spectroscopy for the isolated DA system in solution and for the system arranged into a smectic liquid crystalline (LC) phase. For these cases, very different dynamical behaviours are observed. Whereas the system in solution exhibits an ultrafast excitation energy transfer (EET) (160 fs time scale) followed by a slower charge separation (2.5 ps time scale), quite the opposite is observed for the system in a LC phase. For the self-assembled system in a smectic LC phase, an immediate charge separation without a preceding EET step is observed. The timescale for the formation of the charge separated state is below 100 fs. The purpose of our theoretical study is to explain these findings.

Table 8.1 shows the characteristic time scales obtained from time-resolved ultrafast spectroscopic investigations. Even though the LC system looks promising at first sight, due to the ultrafast charge separation step, this system also shows a very high recom-

Table 8.1: Characteristic timescales from time resolved experiments. Taken from reference [141].

	EET	CT	Recombination
Solution	130 fs	2.7 ps	55 ps
LC	-	60 fs	70 ps

bination rate, which will limit its practical use as a component for photovoltaic devices. While the spectroscopic studies provide an insight into the dynamics of the system upon photoexcitation, the origin of the high recombination rate was unclear at the time of interpreting the experiments. Since standard spectroscopic methods lack spatial resolution, a molecular picture of the recombination process could not be provided.

Theoretical models, on the other hand, do provide the required spatial resolution since the resolution mainly depends on the choice of the model system. The model system should be capable of capturing the ultrafast character of the EET and charge separation and provide an insight into a possible mechanism of the recombination process. Therefore, a site-based model system has been set up in line with the electron-hole Hamiltonian described in section 7.1. Dynamical studies were carried out with the ML-MCTDH method.

8.1 Model System and Model Hamiltonian

The model system for the theoretical investigations is based on the preliminary electron diffraction and molecular modeling techniques presented in reference [142]. There, the molecular structure of the LC phase has been studied and evidence is provided for a unique, strongly tilted structure in the LC phase. Steady-state spectroscopic studies suggest that the donor species is assembled in a J-aggregate, leading to the observed red shift.

To understand the dynamics of the LC phase, representative fragments from the LC phase structure have been taken, for which high-level electronic structure calculations have been performed. This fragment-based information is used to parametrise a suitable model Hamiltonian for a quantum dynamical treatment. The fragment-based approach is supported by the steady state spectra which reveal that the spectrum of the isolated DA System is the sum of the individual spectra of an isolated D and an isolated A. Hence,

several fragments from the LC structure were taken, in particular representing nearest-neighbor aligned DA dimers and stacked DA dimers, for which electronic structure studies were performed. Dynamical calculations were subsequently carried out for a much larger assembly, as shown in figure 8.1.

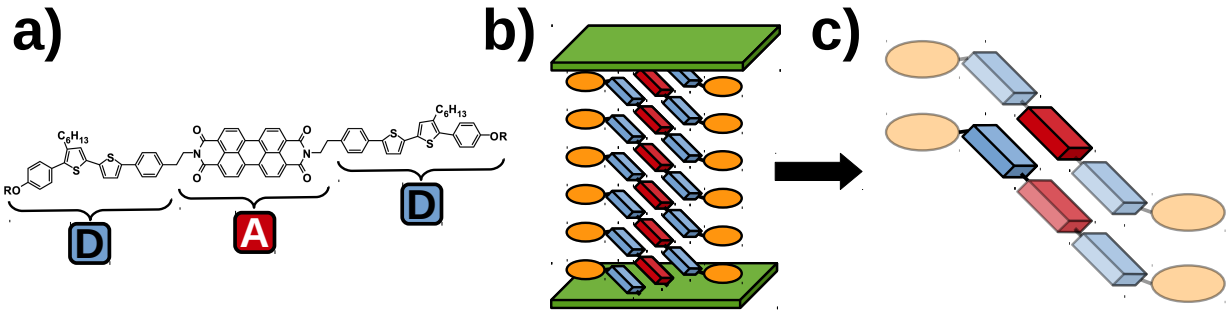

Figure 8.1: a) Molecular structure of the DAD triad with highlighted D and A moieties. b) Sketch of the DAD triad arranged in a smectic LC phase, where siloxane chains act as a scaffold. c) Stacked DAD triads. The transparent shading indicated that these molecules have been omitted from the electronic structure calculations to save computational time.

Figure 8.1a shows the molecular structure of a DAD triad. The donor part consists of a bis-thiophene derivative, whereas the acceptor consists of a perylene diimide moiety. Various experiments and theoretical studies on bis-thiophene and perylene diimide molecules suggest that these materials are suitable precursors for the construction of efficient solar cell devices [143–145]. Figure 8.1b shows a sketch of the DAD system upon self-organisation in a smectic LC phase. The pronounced tilt angle induced due to the self-organisation leads to an increased inter-layer overlap between stacked D and A units. Figure 8.1c shows a representative fragment which has been taken from the molecular assembly. The highlighted blue and red parts (representing donor and acceptor, respectively) show that dominant inter-chain interactions can occur in the smectic LC phase.

As has been pointed out in the introductory part of this chapter, a suitable model system and model Hamiltonian has to be capable to capture the mechanism leading to the ultrafast charge separation in the LC phase. Since on such short time scales coherent effects might play an important role, it is mandatory to use quantum dynamical methods.

The model Hamiltonian has been set up in a generalised electron-hole (e-h) representation in a single excitation subspace, in line with the general approach delineated in chapter

7. Furthermore, the model Hamiltonian will be restricted to a DA dimer as a fundamental building block, rather than a DAD trimer, in order to reduce computational costs. This is justified by the separable nature of the individual contributions of the monomers to the excited states, as can seen both from our calculations and from the experiments.

In the following, a basis is constructed such that the electron is located on site ν while the hole is located on site μ. Localised electron-hole pairs (i.e. electron and hole on the same fragment) correspond to an locally excited configuration (XT) on either the D or A moiety, e.g. $|D_i^{XT}\rangle = |\nu = i, \mu = i\rangle$. Conversely, if electron and hole are located on different monomers, these configurations correspond to a charge separated (CS) state, i.e. $|D_i^+ A_j^-\rangle = |\mu = i, \nu = j\rangle$. In the following, different CS states will be characterised by their electron-hole distance in monomer units. In this notation, CS(n) describes an electron-hole separation over $n \equiv i - j$ monomer units. For the dynamical treatment of a representative fragment of the LC phase, a model employing 12 DA pairs has been used. This gives rise to 168 electronic states, i.e. 12 $|D^{XT}\rangle$, 12 $|A^{XT}\rangle$ and 144 CS states.

In the basis specified above, the Hamiltonian of the system takes the following form,

$$\begin{aligned} \hat{H} &= \hat{H}_{el} + \hat{H}_{el-ph} \\ &= \underbrace{\hat{H}_{on-site} + \hat{H}_{coupl}^{intra} + \hat{H}_{coupl}^{inter}}_{\hat{H}_{el}} + \hat{H}_{el-ph} \end{aligned} \tag{8.1}$$

Here, the term $\hat{H}_{el}$ includes all the electronic interactions such as on-site energies and inter/intra-molecular diabatic couplings. The last term in equation 8.1 represents the linear coupling of the phonon modes to the electronic subset.

$$\hat{H}_{on-site} = \epsilon_D \sum_{i=1}^{N_D} |D_i^{XT}\rangle\langle D_i^{XT}| + \epsilon_A \sum_{i=1}^{N_A} |A_i^{XT}\rangle\langle A_i^{XT}| + \sum_{i=1}^{N_D}\sum_{j=1}^{N_A} \epsilon_{D_i^+ A_j^-} |D_i^+ A_j^-\rangle\langle D_i^+ A_j^-| \tag{8.2}$$

The on-site Hamiltonian contains the on-site energies for the different states, which are supposed to be equal for all fragments in a diabatic representation. The energies for the CS states are defined by the intrinsic Coulomb attraction between an electron and a hole,

resulting in an effective Coulomb barrier. The latter is here constructed from TDDFT calculations (see below). Next, the electronic couplings of the Hamiltonian look as follows

$$\begin{aligned}\hat{H}^{intra}_{coupl} = J^{\text{intra}}_{DA} \sum_{i=1}^{N_D}\sum_{j=1}^{N_A}(|D_i^{XT}\rangle\langle A_j^{XT}|\delta_{ij} + \text{h.c.}) \\ + \kappa^{\text{intra}}_{D} \sum_{i=1}^{N_D}(|D_i^{XT}\rangle\langle D_i^{+}A_i^{-}| + \text{h.c.}) + \kappa^{\text{intra}}_{A} \sum_{i=1}^{N_A}(|A_i^{XT}\rangle\langle D_i^{+}A_i^{-}| + \text{h.c.})\end{aligned} \tag{8.3}$$

and

$$\begin{aligned}\hat{H}^{inter}_{coupl} = J_D \sum_{i=1}^{N_D-1}(|D_i^{XT}\rangle\langle D_{i+1}^{XT}| + \text{h.c.}) + J_A \sum_{i=1}^{N_A-1}(|A_i^{XT}\rangle\langle A_{i+1}^{XT}| + \text{h.c.}) \\ + J^{\text{inter}}_{DA} \sum_{i=2}^{N_D}(|D_i^{XT}\rangle\langle A_{i-1}^{XT}| + \text{h.c.}) \\ + \kappa^{\text{inter}}_{D} \sum_{i=1}^{N_D}(|D_i^{XT}\rangle\langle D_i^{+}A_{i-1}^{-}| + \text{h.c.}) + \kappa^{\text{inter}}_{A} \sum_{i=1}^{N_A}(|A_i^{XT}\rangle\langle D_{i+1}^{+}A_i^{-}| + \text{h.c.}) \\ + t_e \sum_{i=1}^{N_D}\sum_{j=2}^{N_A-1}(|D_i^{+}A_j^{-}\rangle\langle D_i^{+}A_{j\pm1}^{-}| + \text{h.c.}) + t_h \sum_{i=2}^{N_D-1}\sum_{j=1}^{N_A}(|D_i^{+}A_j^{-}\rangle\langle D_{i\pm1}^{+}A_j^{-}| + \text{h.c.}).\end{aligned} \tag{8.4}$$

Equation 8.3 describes the excitonic coupling J_{DA} as well as the exciton to charge transfer couplings, κ_D and κ_A, in a DA chain between covalently bonded D and A moieties. In contrast, equation 8.4 describes the excitonic as well as exciton charge transfer couplings between different layers of DA chains, e.g. between the highlighted fragments in figure 8.1c. The last two terms in equation 8.4 describe the transfer integrals for electron and hole transport, respectively.

Finally, the electronic part of the Hamiltonian is modulated by the last term shown in equation 8.1, i.e., the vibronic coupling part of the Hamiltonian. This part describes how displacements in the nuclear geometry give rise to energetic fluctuations and hence, tune energy levels in and out of resonance. At the same time, such vibronic couplings can modulate the diabatic couplings. In the present study, the electron phonon coupling has been obtained from state-dependent potential energy surfaces (PES) for selected vibrational modes. The chosen PES have been identified by an analysis of the Franck-Condon gradients and represent high frequency bond length alternation (BLA) modes on the D and A fragments as well as a low-frequency torsional degrees of freedom located solely on

the D moiety [146]. Furthermore, an intermolecular mode specific to the LC phase has been taken into account, representing a mode modulating the distance between two layers of DA chains. Overall, the electron phonon (vibronic) coupling part of the Hamiltonian reads as follows,

$$\begin{aligned}\hat{H}_{el-ph} = &\hat{T}_{\mathrm{ph}}(\{\zeta^D\},\{\zeta^A\},\{\zeta^{DA}\}) \\ &+\sum_i \hat{V}_D^{XT}(\{\zeta_i^D\},\{\zeta_i^{DA}\})\,|D_i^{XT}\rangle\langle D_i^{XT}| + \sum_i \hat{V}_A^{XT}(\{\zeta_i^A\},\{\zeta_i^{DA}\})\,|A_i^{XT}\rangle\langle A_i^{XT}| \\ &+\sum_i\sum_j \hat{V}_{DA}(\{\zeta_i^D\},\{\zeta_j^A\},\{\zeta_{ij}^{DA}\})\,|D_i^+A_j^-\rangle\langle D_i^+A_j^-| \end{aligned} \tag{8.5}$$

The kinetic energy operator $\hat{T}_{\mathrm{ph}}$ is chosen to be electronically diagonal in order to fulfill the requirement of a diabatic Hamiltonian. The potential energy terms $\hat{V}$ represent the abovementioned selected PES cuts of the system. In the next section, we describe how these PES cuts were calculated explicitly in order to fit them to analytical funtions and implement them into a given model Hamiltonian for subsequent wave packet propagation.

8.2 Electronic Structure Calculations

According to the model Hamiltonian presented in the previous section, electronic structure calculations on representive fragments taken from the smectic LC phase have been carried out. The highlighted structure shown in figure 8.1c has been optimised using the ωB97XD DFT functional [147] along with the SVP basis set [148, 149] as implemented in the Gaussian09 [150] software package. Based on this optimised geometry, excited state calculations employing the ADC(2) method and def2-SVP basis set have been done, using the Turbomole program package [151].

As has been pointed out in chapter 5, the ADC(2) method is a high-level *ab initio* based Green's function method. This method is suitable as a benchmark tool to find a suitable DFT functional that represents the electronic structure of the system in an appropriate way. Whereas for an isolated chain of neighboring D-A units a suitable DFT functional could be found [146], this was not the case for the stacked alignment shown in figure 8.1c. Due to the stacked alignment of the molecules and the close proximity of the D and A moieties, DFT functionals with an inherent dispersion and long-range correction had to be used. This limits the choice of available DFT functionals to ωB97XD or CAM-B3LYP

[152]. Recently there has been a benchmark study on the performance of the ωB97XD for the excited states of thiophene molecules [153]. The results of that study have been compared to ADC(2) calculations and are fairly similar. Since the D moiety of the system under investigation is a thiophene derivative, the use of the ωB97XD functional is well justified. However, while the obtained DFT ground state structure seems to be plausible, the excited states obtained from the ωB97XD functional were not always in agreement with the energetics found from our ADC(2) calculations. Therefore, the energetics defined in our model Hamiltonian refers throughout to the ADC(2) results.

Figure 8.2 shows the molecular geometry of an optimised DA dimer, representing the highlighted area of figure 8.1c along with the excited states obtained with the ADC(2)/def2-SVP method.

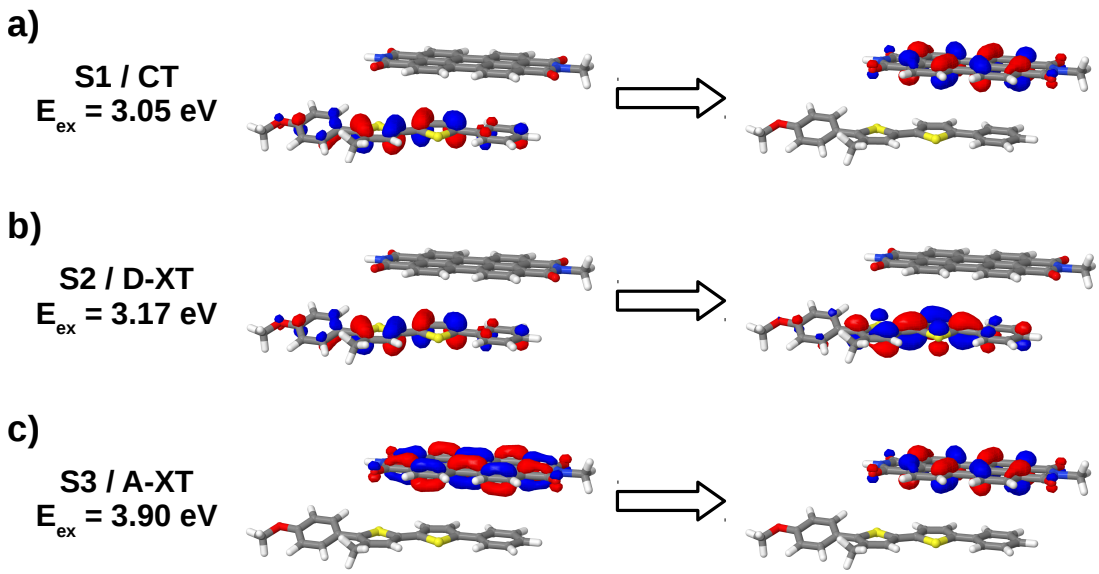

Figure 8.2: Excitations calculated with the ADC(2) method and the def2-SVP basis set. Shown are the natural transition orbitals as provided by the TheoDORE program package [154–156].

Figure 8.2a-c shows the three relevant excited states which have been identified from the ADC(2)/def2-SVP calculations and a natural transition orbital (NTO) analysis [157]. Figure 8.2a shows the first excited state. From the NTO analysis one can deduce that this state corresponds to the charge transfer (CT) state. The second excited state corresponds to the locally excited D-XT state, i.e. the experimentally prepared initial state. One can

see that the energy gap between the bright excited D-XT state and the CT state is only 0.12 eV. On the other hand, the S3 state (figure 8.2c) is clearly the excited A-XT state, lying 0.73 eV above the bright D-XT state.

The diabatic coupling, mediating the transfer from one state to another, have been obtained by a diabatisation procedure as explained in section 4.3 and references [158, 159]. Briefly, a projection of the adiabatic wave function $|\Psi\rangle$ onto reference wave functions with defined character, i.e., of locally excited or charge transfer type, is carried out. Then, the diabatic wave functions $|\Phi\rangle$ are expressed as a linear combination of the adiabatic wave functions, i.e. the adiabatic wave functions act as basis for the diabatic wave functions. Finally, the matrix element $\langle\Phi_i|\hat{H}|\Phi_j\rangle$ is calculated, which gives the value of the respective diabatic coupling. In the following table 8.2, the diabatic couplings and transfer integrals are shown, obtained from the diabatisation procedure outlined above.

Table 8.2: Electronic diabatic couplings, calculated with the LC-BLYP functional.

J_{DA}^{intra}	κ_D^{intra}	κ_A^{intra}	J_D	J_A	J_{DA}^{inter}	κ_D^{inter}	κ_A^{inter}	t_e	t_h
0.02	0.002	2×10^{-4}	-0.10	-0.03	0.059	0.025	0.023	5×10^{-4}	0.0013

From the table, one can see that the entries corresponding to the intra-molecular transfer, i.e. the Hamiltonian in equation 8.3, are much smaller then the couplings of the Hamiltonian in equation 8.4. The reason for that behaviour is due to the fact that the calculated diabatic couplings are proportional to the overlap of the corresponding wave functions. Since the overlap for an intermolecular transfer is much larger then for the intramolecular transfer, the diabatic couplings are also much larger.

The magnitude of the intramolecular couplings from table 8.2 are also in accordance with the experimental results for the system in solution, see also table 8.1. Here, first an EET step from the D-XT to the A-XT state happens, followed by slower CT state formation. This is reflected by the diabatic couplings, where the coupling between the D-XT and A-XT states is one order of magnitude larger then the coupling between the A-XT and CT state. The coupling between the D-XT and CT state is zero. For the smectic LC phase, this behaviour is the opposite. Here, the experiment suggests that the CT state formation happens immediately after photoexcitation to the bright D-XT state. In combination with the excitation energies shown in figure 8.2, this behaviour is supported by the large D-XT

to CT couplings. Even though the coupling for an EET process is twice as high as for the CT state formation, this process does not happen due to the energetics. From figure 8.2 one can see that the A-XT state, i.e. the final state of the EET process originating from the D-XT state, is energetically out of reach.

After the initial CT state has been formed, the subsequent spatial separation of electron and hole obeys Coulombs law. To incorporate the energetics of the spatially separated electron-hole states, the Coulomb barrier has been calculated explicitly. To do so, various D-A conformations have been taken from the smectic LC phase, each mimicking a distinct electron-hole configuration. Donor and acceptor fragments not participating in the calculation of the Coulomb barrier have been replaced by point charges, modeling the distribution of local dipole moments. Furthermore, an external electric field of 50 $V/\mu m$ has been included in the calculation in order to enhance charge separation.

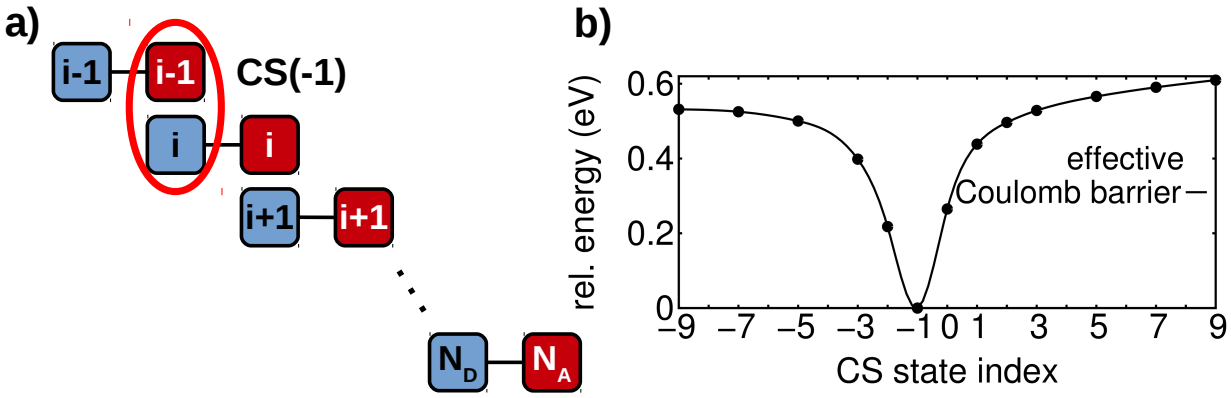

Figure 8.3: a) Schematic representation of a LC DA stack consisting of N_D donor moleucles and N_A acceptor molecules. The highlighted CS(-1) configuration is the state to which the initial charge separation occurs, according to electronic structure calculations. b) Calculated Coulomb barrier. The barrier has been obtained with the ωB97XD functional and the SVP basis set, as implemented in the Gaussian09 software package.

Figure 8.3 shows (a) a sketch of the calculation set up as well as (b) the resulting Coulomb barrier. As mentioned above, monomers not participating in the calculation of a specific electron-hole distance for the Coulomb barrier have been replaced by point charges, representing the dipole moment between two fragments. (We note, though, that polarization effects are not correctly represented at this level of treatment.) Translating this explicitly to the highlighted CS(-1) configuration in figure 8.3, the donor fragments

$i-1$ & $i+1$ as well as the acceptor fragments i & $i-2$ (not shown) would be replaced by point charges. This calculation set up has been used to calculate the Coulomb barrier for up to a electron-hole distance of ±9 DA units. Figure 8.3 shows the resulting barrier with an applied external electric field of 50 $V/\mu m$. One can see that the CS(-1) state (see figure 8.3a) is strongly stabilised and acts as a local trap. The other CS states are much higher in energy and one can expect that these states get barely populated, even though the D-XT state lies roughly 0.1 eV above the CS(-1) state. The reason for the high barrier between the CS(-1) state and the CS(0) or CS(-2) state is the negligible overlap between donor/donor and acceptor/acceptor molecules. Due to the unique alignment of the covalently bonded D-A units within the smectic LC phase, the overlap between different layers of D-A molecules is very small and hence, a lot of energy is needed to promote an electron (hole) from one acceptor (donor) to the other.

Once the energetics of the system have been defined, the potential energy surfaces (PES) have to be calculated. From the analysis of the Franck-Condon gradients, several important modes were identified, for which PES cuts were calculated.

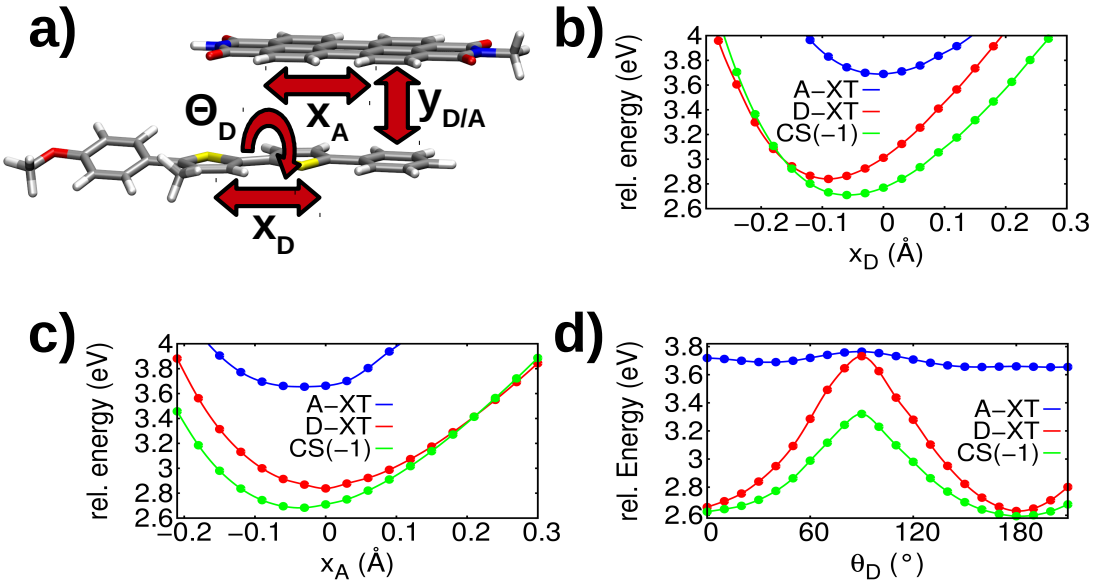

Figure 8.4: a) Molecular representation of a DA dimer, taken from the LC structure. Additionally shown are the degrees of freedom for which the PES are calculated. b) PES for the x_D mode. c) PES for the x_A mode. d) PES for the θ_D mode. Green curves correspond to the CS(-1) state, red to the D-XT and blue to the A-XT state.

Figure 8.4a shows a DA fragment from the smectic LC phase with the most relevant degrees of freedom (DOF). Figure 8.4b shows the PES for the high frequency BLA mode located between the two thiophene rings on the donor fragment. Upon photoexcitation from the ground state (not shown) to the bright D-XT State, the bond length shortens. Furthermore, one can see that the PES of the D-XT and the CS(-1) state intersect each other, highlighting the importance of the BLA mode for the dynamics. Due to a sufficient amount of excess energy, the wave packet should be able to reach the intersection between the two states. The BLA on the acceptor does not play such a central role. A crossing between the D-XT and CS(-1) does exist, but is higher in energy then the crossing in the BLA located on the donor. Nevertheless, the BLA on the acceptor does play a role in the dynamics since it modulates the electronic energy levels due to the linear vibronic coupling ansatz. The same observation can be made for the torsional DOF as for the BLA on the acceptor. Even though no crossing exists, the torsional DOF plays in important role in generating a continuum of vibronically resolved states. Furthermore, it was shown in literature that the combination of high frequency modes and low frequency modes is crucial for the transfer pathways, even though there may not be directly observable intersections in the selected PES cuts [126]. For all three PESs, one can see that the A-XT state lies well above the D-XT and CS(-1) state. Hence, the A-XT state does not play a role in the dynamics of the smectic LC phase, which was already confirmed by the time resolved spectroscopic experiments.

The PESs in figure 8.4b-d have been calculated at a discrete set of geometries. In order to implement a continouus PES into the proposed model Hamiltonian, these discretised points have to be fitted by appropriate analytical functions. For the BLA and intermolecular modes, a Morse potential function has been used, whereas a cosine series has been employed for the torsional DOF. Specifically, the analytical expressions look as follows

$$v(x) = D_0 \left(1 - exp(-\alpha(x - x_0))\right)^2 \tag{8.6}$$

and

$$v(\theta) = a_1 cos(\theta) + a_2 cos(2\theta) + a_3 cos(4\theta) \tag{8.7}$$

From these analytical expressions, the following parameters have been obtained.

Table 8.3: Parameters obtained from a fit to the calculated PES, as shown in figure 8.4b-d.

		GS	ES	CT
x_D	D_0	0.2210	0.2425	0.2514
	α	0.9095	0.9804	0.9235
	x_0	-0.0103	-0.1453	-0.0886
x_A	D_0	0.2210	0.2337	0.2418
	α	0.8905	0.9225	0.8833
	x_0	-0.0097	-0.0870	-0.0635
θ_D	a_1	5.83E-4	5.24E-4	4.92E-4
	a_2	-1.4E-3	-0.0185	-0.0118
	a_3	7.66E-4	2.80E-3	2.50E-3
$y_{D/A}$	D_0	0.0086	0.0165	0.0317
	α	0.668	1.037	0.733
	x_0	7.18	7.18	6.23

It should be noted that the electronic structure calculations performed to parametrise the intermolecular mode $y_{D/A}$ did not yield a bond length reduction between the donor and acceptor moiety upon CS(-1) state formation. Therefore, the potential minimum has been shifted artificially by 0.5 $\mathring{A}$ due to the Coulomb attraction between opposite charges.

8.3 Quantum Dynamics Simulations

Once the elements of the Hamiltonian proposed in equation 8.1 to 8.5 have been defined, high-dimensional quantum dynamics simulations can becarried out. Prior to that, it is beneficial to analyse the spectrum of the Hamiltonian, i.e. the eigenvaluesand eigenvectors after photoexcitation to the bright D-XT state. Since the A-XT states are energetically and dynamically irrelevant for the formation of the charge transfer state, they will be neglected in the following. This will reduce the total number of states of the model Hamiltonian from 168 to 156, i.e. 12 D-XT and 144 CS(n) states, where the CS states' energies are defined by the Coulomb barrier shown in figure 8.3b. Figure 8.5a shows the diabatic (I) as well as local-adiabatic (II) eigenvalues of the Hamiltonian. The diabatic eigenvalues correspond to the on-site energies ϵ_D and $\epsilon_{D_i^+ A_j^-}$ from equation 8.1. Here one can see that the only

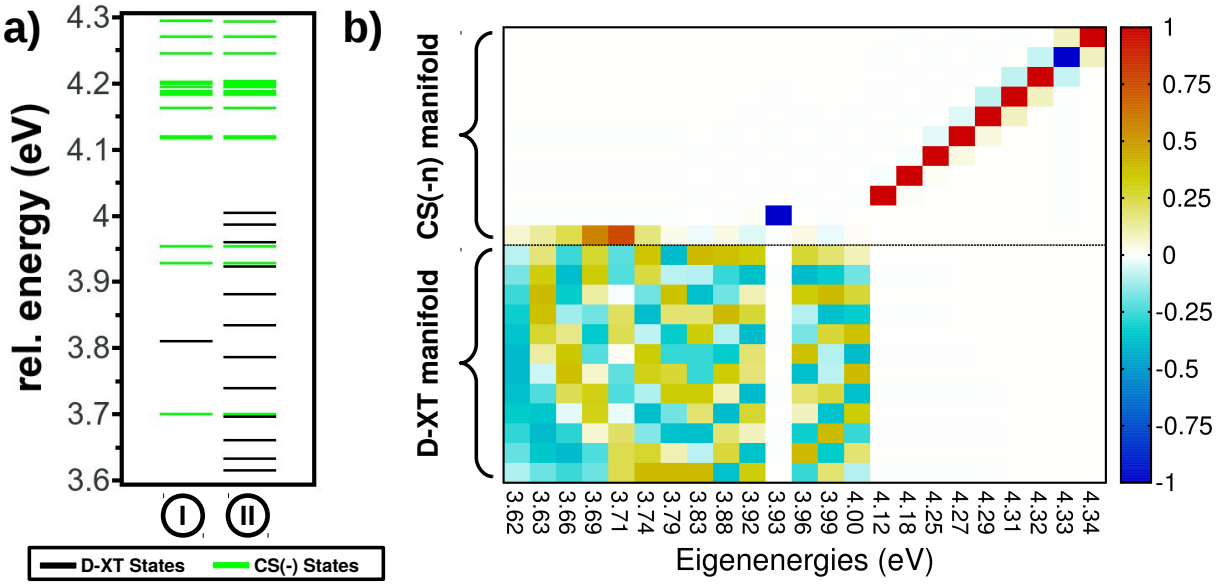

Figure 8.5: a) Diabatic (I) and adiabatic (II) eigenvalues of the electronic Hamiltonian after numerical diagonalisation. b) Graphical representation of the eigenvectors of the electronic Hamiltonian after diagonalisation, illustrating the mixing between the D-XT and CS(-n) manifold. Entries below the dashed line correspond to wave function coefficients for the D-XT state, whereas entries above the dashed line correspond to wave function coefficients for the CS(-n) state.

energetically favourable CS state is the one below the D-XT on-site energy, which corresponds to the CS(-1) state. In the local-adiabatic representation, the coupling between the D-XT manifold and the CS manifold has been neglected. One can see that the influence of the transfer integrals on the CS(n) states is negligible, which is not surprising due to their small magnitude. The D-XT manifold shows a splitting into 12 adiabatic eigenvalues. Due to the sign of the excitonic coupling shown in table 8.2 one can see that the bright state is the energetically lowest state.

From the graphical representation of the eigenvectors in figure 8.5b one can see that the bright D-XT state on the lower band edge of the D-XT manifold shows a non-negligible CS(-1) state mixing. This mixing intensifies until the fifth state, afterwards the CS(-1) contribution to the D-XT state gets lower again. Due to the linear vibronic coupling approach, dynamical changes in the nuclear geometries will induce fluctuations in the energy levels and hence, open or close specific pathways of exciton migration or dissociation. From the analysis presented above, one can deduce that the CS(-1) state will be energetically

accessible, while the remaining CS(n) states may not be accessible immediately. A full quantum dynamical treatment of the proposed model Hamiltonian is therefore necessary in order to obtain insight into the mechanism after photoexcitation.

The full quantum dynamics have been done using the ML-MCTDH method with 156 electronic states (12 D-XT & 144 CS states) and 48 DOF. In addition to the 47 DOF from the system (i.e. 12 x_D, 12 θ_D, 12 x_A & 11 $y_{D/A}$), an additional effective mode has been constructed to account for the missing reorganisation energy due to the reduced amount of DOFs of the system. Furthermore, simulations involving the isolated DA system in solution have been performed, employing the MCTDH method in multi-set formalism. Here, the three experimentally observed states (i.e. excitonic D, excitonic A and CT state) along with three DOF and an additional solvent coordinate to account for the influence of the solvent on the dynamics, have been used. Details regarding the electronic structure of the isolated DA system can be found in reference [146]. Figure 8.6a shows the population of

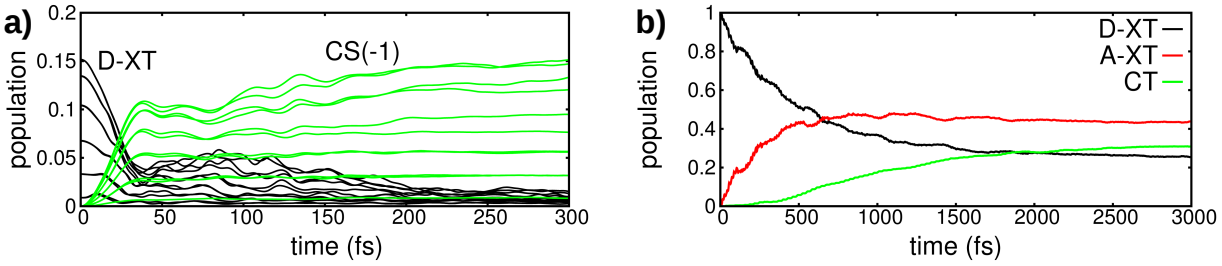

Figure 8.6: a) Individual excitonic donor and CS(-1) populations for the simulation of the smectic LC phase. The initial excitonic state is a delocalised J-aggregate. b) Dynamics of the isolated DA system in solution. In line with the experiment, first an EET followed by a slower build up of the CT state can be observed.

the invidiual D-XT states and the CS(-1) states. Electronic structure calculations and the red-shifted steady-state absorption spectrum indicate a J-aggregate type delocalisation of the initial wave packet over several units [141]. Therefore, the initial wave packet is taken to be delocalised over all 12 accessible donor molecules present in the model Hamiltonian. From the population plot, one can infer that an ultrafast exciton dissociation into charge separated states is occurring. This is also in accordance with the reported experimental results, see also table 8.1. Interestingly, the quantum dynamics reveal two time scales of the population transfer: one ultrafast time scale in the $\approx$ 60 fs regime and one slower time scale in the 200 fs regime. The slower time scale can be attributed to the build-up and decay of a quasi-stationary coherent superposition between the initial D-XT and the

resulting CS(-1) states. Figure 8.6b shows the population dynamics for the isolated system in solution. Again, the experimentally bright D-XT state has been prepared as the initial state for the wave packet dynamics. One can see that first, an EET from the D-XT to the A-XT state is occurring, followed by a slower CT state formation. Again, this is in agreement with the experimental results reported in table 8.1.

As has already been pointed out, the population dynamics of the smectic LC phase simulations in figure 8.6a reveal two time scales, with the slower one originating from a coherent superposition state between the D-XT and CS(-1) state manifold. Figure 8.7a

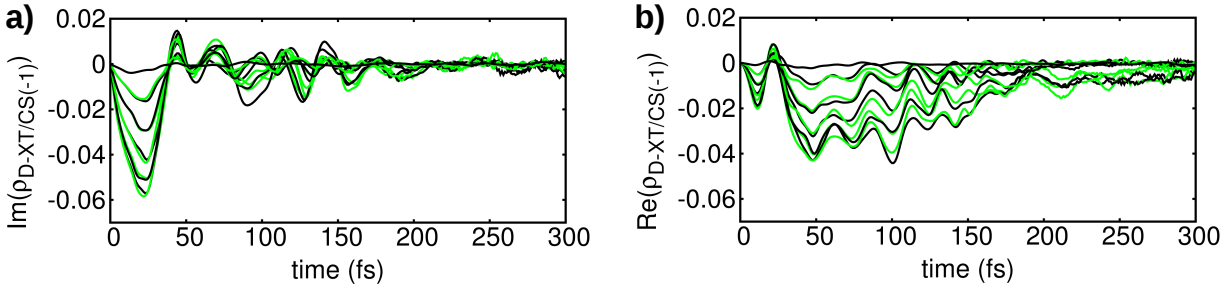

Figure 8.7: a) Imaginary part of the electronic coherence $\rho_{D-XT/CS(-1)}$. b) Real part of the electronic coherence $\rho_{D-XT/CS(-1)}$. The imaginary part of the electronic coherence determines the transient population flux, which can be seen in the population dynamics in figure 8.6. The real part shows that a long-lived coherent superposition between the D-XT and CS(-1) state emerges, which is responsible for the two-timescale dynamics in the population plot.

shows the imaginary part of the electronic coherence, i.e. $\rho_{i,i-1}^{D^{XT}-CS(-1)} = \langle D_i^{XT}|\hat{\rho}|D_i^+ A_{i-1}^-\rangle$ with $\hat{\rho} = |\psi\rangle\langle\psi|$. The imaginary part of the electronic coherence determines the fast $\approx$ 50 fs population flux [160] from the D-XT to the CS(-1) state, as it can be seen in figure 8.6a. The real part of the coherence suggests that a coherent superposition state is formed, which lasts for about 200 fs until it disappears again.

So far the ultra fast mechanism leading to the initial charge seperation could be elucidated. Yet, the analysis lacks an explanation of the high recombination rate, which has been reported experimentally. Therefore, the spatial extension of the electron-hole separation has been analysed. Since the proposed model system and model Hamiltonian has all electron-hole interactions included, it should give some evidence about the high recombination rate. Figure 8.8 shows the CS(n) state populations along with the cumulative population of the individual D-XT states, i.e. $P_D^{XT} = \sum_i P_{D_i}^{XT}$. It is obvious that all pop-

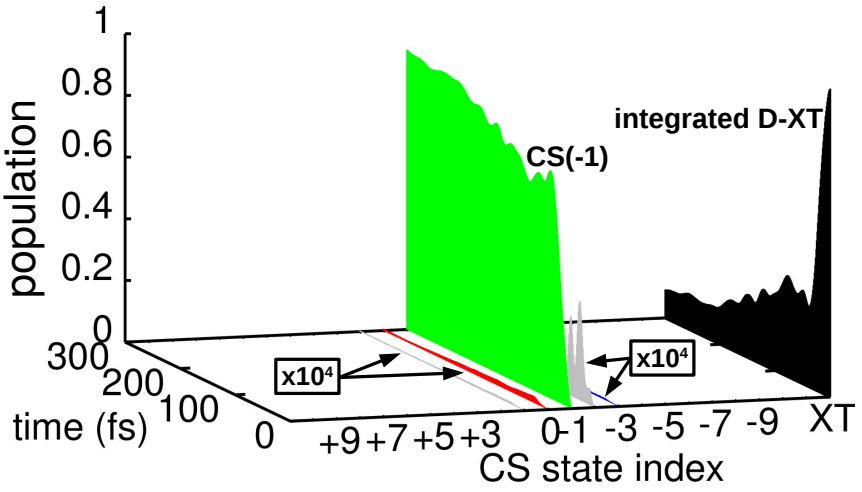

Figure 8.8: Spatially resolved populations of the different CS states. The ultrafast excitonic decay of the integrated D-XT populations matches the rise of the initial CS(-1) state. The other CS($\pm n$) states are barely populated due to the high Coulomb barrier and small transfer integrals.

ulation accumulates in the CS(n=−1) state, with the population of the other CS(n≠ −1) is nearly zero. One of the reasons for this behaviour is the huge Coulomb barrier between the individual CS(n) states, limiting the transfer efficiency. Another important point is the small value of the transfer integrals. From table 8.2 one can see that the electron (t_e) and hole (t_h) transfer integrals are of the order of 10^{-3}. In combination with the high Coulomb barrier, a transfer along the molecular axis is not possible and these two effects contribute as major factors to the high recombination rate. Since electrons and holes remain spatially close to each other, they are more likely to undergo recombination rather than efficient charge separation.

In addition to the fully delocalised initial condition prepared in the bright D-XT J-aggregate state, various degrees of delocalisation have also been used as an initial state. From figure 8.5b it is obvious that the fully delocalised initial state is the lowest eigenstate in an adiabatic representation due to the nodeless structure of the wave function. Therefore, localisation should increase the initially available excess energy and maybe facilitate new pathways. The following figure shows the results for the quantum wave packet dynamics with various degrees of delocalisation. Figure 8.9a shows the overall CS state populations for various degrees of initial delocalisation. One can see that the amount of CS states generated does not deviate very much with increasing delocalisation. Except for a localised

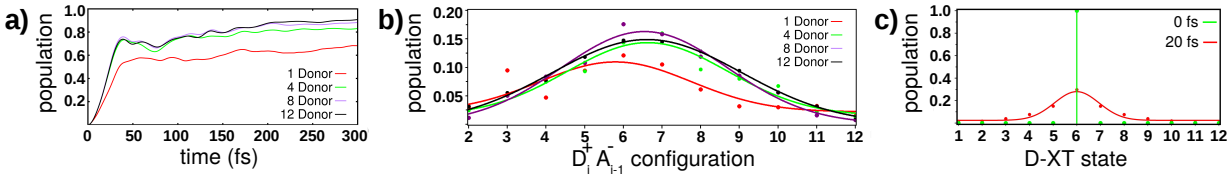

Figure 8.9: Influence of different initial delocalisation lengths on the overall CS state population. a) Overall CS state populations for different delocalised initial conditions. b) Distribution of the different CS(-1) states depending on the initial delocalisation length. c) D-XT state populations at 0 femtoseconds and after 20 femtoseconds starting from a localised initial condition to highlight the very fast excitonic delocalisation.

initial condition, the integrated CS state populations are fairely even. Figure 8.9b shows the distribution of the accessible CS(-1) states depending on the initial condition. Again, the same behaviour can be seen as for figure 8.9a, where the different delocalisation lengths do not change anything in the dynamics. In conjunction with the CS state populations from figure 8.9a this leads to the conclusion of an efficient and fast exciton delocalisaton over the whole lattice. Figure 8.9c emphasizes this behaviour. One can see that the initial localised excitation spreads equally over the whole lattice after already 20 femtoseconds, indicating a fast and efficient exciton delocalisation. After the exciton delocalisation, the CS(-1) states are populated.

8.4 Summary and Conclusion

High-level electronic structure calculations as well as state-of-the-art quantum dynamics simulations based on a first-principles parametrised model Hamiltonian have been conducted to elucidate the ultrafast mechanism of exciton dissociation leading to the generation of charge separated states in a liquid-crystalline donor-acceptor co-oligomer combination. The proposed model system and the model Hamiltonian are based on a generalised linear vibronic coupling approach in combination with the knowledge of experimental observations. Electronic structure calculations were performed for suitable fragments taken from the smectic LC phase. These calculations reveal that an ultrafast exciton dissociation into free charge carriers should be possible due to the small energy gap between the bright excitonic donor state and the charge transfer state. Furthermore, the electronic structure calculations revealed that the excitonic acceptor state, responsible for the EET as seen in the isolated system in solution, is energetically out of reach and hence, EET does not play a role in the dynamical treatment of the system. The calculated diabatic couplings

emphasize the possibility of an ultrafast exciton dissociation, indicated by a reasonably large coupling value.

A population analysis of the quantum dynamics simulations showed that the exciton dissociation is occurring on an ultrafast time scale, namely within the first 50 femtoseconds. Furthermore, the population analysis indicated a second time scale, which is of the order of 200 femtoseconds. This second time scale could be interpreted as the build-up and decay of a quasi-stationary coherent superposition of the initial excitonic donor state with the charge separated state. Further analysis of the charge separated state populations revealed that the spatial extension of the electron-hole distance remains on the order of one monomer unit. This is not very surprising if one recalls the high Coulomb barrier and the small transfer integrals. Ultimately, this spatial localisation of electrons and holes will lead to recombination processes on longer time scales, contrary to the desired charge separation into free charge carriers. Upon exciton localisation, this behavior does not change, even though the initial wave packet now possesses more excess energy. Due to very fast and efficient exciton delocalisation, the charge separation process happens after exciton delocalisation.

Summarizing the combined electronic structure and quantum dynamics simulations, it can be stated that the molecular packing plays a central role in the energetics of the system and the subsequent dynamics upon exciton dissociation. Even if exciton dissociation might be the kinetically fastest process, this will not lead to an efficient generation of free charge carriers. Interestingly, this behaviour was also observed for other donor-acceptor systems composed of oligo(p-phenylenevinylene) and perylene diimides [161, 162]. A detailed understanding of the influence of molecular packing on the photophysical properties is needed for the efficient design of more efficient organic photovoltaic devices in the future.

8.5 Outlook to 2nd Generation DA Systems

In view of the inefficient charge generation in the first-generation DAD system, a second generation of D_nA dyad co-oligomers was devised [35, 36] with the aim of increasing the CT lifetime while preserving a near 100% CT formation efficiency. An increased CT lifetime is indicative of a reduced recombination rate and a higher photocurrent yield. This new co-oligomer generation features both chemical modifications and a different molecular packing

as compared with the first-generation material. As detailed in references [35, 36, 163], the second-generation material is organized into highly ordered lamellar mesophases that feature well-defined donor and acceptor domains; the latter are interleaved such as to form a zipper-like structure [36, 163].

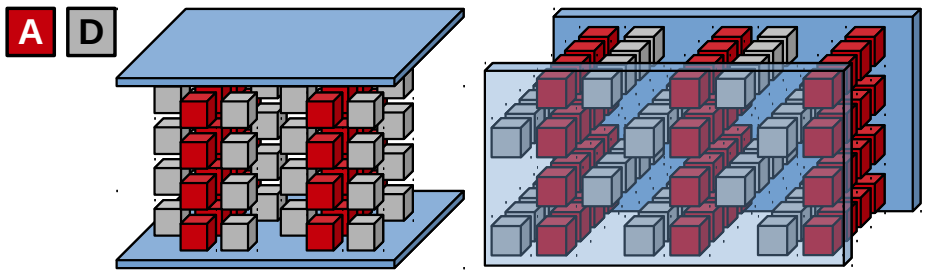

Figure 8.10: Sketch of 2nd generation DA materials arranged into a LC phase. One can see the different ordering patterns with planes consisting either of DA or AD dimers.

Figure 8.10 shows a sketch of the second generation DA system arranged into a mesoscopic phase. From both figures one can see that there is an alternating stacking pattern of AD in every even row and DA in every odd row. While the acceptors are in contact with each other via two dimensions, the donors are interacting only in one dimension with each other. The dimension in which both D and A are overlapping with the next DA dimer is caused by the strong π-π interaction of the acceptors.

As for the aspect of chemical design, the donor and acceptor cores are closely related to the first-generation material, but additional linking moieties are now sandwiched between the D and A parts, as illustrated in figure 8.2. Notably, the additional δ (benzene containing) and δ^+ (benzothiadiazol containing) variants are investigated. In addition, a δ^- (amino) moiety is optionally attached to the donor building blocks. Finally, several D units may be concatenated to form, e.g., $\delta^-\mathrm{D}_n\delta^+\mathrm{A}$ units, whose length tends to increase both the CT formation time and the CT lifetime [164].

Spectroscopic investigation reveals that in the presence of the δ spacer, the transfer mechanism remains similar to the first-generation material (see figure 8.11a and table 8.1), such that donor-acceptor excitation energy transfer precedes charge transfer. The main effect of the spacer is an increase of both EET and CT lifetimes. However, in the presence of the δ^+ spacer, the mechanism changes drastically (see figure 8.11b). Here, the EET step is now absent, and charge transfer occurs directly from the photoexcited donor ($\mathrm{D}\delta^+$) moiety, on a time scale of $\sim$90 ps. Further, the δ^- (amino) moiety leads to a significant

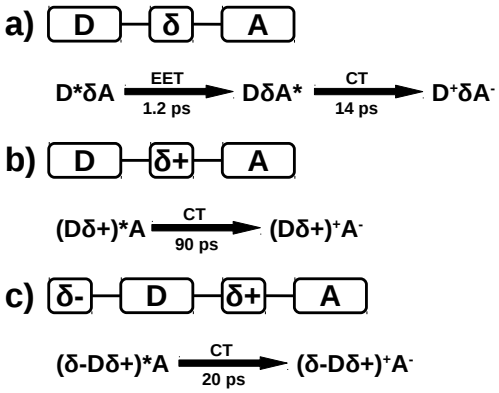

Figure 8.11: Schematic illustration of DδA, Dδ^+A and δ^-Dδ^+A species and the relevant EET and CT transfer steps from time-resolved spectroscopy [164]. The measured time scales refer to solution phase measurements with chloroform solvent.

(up to threefold) extension of the CT lifetime, see figure 8.11c.

The spectroscopic observations are backed up by electronic structure analysis (see figure 8.12), revealing an additional excitation on the δ^+ moiety (DS_1) in addition to the principal donor transition (DS_2). A more detailed analysis confirms that this transition is involved in the (Dδ^+)→A charge transfer [164].

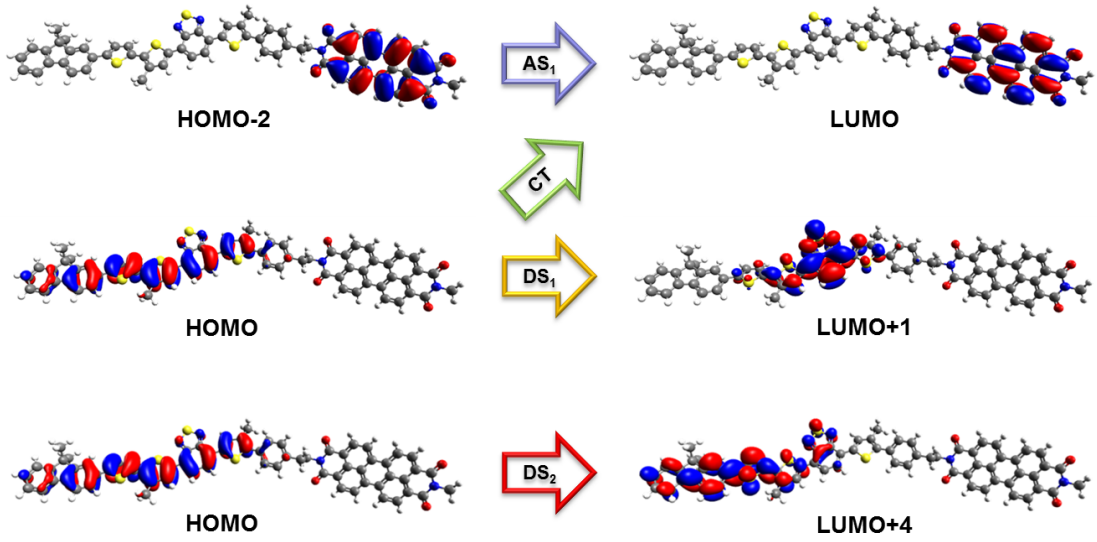

Figure 8.12: Excited state electronic structure of the Dδ^+A species, showing the most relevant electronic transitions. As compared with figure 8.2, note the additional excitation on the δ^+ moiety (DS_1) which is now involved in the D-A charge transfer.

An extensive analysis of the influence of the donor length n with respect to charge transfer formation and recombination times for both the $D_n\delta^+A$ and $\delta^-D_n\delta^+A$ has been done. As it was already seen from figure 8.11, the influence of the δ versus δ^+ spacer on the charge transfer formation time was quite dramatically, which is believed due to the absence of the excitation energy transfer. From table 8.4 one can see that the influence of the donor length D_n of the $D_n\delta^+A$ compound does not effect very much the charge transfer formation and recombination times. In contrast, the influence of the donor length for the $\delta^-D_n\delta^+A$ compound is much stronger. Especially for the charge transfer recombination kinetics, an increase of the charge transfer lifetimes from 400 ps to 2.3 ns could be observed. It is believed that the reason for this increase is due to the shielding effect of the δ^- group, which enhances the separation distance of electron and hole and thus, leading to a longer CT life time.

Table 8.4: Charge transfer formation and recombination times of 2nd generation DA systems. Various lengths of donors have been used for the corresponding measurements. All times in picoseconds.

	$D_n\delta^+A$		$\delta^-D_n\delta^+A$	
n	CT Formation	CT Recombination	CT Formation	CT Recombination
0	90	410	20	400
1	90	480	14	2300
2	150	440	14	1100
3	140	430	-	-

In order to explain the findings of the slow charge transfer formation and recombination times as compared to the first generation system (see also table 8.1), an analysis of the rates within the Marcus-Levich-Jortner formalism has been done. The results of the electronic couplings obtained from this analysis are shown in the following table.

From table 8.5 one can see that the electronic coupling values are in general very small and on a comparable order of magnitude as for the first generation system, see also table 8.2. In view of the future design of molecular functional materials and especially the experimentally observed increase in CT lifetimes, a reduction in the electronic coupling is desireable, which seems to lead to an increase in the charge transfer life time. This observation, where a decrease of the electronic couplings is accompanied by an increase in

Table 8.5: Electronic couplings for charge separation and charge recombination processes. Results have been obtained from measurements in chloroform. All values in meV.

Compound	Process	Coupling
$D_1\delta A$	Formation	2.39
	Recombination	0.54
$D_1\delta^+ A$	Formation	1.38
	Recombination	0.50
$\delta^- D_1\delta^+ A$	Formation	0.89
	Recombination	0.31

charge transfer lifetime, can be explained by the overlap between the relevant molecular orbitals. According to $V^2 = V_0^2 exp(-\beta R_{cc})$ [165] with V being the electronic coupling, it is proportional to the electron-hole distance and thus also the overlap of the relevant molecular orbitals. In conjunction with the observations made that electron push and pulling effects increase the charge transfer formation life time, one can deduce that the average electron-hole distance is increased by electron pushing and pulling effects.

9 — Mixed Frenkel/CT States in Regioregular Oligothiophene Aggregates

Poly-3-hexyl-thiophene (P3HT) is a typical material used as donor phase in BHJ nano materials for organic photovoltaic devices. Depending on the processing technique, different types of morphological packing orders exist. The material typically exhibits either a regio-regular (RR) or a regio-random (RRa) structure. Due to its optoelectrical properties, RR-P3HT is superior to RRa-P3HT, with charge carrier mobilities usually one order of magnitude higher for the RR-P3HT material [166].

While the conventional picture is that the photogenerated species in RR-P3HT are H-aggregate type excitons, it has become clear over recent years [167, 168] that photoexcitation also generates coupled charge pairs, or polaron pairs (PP). In the present section, this process of polaron pair generation is investigated by studying stacked oligomer species. Our study connects to the recent experimental investigation by de Sio et al. [168] where coherent oscillatory signals were observed and assigned to vibronic signals accompanying polaron pair generation. In related studies [169], such signals were also observed but their origin was unclear.

To study the role of charge transfer excitons, we analyze small stacks of oligothiophene tetramer (OT-4) species. We combine state-of-the-art electronic structure calculations with a linear vibronic coupling (LVC) model, either within the full dimensionality of the normal-mode space, or else using the effective-mode methods described above. Dynamical ML-MCTDH calculations are performed for this model Hamiltonian, typically for a total of 40 normal modes per fragment, amounting to 120 modes for a stacked trimer, and 200

modes for a stacked pentamer. Finally, charge separation within the donor domain can obviously influence the carrier generation at the donor/acceptor interface. This aspect will be addressed in detail in chapter 10, for a model system representative of the P3HT/PCBM donor-acceptor system.

9.1 Model Hamiltonian: Excitons and CT-Excitons in Stacked OT-4 Oligomers

The model system used to study the ultrafast polaron pair generation consists of three oligothiophene tetramer (OT-4) molecules stacked upon each other, leading to an aggregate with H-type characteristics.

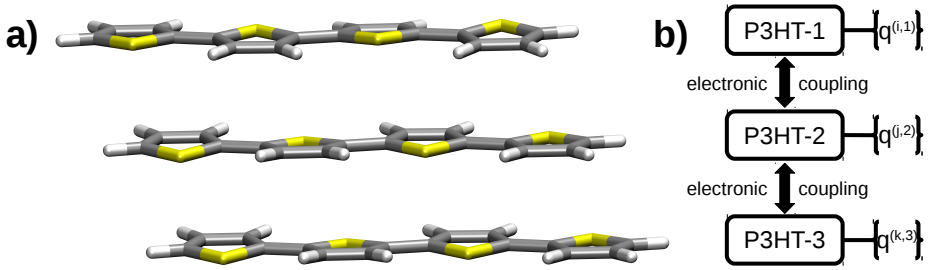

Figure 9.1: a) Molecular representation of OT-4 trimer used for the quantum dynamics simulations. b) Schematic representation of the OT-4 trimer along with its associated normal modes q and electronic couplings between the individual fragments.

Figure 9.1a and b shows the molecular geometry of the system as well as a schematic sketch of the individual molecules with their associated normal modes and the electronic couplings. Each OT-4 monomer is associated with its own subset of normal modes $\{q\}$, obtained from electronic structure calculations. The electronic coupling is obtained from a quasi diabatisation scheme which has also been used to obtain the electronic couplings for the investigation in the previous chapter [158, 159], see also section 4.3 for details.

As in the preceding section, the corresponding model Hamiltonian is set up in single excitation subspace in a generalized electron-hole (e-h) representation. The electron is located at site $\nu_e = \nu$, whereas the hole is located on site $\mu_h = \mu$. Localised e-h pairs (i.e. electron and hole located on the same fragment) correspond to a Frenkel excitonic configuration (XT), $|XT_i\rangle = |\nu = i, \mu = i\rangle$ (with $i = 1, \ldots, 3$). Conversely, if an e-h pair is not located on the same fragment, the configuration represents a charge transfer (CT) state,

i.e. $|M_i^+ M_j^-\rangle = |\nu = i, \mu = j \neq i\rangle$. Here, we have made the approximation that electron and hole are always located on neighboring fragments. In a more generalised approach, one would not restrict the distance between an e-h pair to one fragment, but also allow the population of CT states with $|M_i^+ M_j^-\rangle = |\nu = i, \mu = j = i+1, i+2, i+3, \ldots\rangle$. In the presented simulations, a total of three OT-4 molecules has been used along with seven electronic states (three XT and four CT states).

The overall Hamiltonian $\hat{H}$ can be split into three terms,

$$\hat{H} = \hat{H}_0^{el} + \hat{H}_0^{ph} + \hat{H}^{vibronic} \tag{9.1}$$

where the first term ($\hat{H}_0^{el}$) corresponds to the purely electronic part of the Hamiltonian including the electronic couplings, while the second term ($\hat{H}_0^{ph}$) corresponds to the zeroth-order vibrational (phonon) Hamiltonian, and the third term ($\hat{H}^{vibronic}$) subsumes all vibronic interactions. The electronic part of the Hamitonian reads as follows,

$$\begin{aligned}
\hat{H}_0^{el} = {} & \epsilon_{XT} \sum_{i=1}^{3} |XT_i\rangle \langle XT_i| + \epsilon_{CT} \sum_{i=1}^{2} \left(|M_i^+ M_{i+1}^-\rangle \langle M_i^+ M_{i+1}^-| + |M_{i+1}^+ M_i^-\rangle \langle M_{i+1}^+ M_i^-| \right) \\
& + J \sum_{i=1}^{2} |XT_i\rangle \langle XT_{i+1}| + h.c. \\
& + K_1 \left(|XT_1\rangle \langle M_1^+ M_2^-| + |XT_2\rangle \langle M_1^- M_2^+| + |XT_2\rangle \langle M_2^+ M_3^-| + |XT_3\rangle \langle M_2^- M_3^+| + h.c. \right) \\
& + K_2 \left(|XT_1\rangle \langle M_1^- M_2^+| + |XT_2\rangle \langle M_1^+ M_2^-| + |XT_2\rangle \langle M_2^- M_3^+| + |XT_3\rangle \langle M_2^+ M_3^-| + h.c. \right)
\end{aligned} \tag{9.2}$$

Here, the first two terms are the on-site energies for the different states, i.e. excitonic (ϵ_{XT}) and charge transfer states (ϵ_{CT}). The third term J is the electronic diabatic coupling between the excitonic states and the K_i terms are the exciton to charge transfer state couplings.

The zeroth-order vibrational part is given as follows within the harmonic approximation,

$$\hat{H}_0 = \sum_{i=1}^{N_{OT4-1}} \frac{1}{2}\omega_i (p_i^2 + q_i^2) + \sum_{j=1}^{N_{OT4-2}} \frac{1}{2}\omega_j (p_j^2 + q_j^2) + \sum_{k=1}^{N_{OT4-3}} \frac{1}{2}\omega_k (p_k^2 + q_k^2) \tag{9.3}$$

Here, each monomer i, j and k has its own subset of site-local degrees of freedom.

Next, the vibronic part of the Hamiltonian can be represented as a sum over local and non-local contributions,

$$\hat{H}^{vibronic} = \hat{H}^{local} + \hat{H}^{nonlocal} \tag{9.4}$$

While all modes are taken to be local in our model (i.e., confined to a given fragment), the local or non-local nature of the vibronic couplings depends on the nature of the excited state, i.e., on whether we are considering a localised excitonic state (local) or a charge transfer configuration (non-local). Specifically, the local vibronic contributions involve the excitonic states,

$$\hat{H}^{local} = \sum_{i=1}^{N_{OT4-1}} c_i q_i \left|XT_1\right\rangle \left\langle XT_1\right| + \sum_{j=1}^{N_{OT4-2}} c_j q_j \left|XT_2\right\rangle \left\langle XT_2\right| + \sum_{k=1}^{N_{OT4-3}} c_k q_k \left|XT_3\right\rangle \left\langle XT_3\right| \tag{9.5}$$

while the non-local vibronic contributions involve the charge-separated species,

$$\begin{aligned}\hat{H}^{non-local} = & \sum_{i=1}^{N_{OT4-1}} \kappa_i q_i \left(\left|M_1^+ M_2^-\right\rangle \left\langle M_1^+ M_2^-\right| + \left|M_1^- M_2^+\right\rangle \left\langle M_1^- M_2^+\right|\right) \\ & + \sum_{j=1}^{N_{OT4-2}} \kappa_j q_j \Big[\left(\left|M_2^+ M_1^-\right\rangle \left\langle M_2^+ M_1^-\right| + \left|M_2^+ M_3^-\right\rangle \left\langle M_2^+ M_3^-\right|\right) \\ & + \left(\left|M_2^- M_1^+\right\rangle \left\langle M_2^- M_1^+\right| + \left|M_2^- M_3^+\right\rangle \left\langle M_2^- M_3^+\right|\right)\Big] \\ & + \sum_{k=1}^{N_{OT4-3}} \kappa_k q_k \left(\left|M_3^+ M_2^-\right\rangle \left\langle M_3^+ M_2^-\right| + \left|M_3^- M_2^+\right\rangle \left\langle M_3^- M_2^+\right|\right)\end{aligned} \tag{9.6}$$

Since the charge transfer states are defined between two fragments, the corresponding vibronic couplings are also non-local and hence defined between two fragments.

The electronic part of the Hamiltonian shown in equation 9.2 can be rewritten in matrix form, highlighting the coupling between the different excitonic and charge transfer states.

$$H_0^{el} = \begin{pmatrix} \epsilon_{XT} & J & & K_1 & & K_2 & \\ & \epsilon_{XT} & J & K_2 & K_1 & K_1 & K_2 \\ & & \epsilon_{XT} & & K_2 & & K_1 \\ & & & \epsilon_{CT} & & & \\ & & & & \epsilon_{CT} & & \\ & & & & & \epsilon_{CT} & \\ & & & & & & \epsilon_{CT} \end{pmatrix} \tag{9.7}$$

The on-site energies, vibronic couplings and diabatic electronic couplings are based on electronic structure calculations employing density functional theory on a ground state optimised oligothiophene stack, composed of an OT-4 dimer. Due to the huge size of a stacked oligothiophene chain, the ground state optimised structure has been obtained from density functional theory using the ωB97XD [147] and SVP basis set [148, 149] as implemented in Gaussian09 [150].

9.2 Electronic Structure Calculations

The electronic structure calculations have been carried out using a stacked dimer of two OT-4 molecules. From these dimer calculations, all the relevant parameters for the quantum dynamics simulations have been obtained, i.e. excitation energies, diabatic couplings and vibronic couplings. Most of the electronic structure calculations have been carried out using DFT methods, i.e. the ωB97XD functional as implemented in the Gaussian09 software package. However, due to the expected high charge transfer character, high-level *ab initio* methods such as ADC(2) were performed as well in order to validate the reliability of the mentioned DFT functional. In particular, it has been shown by H. Lischka and collaborators that ωB97XD gives good results for P3HT when compared to ADC(2) [153]. We could confirm this observation in our calculations, see figure 9.2. All excited state calculations are based on the optimised ground state geometry.

Figure 9.2 shows the comparison of the excited states between the ωB97XD DFT method and the ADC(2) wave function based method. From the transition density plots one can see that the the ωB97XD DFT functional and the ADC(2) wave function method

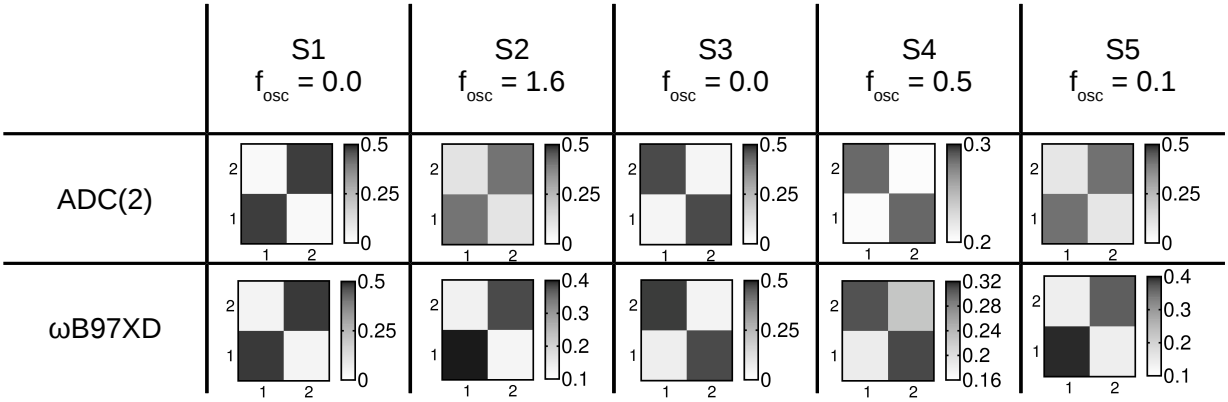

Figure 9.2: Properties from the analysis of the transition density matrices for a stacked oligothiophene chain, composed of two OT-4 molecules, as provided by the TheoDORE program package [154–156]. The x-axis represents the position of the electron, whereas the y-axis represents the position of the hole. Diagonal entries correspond to the XT manifold, off-diagonal entries correspond to the CT manifold. In both cases, the DFT optimised ground state structure has been used. The excited states of the upper row have been calculated with the ADC(2) method, the excited states of the lower row with the ωB97XD functional. In both cases, the SVP basis set was employed.

are in excellent agreement. Both methods describe the first two excited states as mainly Frenkel states, with the S2 state exhibiting a non negligible CT character. The S3 state is in both cases a pure CT state. Furthermore, the S3-S2 gap between the two electronic states is similar for both methods, namely 0.48 eV for the ωB97XD functional and 0.51 eV for the ADC(2) method.

In view of the good performance of the ωB97XD DFT functional, the vibronic coupling constants have been calculated using TDDFT calculations with the ωB97XD DFT functional.

Figure 9.3a shows the vibronic coupling constants associated with each normal mode of the system. As one can see, there are two dominant modes, which are collective modes of CC stretch type. These two modes exhibit large vibronic coupling values since they belong to deformations within the π electronic structure and are therefore responsible for the optical properties of the system.

Furthermore, there exist a lot of very small vibronic coupling constants contributing to the overall spectral density of the system. From equation 7.9 one can see that the value of

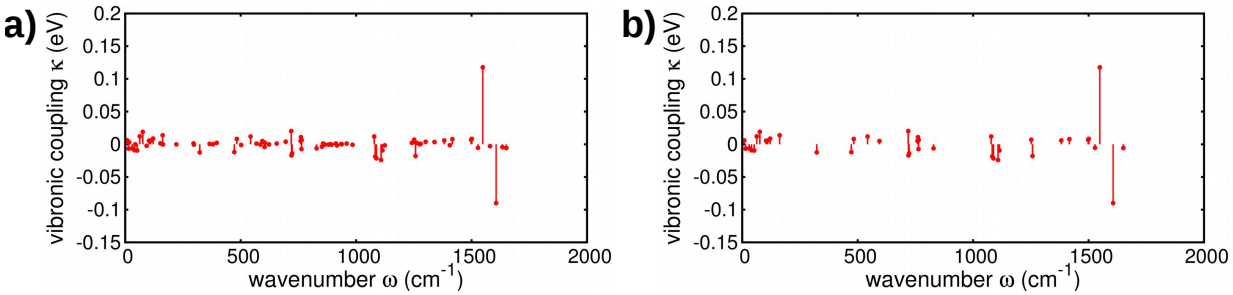

Figure 9.3: Calculated vibronic couplings κ for the bright S2 state from the calculation of an OT-4 dimer. One fragment was chosen to be frozen, while the normal modes of the other fragment have been used for the determination of the vibronic couplings. a) Full normal mode vibronic couplings. b) Normal mode vibronic couplings above a threshold value of 0.005 eV. The reorganisation energy changes only marginally.

the vibronic coupling corresponds to the shift of the excited state minimum. Hence, small values of the vibronic coupling constant are equal to a small and mostly negligible shift in the excited state minimum and therefore, these modes do not contribute much to the excited state dynamics.

For the subsequent dynamics a threshold value has been introduced which eliminates couplings below this specific value. Since the vibronic couplings are related to the reorganisation energy λ via $\lambda = \sum_i \kappa_i / 2\omega_i$, the threshold value should not be chosen too generously, as it can change the overall dynamics of the system. Figure 9.3b shows the reduced set of vibronic couplings after imposing a threshold value. The difference in reorganisation energy between the full normal mode representation and the reduced set of normal modes is 3% and thus, the approximation should give reliable results.

Another important characteristic for the dynamics is the relation between the difference in on-site energies and the diabatic couplings. Electronic couplings are going to have a significant effect if they fall into a similar ranges as the differences between on-site energies.

From table 9.1 one can see that the difference in on-sit eenergies between the bright XT and CT state is 0.48 eV. Interestingly, the diabatic coupling is nearly half of this energy splitting, and will therefore likely give rise to an ultrafast charge transfer. Furthermore, one can see that the excitonic coupling J has a positive sign, conforming to the assumption of an H-aggregate type wave function.

Table 9.1: On-site energies and diabatic couplings obtained from *ab initio* calculations. The on-site energies have been obtained from ωB97XD, whereas the diabatic couplings have been obtained using the LC-BLYP functional. All parameters are given in eV.

On-site energies		Diabatic couplings		
ϵ_{XT}	ϵ_{CT}	K_1(LUMO)	K_2(HOMO)	J
0.00	0.48	0.23	0.09	0.12

With the information about the electronic part at hand, one can diagonalise the electronic part of the Hamiltonian, shown in equation 9.2. This will give information about the adiabatic state distributions and allow a first guess at the subsequently following dynamics.

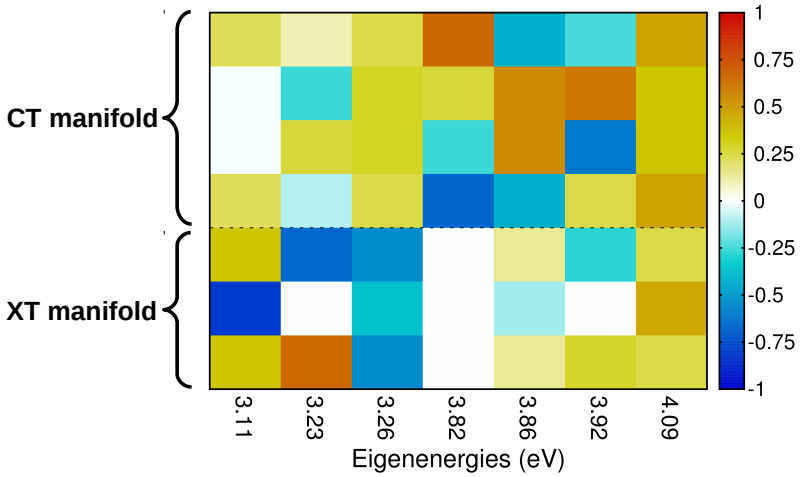

Figure 9.4: Graphical representation of the eigenvectors of the numerically diagonalised electronic Hamiltonian shown in equation 9.2. The eigenvectors are plotted columnwise and in ascending order. Entries below the dashed line correspond to the excitonic manifold, while entries above the dashed line correspond to a charge transfer configuration.

Figure 9.4 shows a graphical representation of the eigenvectors and eigenvalues of the numerically diagonalised electronic Hamiltonian. Entries below the dashed line correspond to the XT manifold, while entries above the dashed line correspond to the CT manifold. The eigenvectors are shown columnwise in ascending order. For the model system shown in figure 9.1, the bright state is the S3 state. From the eigenvector analysis, one can infer that the S3 state exhibits a non negligible mixing with the CT states, which is in agreement with the analysis of the electron-hole distribution for the dimer system shown in figure 9.2.

The lowest energy state also shows a significant mixing of the XT manifold with the CT manifold. Additionally, one can see that the population of the fragment in the middle is the highest, indicating a localisation of the excitonic portion of the wave packet on this particular fragment.

9.3 Dynamics Simulations

9.3.1 Quantum Dynamics in Normal Mode Representation

Quantum dynamics simulations have been carried out using the ML-MCTDH method, as in the previous chapter. The model system features a total of three OT-4 molecules and seven electronic states. As has been pointed out in the previous section, a reduced set of normal modes has been used for the quantum dynamics simulations, leading to a total of 120 normal modes (40 per fragment). In recent time resolved experiments, very short pulses with a duration of a few femtoseconds have been used [170]. The generation of these pulses comes with the cost of a very large spectral width, suggesting that the entire excitonic manifold is excited, creating an electronic wavepacket. Therefore, we report here on simulations using a localised excitation on the central OT-4 fragment.

Figure 9.5a shows the diabatic populations of a simulation with a localised initial condition. One can see that a very fast decay of the initially localised wave packet occurs during the first few femtoseconds, which is accompanied by fast oscillations. These rapid oscillations also appear in the population traces of the charge transfer states, indicating a transfer between the intially localised excitonic wave packet and the charge transfer states. Furthermore, one can see that slower oscillations appear in the population traces on longer time scales. In figure 9.5b one can see the spatially resolved electron-hole populations. At the beginning of the simulation, the excitonic wave packet is localised on the central OT-4 fragment, see also figure 9.1a and b. During the first ten femtoseconds, the excitonic wave packet splits into a coherent superposition of an excitonic wave packet and a charge transfer state and subsequently relocalises again. This splitting and relocalisation possibly give rise to the fast oscillations, seen in the upper population plot. It is also worth noting that the results from the diagonalisation of the electronic Hamiltonian shown in figure 9.4 indicate that the lowest energy state has a high contribution of excitonic character for the

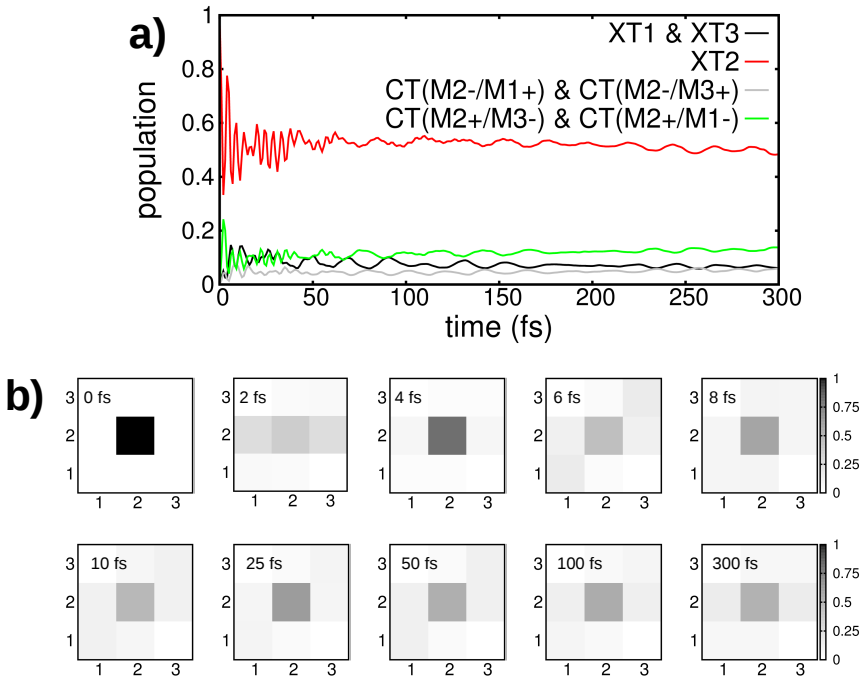

Figure 9.5: Diabatic electronic populations for a P3HT trimer with a localised initial condition on P3HT-2, see also figure 9.1b. a) One dimensional plot of the diabatic populations for excitonic and charge transfer states. b) Electron hole resolved populations for selected time cuts. The x-axis represents the position of the hole while the y axis represents the position of the electron. Numbers refer to the respective P3HT-i fragment. Electron and hole occupying the same fragment represent a Frenkel exciton state.

P3HT-2 fragment, which is also the result of the present dynamical simulations.

In addition to the analysis of the populations, electronic coherence between excitonic and charge transfer states has been analyzed. Electronic coherence corresponds to the off-diagonal elements of the electronic density matrix and, hence, to expectation value of off-diagonal operators like $\hat{C} = |\mathrm{XT}\rangle\langle\mathrm{CT}|$, i.e.,

$$\begin{aligned} \rho_{\mathrm{XT,CT}}(t) &= \mathrm{Tr}\{\,|\mathrm{XT}\rangle\langle\mathrm{CT}|\,\hat{\rho}(t)\} \\ &= \mathrm{Tr}\{\,|\mathrm{XT}\rangle\langle\mathrm{CT}|\,|\Psi(t)\rangle\langle\Psi(t)|\} \\ &= \langle\Psi(t)|\mathrm{XT}\rangle\langle\mathrm{CT}|\,\Psi(t)\rangle \end{aligned} \tag{9.8}$$

where the trace (Tr) refers to the electronic and phonon modes and the density operator $\hat{\rho}(t) = |\Psi(t)\rangle\langle\Psi(t)|$ derives from the time-evolving overall wave function state from the MCTDH propagation. The electronic coherence indicates the presence of a coherent super-

position state whose characteristic phase factor derives from the transition energy between the relevant states, i.e., differences in adiabatic egenvalues. For a two-state system, this can be straightforwardly seen as follows, for a wave function of the form,

$$|\Psi(t)\rangle = c_1\, e^{-iE_1 t/\hbar}|1\rangle + c_2\, e^{-iE_2 t/\hbar}|2\rangle \tag{9.9}$$

such that the electronic coherence matrix element ρ_{12} read as follows,

$$\rho_{12} \;=\; \langle\Psi(t)|1\rangle\langle 2|\Psi(t)\rangle = c_1^* c_2 e^{i(E_1-E_2)t/\hbar} \tag{9.10}$$

where the orthogonality of the states $|1\rangle$ and $|2\rangle$ was used.

In general, information about the adiabatic eigenvalues of the system can be obtained from the Fourier transformation of the wavepacket autocorrelation function $C(t) = \langle\Psi(t=0)|\Psi(t)\rangle$, yielding the absorption spectrum.

In high-dimensional systems, it is often found that the imaginary part of the electronic coherence, which determines the state-to-state population flux, decays to zero after a transient period, while the real part of the electronic coherence persists, indicating that a coherent superposition state persists. This is illustrated, e.g., in Figure 6.7 of the previous chapter.

The analysis of the electronic coherence will be performed first for the electronic Hamiltonian in the absence of vibrational contributions. Afterwards, the full Hamiltonian as shown in equations 9.1 to 9.6 will be analysed.

Figure 9.6a shows the real part of the expectation value of the electronic coherence between the excitonic state located on the center fragment and a corresponding charge transfer state. One can see that the electronic coherence features two different oscillatory signals, one with a fast periodicity and a second with a slower periodicity. Transforming these data from the time domain to the frequency domain by a Fourier transformation yields the spectrum shown in figure 9.6b. According to equation 9.10, each of these peaks corresponds to a transition between two states with an energy difference as obtained from the spectrum. In order to assign the peaks to certain transitions, one has to know the adiabatic eigenvalues of the system, which are obtained by Fourier transforming the auto-

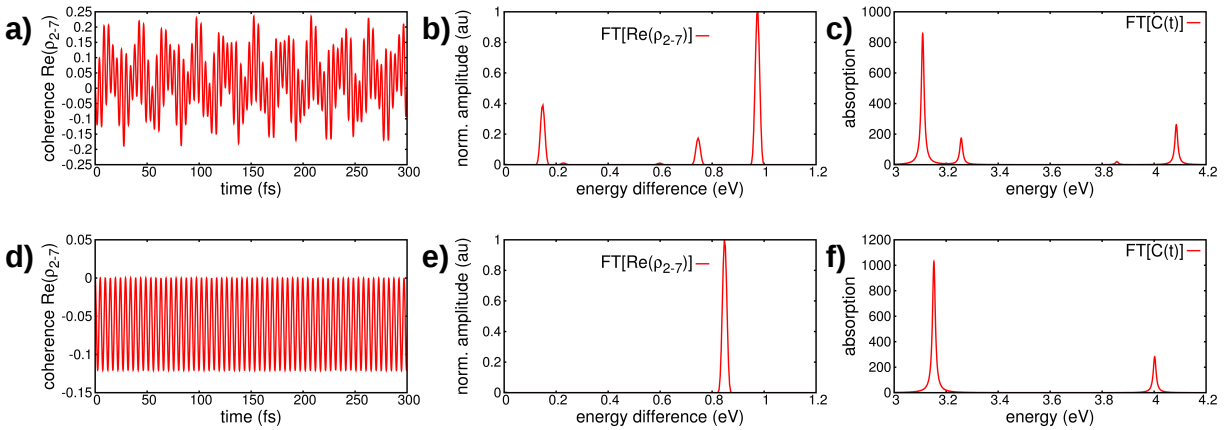

Figure 9.6: a-c: Simulations employing only the electronic Hamiltonian with all couplings. a) Time resolved expectation value of the electronic coherence ρ_{2-7}, where the states 2 and 7 correspond to an excitonic and a charge transfer state, b) Fourier transformation of a. c) Fourier transformation of the autocorrelation function C(t) to obtain the absorption spectrum needed to interpret panel b.
d-f: Simulations employing only the electronic Hamiltonian without the excitonic coupling J. d) Time resolved expectation value of the electronic coherene ρ_{2-7}. e) Fourier transformation of d. f) Fourier transformation of the autocorrelation function C(t).

correlation function $C(t)$, yielding the absorption spectrum in figure 9.6c. Here, the state at 3.26 eV is the excitonic state corresponding to the bright state in an H-type aggregate. The state at 3.1 eV is the dark state in an H-type aggregate. The peaks at 3.86 and 4.09 eV correspond to the charge transfer states. The configuration of these adiabatic states can be identified from the representation of the eigenvectors in figure 9.4. One can see that the lowest energy state at 3.11 eV corresponds mostly to an excitonic configuration on the center fragment. The bright state at 3.26 eV corresponds to a delocalised excitonic configuration.

With the aid of the absorption spectrum of figure 9.6c one can infer that the peak at 0.14 eV in figure 9.6b stems from the transition of the third state to the first state, which would correspond to an excitonic transition, since the third and first state have a very high excitonic character of 73 and 90 percent, respectively. The peak at approximately 1.0 eV corresponds to the transition from the first to the seventh state, which is mainly the transfer from the excitonic to the charge transfer state.

Figures 9.6d-f correspond to a simulation with no excitonic coupling present, i.e. $J = 0$ in equation 9.2. Hence, only the transfer between the excitonic and the charge transfer state is allowed. This is also reflected in the coherence, shown in figure 9.6d. Here, only the fast oscillatory pattern of figure 9.6a remains, which stems from the exciton-to charge-transfer state dynamics. Subsequently, only one peak emerges from the corresponding Fourier transformation, which corresponds to the energy gap of the excitonic and charge transfer state, as can be seen from figure 9.6f.

After the analysis of the electronic coherence in the absence of any normal modes, the same analysis protocol has been applied to the simulation with a total of 120 degrees of freedom. In contrast to the one dimensional Fourier transformation in the analysis above, a windowed Fourier transform is used, such that the 1D time-domain data set is translated to a 2D time-frequency domain representation. A Hann filter is used for the moving time-domain window [171], as implemented in the MatLab software suite [172]. A window width of 50 femtoseconds has been used.

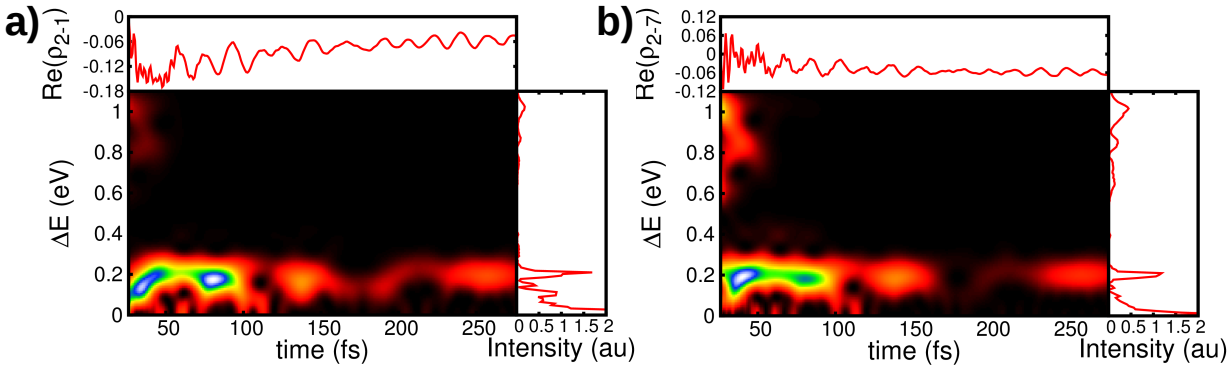

Figure 9.7: Two dimensional Fourier transformations of the full system Hamiltonian employing seven electronic states and 120 normal modes and a localised initial condition on the P3HT-2 fragment, see also figure 9.1b. a) Fourier transformation of the XT-XT ρ_{2-1} coherence. b) Fourier transformation of the XT-CT ρ_{2-7} coherence. Upper panels: Expectation value of the respective coherence, damped with an exponential function and a time constant of 200 fs. Right panels: one dimensional Fourier transformation of the electronic coherence.

Figures 9.7a and b show the two dimensional windowed Fourier transformation of the electronic coherence between two XT states (figure 9.7a, ρ_{2-1}) and between an XT state and a CT state (figure 9.7b, ρ_{2-7}). Comparing these two figures, one can see that the two

dimensional Fourier transforms are quite similar. Both figures show a dominant contribution in the 0.2 eV frequency region on the short time scale as well as on a longer time scale. Additionally, the Fourier transformation of the XT-CT coherence ρ_{2-7} also shows a high-frequency contribution in the 1 eV region on the short time scale. Based on the above analysis of the electronic coherence, this contribution can be assigned to the XT-CT transition, which is characteristic of the analysed coherence. A significant difference between the two simulations can be seen in the intensity of the low frequency 0.2 eV signal. Comparing these intensities for the ρ_{2-1} XT-XT and ρ_{2-7} XT-CT coherence, one can see that the 0.2 eV signal is much stronger for the XT-XT coherence (1.9 eV) than for the XT-CT coherence (1.1 eV).

Considering the spectral density in figure 9.3 once again, it is obvious that the highest contribution to the spectral density arises from normal modes centered around 1500 cm^{-1} (approx. 0.2 eV), i.e. in the same spectral range as the low frequency signal obtained from Fourier transforming the electronic coherence. From the above analysis of the pure electronic dynamics, it is known that the low frequency signal stems from excitonic coherence, initiated by the delocalisation of the initially localised wave packet. In conjunction with the presented analysis we therefore conclude that a combination of excitonic couplings and normal modes both contribute to the observed signal. This also explains why the low frequency 0.2 eV signal is more intense for the ρ_{2-1} XT-XT coherence than for the ρ_{2-7} XT-CT coherence.

9.3.2 Effective Mode Dynamics

As it has been pointed out in the introductory part of chapter 9 and section 7.4, an effective mode decomposition of the normal mode representation has been done in order to reduce the total number of degrees of freedom, while keeping the physical properties of the system unchanged. The model Hamiltonian used for the dynamics is the same as for the normal mode approach, except that it is now set up in the basis of effective modes $\{X_i\}$ instead of a normal mode basis $\{x_i\}$. Since both approaches are based on the LVC approach, the model Hamiltonians shwon in equations 9.1 to 9.6 can be used for the dynamical treatment of both methods. In the following, the results with different layers of effective modes will be presented. The n-th layer dynamics feature a total of 7N effective modes.

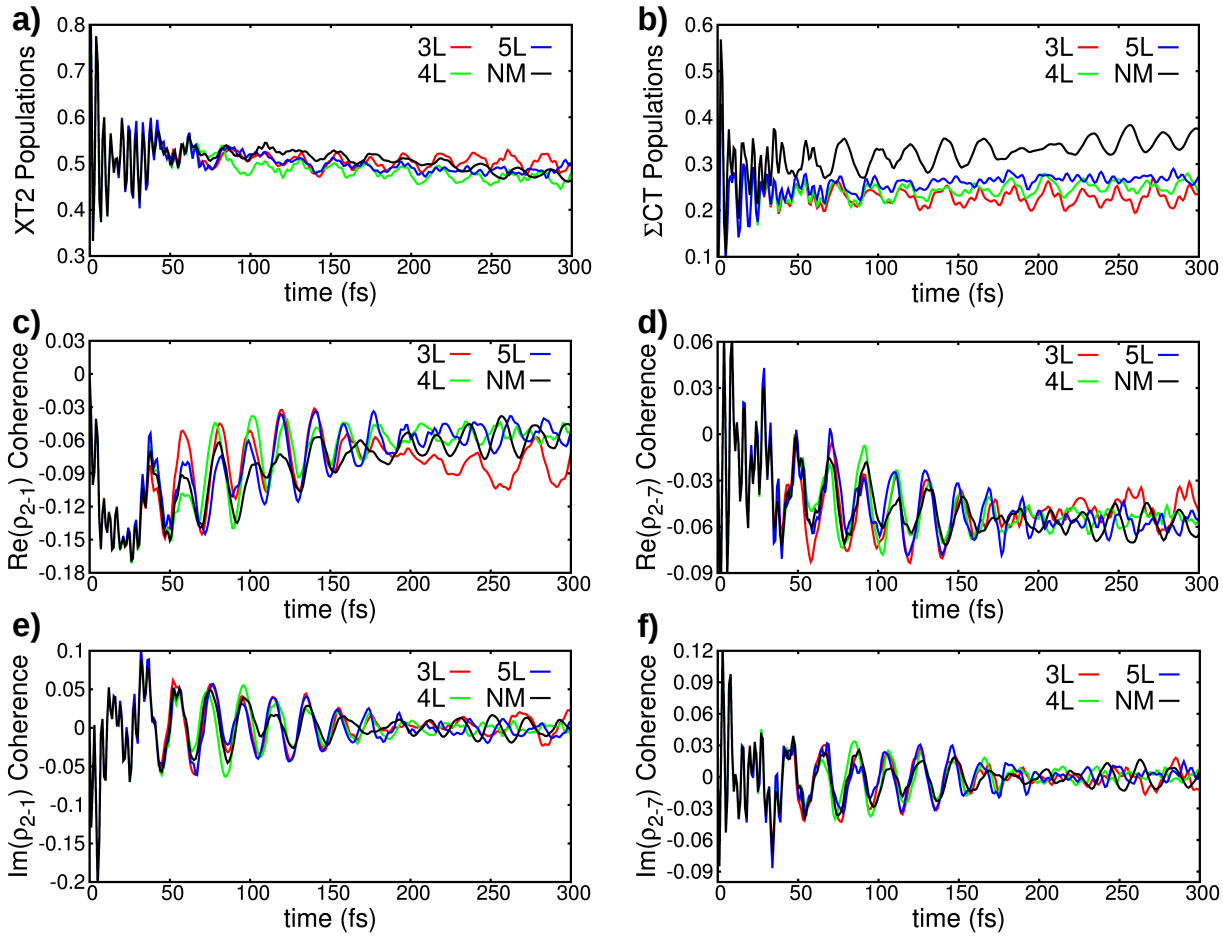

Figure 9.8: Comparison of the diabatic populations and electronic coherences of different effective mode layers with the normal mode ansatz. a) Diabatic XT2 populations. b) Diabatic charge transfer populations. c) Real part of the electronic ρ_{2-1} coherence. d) Real part of the electronic ρ_{2-7} coherence. e) Imaginary part of the electronic ρ_{2-1} coherence. f) Imaginary part of the electronic ρ_{2-7} coherence.

Figure 9.8a and b show the diabatic populations of the XT2 state and of the sum over CT states ($\sum$CT), for different numbers of effective-mode layers. For reference, the dynamics in the normal-mode representation are shown in black. While the XT2 state populations, shown in figure 9.8a, are exactly reproduced for the short time dynamics and differ only slightly for longer times for three layers of effective modes, the charge transfer populations, shown in figure 9.8b, differ more, even for 5 layers of effective modes. Nevertheless, the qualitative behaviour is reproduced by the effective mode approach.

Figure 9.8c and d show the real part of the expectation value of the electronic coherence between two XT states and between an XT and CT state, respectively. While the short time dynamics are represented exactly for all layers under investigation, the three-layer simulations differ again for longer times. The four and five-layer simulations also represent the qualitative behavior of the normal mode simulations quite well.

As for the simulations employing the normal mode ansatz, a windowed Fourier transformation of the electronic coherences is performed for the different layers of effective modes. The same window width and Hann filter as for the previously shown Fourier transformations has been used.

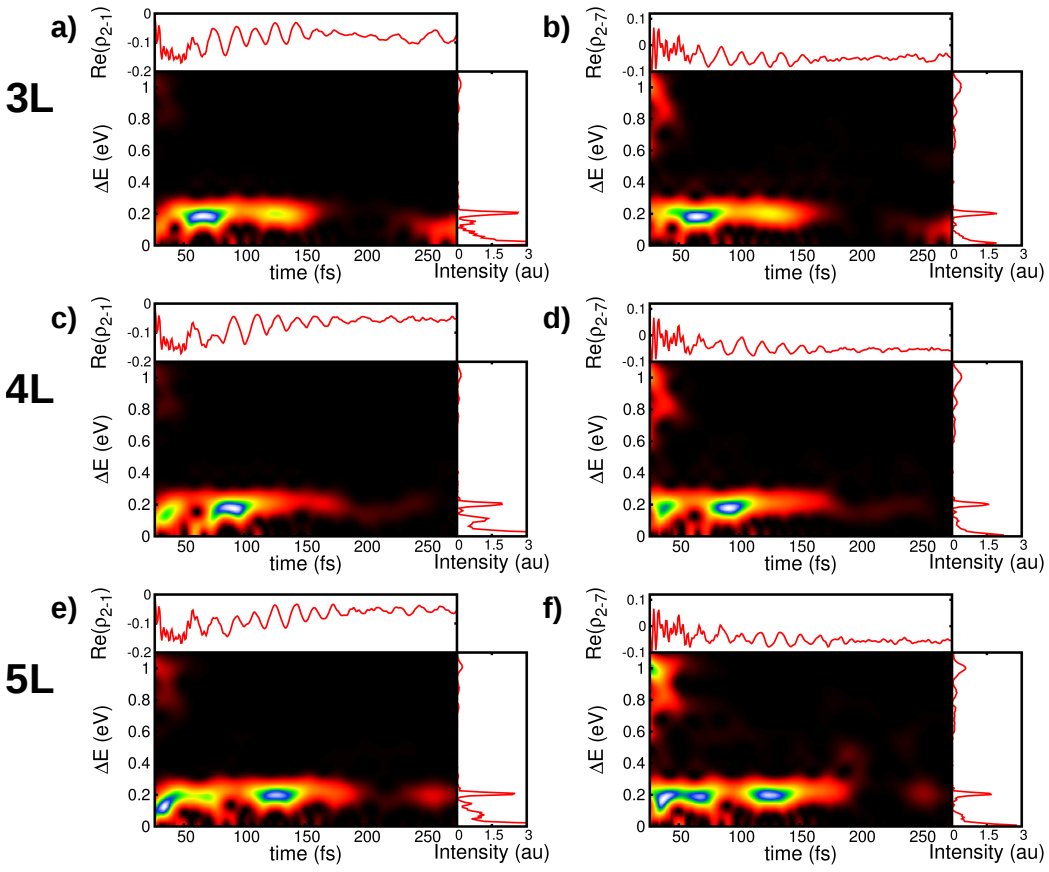

Figure 9.9: Two dimensional Fourier transformation of different layers of effective modes. a) and b) Real part of the ρ_{2-1} and ρ_{2-7} electronic coherence for 3 effective mode layers. c) and d) Real part of the ρ_{2-1} and ρ_{2-7} electronic coherence for 4 effective mode layers. e) and f) Real part of the ρ_{2-1} and ρ_{2-7} electronic coherence for 5 effective mode layers.

Figures 9.9a to f show the two dimensional Fourier transformation of the real part of the electronic ρ_{2-1} and ρ_{2-7} coherences, respectively. Comparing these results to the normal-mode Fourier transformation in figure 9.7a and b, one can clearly see that the same behaviour could be reproduced by the effective mode ansatz. For figures 9.9a, c and e one can see that a dominant contribution in the 0.2 eV regime can be seen, which is apparent over nearly the whole simulation time. From the analysis done in the previous section, this signal can be assigned to excitonic coherence, due to a delocalisation effect, since a localised initial condition has been used. In contrast, figures 9.9b, d and f show an additional signal at approximately 1.0 eV. This signal can be assigned to the XT-CT transfer. As for the simulation employing the normal mode approach, one could see that the intensities of the 0.2 eV and 1.0 eV signals change depending on the observed coherence, i.e. the ρ_{2-1} or the ρ_{2-7} coherence. This is also the case for the simulation employing the normal mode approach. For all three simulations employing different layers of effective modes, one can see that the 1.0 eV signal rises, depending on the observation of the Fourier transformation of coherence ρ_{2-1} or coherence ρ_{2-7}. At the same time, the 0.2 eV signal loses intensity. Both observations are in agreement with the normal mode simulations.

9.3.3 Summary and Conclusion

Recent experimental investigations performed on RR-P3HT indicated the formation of polaron pairs, accompanied by coherent oscillatory signals. In order to elucidate the mechanism of the polaron pair formation and the origin of these oscillatory signals, high level electronic structure calculations have been carried out in order to parametrise a high-dimensional model Hamiltonian within the linear vibronic coupling framework. Ground-state DFT calculations on a stacked OT-4 oligomers have been performed in order to obtain the ground state normal modes which are necessary for the construction of the linear vibronic coupling Hamiltonian. Furthermore, excited electronic states have been calculated within the same framework and compared against high level *ab initio* ADC(2) calculations. In particular, the electron and hole distribution per chain has been analysed. The result showed that the electronic bright state, corresponding to an H-type aggregate features already a minor mixture between the locally excited state and charge transfer states. Based on the ground state optimsed structure, electronic diabatic couplings between the excitonic and charge transfer state have been calculated. While the splitting between the excitonic and charge transfer state is very large, the diabatic couplings are approximately 1/2 of this

energy gap, indicating a fast and efficient transfer.

The quantum dynamics simulations have been carried out using the ML-MCTDH program. The model Hamiltonian featured a total of three P3HT chains, each consisting of a reduced set of 40 normal modes. Furthermore, seven electronic states have been included in the dynamical treatment. While the main focus was put on the analysis of the electronic coherence between an excitonic and a charge transfer state, the population analysis showed that an efficient and fast charge transfer state formation could be observed. This is in agreement with an analysis of adiabatic eigenvalues of the electronic Hamiltonian, which predicted a localisation of the excitonic wave packet in the middle of the stack and a non-negligible amount of charge transfer. The analysis of the electronic coherence revealed two main processes within the system. Firstly, there is the transfer from the excitonic to the charge transfer manifold, associated with a high frequency oscillation of about 1.0 eV. Secondly, there is a lower-frequency process in the 0.2 eV region. This process could be explained by a combination of excitonic delocalisation and normal mode contributions. Due to the huge number of degrees of freedom for the system, the low frequency process is subjected to contributions from normal modes in the same frequency regime. By analysing the spectral density, one can see that the modes located in the same frequency regime as the excitonic delocalisation have a large impact on the excited state dynamics. The interaction between the excitonic delocalisation and the normal modes in the same frequency regime lead to an increase of the low frequency signal, which could be responsible for the coherent oscillations in recent experiments. In addition to the simulations performed within the normal mode representation, an effective mode decomposition of the normal mode subspace $\{x_i\}$ into varying layers of effective modes $\{X_i\}$ has been performed. Our results from quantum dynamical simulations showed remarkable similarities to the results obtained from the normal mode approach, while reducing the computational effort.

Though the present study may explain the coherent oscillations found in recent experimental studies on RR-P3HT, still some uncertainties remain. On the one hand we did not include the influence of temperature on the dynamics, i.e. the simulations are carried out at 0 K. In a real system, temperature effects will lead to more flexibility in the system and hence, to local trapping effects or a faster decoherence of the wave packet, which in turn will lead to less long-lived coherent oscillations. Furthermore, the model system featured only a total of four charge transfer states, since the electron-hole distance has been lim-

ited to one monomer. Including long-range electron-hole separation might also change the overall dynamics. While one could argue that a stack consisting of three OT-4 molecules might be too small, analogous simulations for five stacked OT-4 units did not show any noticeable differences in the dynamics.

Overall, a comprehensive study of the excited state dynamics of a small model fragment representing RR-P3HT with a large number of degrees of freedom has been presented, and coherent effects have been explained in terms of electronic and vibrational coherence.

10 — Charge Carrier Generation in a P3HT/PCBM Model System

The combination of Poly(3-hexylthiophene-2,5-diyl) (P3HT) and the fullerene derivative [6,6]-phenyl-C_{61} butyric acid methyl ester (PCBM) is a well known organic photovoltaic system, whose charge separation dynamics has been studied extensively by both theoretical and experimental groups [131, 173–175]. The experimental studies report on an ultrafast ($\sim$ 50 fs) formation of a interfacial charge transfer state, while the subsequent generation of free carriers can be either ultrafast or slow, depending on the material's morphology [175]. In particular, a regioregular morphology has been shown to favor ultrafast long-range charge separation. In view of this, it is conjectured that due to the delocalisation of carrier species in regioregular architectures, the effective Coulomb barrier is significantly decreased, which will lead to ultrafast free charge carrier formation. Furthermore, the effect of hot charge transfer states has also been invoked in order to explain these findings [45].

In a recent study in our group [131], a model Hamiltonian for a regioregular P3HT/PCBM system was constructed where both excitonic and carrier delocalization was taken into account. In the present work, this Hamiltonian is augmented by the presence of charge separated states in the donor (P3HT) domain. To this end, the Hamiltonian developed in the preceding section is combined with the model of [131]. The present study is aimed to show whether the generation of charge transfer excitons in the P3HT domain is (i) favorable to free carrier generation, due to additional pathways for charge separation, or (ii) unfavorable since the additinal charge-separated species act as traps.

In combination with the previous findings, where an efficient formation of P3HT/P3HT charge separated states could be observed, a model Hamiltonian to study the ultrafast dynamics in a P3HT/PCBM BHJ including the aforementioned P3HT/P3HT charge sep-

arated states has been constructed and used for high-dimensional quantum dynamical simulations.

The parametrization of the model is entirely in line with [131]. An effective mode approach has been used [125, 176], as discussed earlier. The effect of P3HT charge transfer excitons can therefore be assessed by direct comparison with the previous results for this system.

10.1 Introduction and Model Hamiltonian

The model system that is studied consists of 13 P3HT monomers and a single PCBM "super-site" (subsuming the distribution of a PCBM aggregate which is not accounted for explicitly), in line with the study of [131].

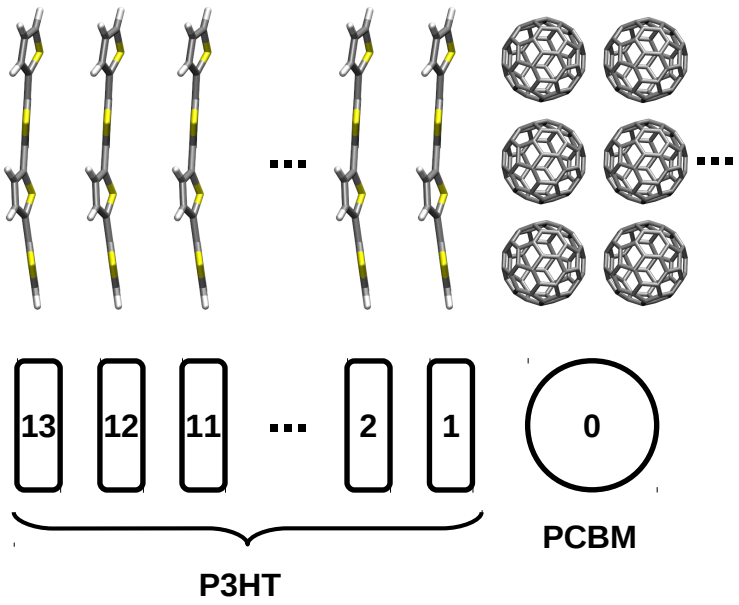

Figure 10.1: Sketch of the simulation setup featuring a total of 13 P3HT monomers as electron donors and a PCBM manifold as an electron acceptor. With respect to the electronic couplings, only nearst neighbors couplings have been employed.

An effective mode ansatz is employed, where each monomer has a total of eight effective modes obtained from the procedure outline above (see section 7.4) which results in a total of 112 degrees of freedom. The excitonic (XT type) P3HT states are coupled to each other via nearest neighbor exciton couplings. Furthermore, there are couplings between the XT and

CT state manifolds, where one now has to distinguish between (i) homomolecular charge separated (CS) states (within the P3HT domain) and (ii) heteromolecular charge transfer (CT) states (between a P3HT and the PCBM manifold). While the homomolecular XT to CT state couplings are defined between each neighboring monomer, the heteromolecular XT to CT state coupling is only defined at the interface.

As mentioned above, the model Hamiltonian represents an extension to the Hamiltonian of [131], and is also closely related to the model Hamiltonians that have been used in the previous sections. The new feature is the inclusion of homomolecular charge transfer excitons in the donor domain. The setup is again a generalised electron-hole representation $\{|\mu\nu\rangle\}$, with the electron occupying site μ and the hole occupying site ν. Locally excited states correspond to the Frenkel state manifold, with electron and hole both occupying the same monomer, i.e. $|XT_n\rangle = |\mu_n, \nu_n\rangle$, with the number n referring to the specific fragment, see figure 10.1. The Frenkel states are only defined within the P3HT manifold. Non-local occupations of electrons and holes on different monomers correspond either to the CT state manifold or the CS state manifold. Within the CT state manifold, the electron is located on the PCBM molecule, whereas the hole is located somewhere in the P3HT manifold, i.e. $|CT_{nn'}\rangle = |\mu_n, \nu_{n'}\rangle\,, n = 0, n' \neq n$. Conversely, for the CS states, both electron and hole are located within the P3HT manifold, but not on the same monomer, i.e. $|CS_{nn'}\rangle = |\mu_n, \nu_{n'}\rangle\, n \neq n' \neq 0$. The corresponding Hamiltonian is an augmented version of the Hamiltonian presented in reference [131] and can be split into an electronic part ($\hat{H}_{el}$) and an electron-phonon part ($\hat{H}_{el-ph}$),

$$\hat{H} = \hat{H}_{el} + \hat{H}_{el-ph} \tag{10.1}$$

The electronic Hamiltonian comprises on-site energies and diabatic electronic couplings,

$$\begin{aligned}\hat{H}_{el} = &\epsilon_{XT} \sum_{n}^{13} |XT_n\rangle \langle XT_n| + \sum_{n}^{13} \epsilon_{n,CT} |CT_{0,n}\rangle \langle CT_{0,n}| + \sum_{n,m}^{13} \epsilon_{n,CS} |CS_{n,m}\rangle \langle CS_{n,m}| \\ &+ J \sum_{n}^{12} (|XT_n\rangle \langle XT_{n+1}| + h.c.) + \lambda (|XT_1\rangle \langle CT_{0,1}| + h.c.) \\ &+ t \sum_{n}^{12} (|CT_{0,n}\rangle \langle CT_{0,n\pm1}| + h.c.) + K1 \sum_{n}^{12} (|XT_n\rangle \langle CS_{n,n\pm1}| + h.c.) \\ &+ K2 \sum_{n}^{12} (|XT_n\rangle \langle CS_{n,n\pm1}| + h.c.) + K (|CS_{1,2}\rangle \langle CT_{0,2}| + h.c.) \\ &+ l_e \sum (|CS_{n,n'}\rangle \langle CS_{n\pm1,n'}| + h.c.) + l_h \sum (|CS_{n,n'}\rangle \langle CS_{n,n'\pm1}| + h.c.) \end{aligned} \tag{10.2}$$

The first three terms of 10.2 are the on-site energies for the XT, CT and CS states, respectively. All on-site energies are taken from electronic structure calcaulations employing the TDDFT level of theory, in conjunction with the LC-BLYP functional as detailed in references [158, 177]. The on-site energies of the CT states in particular have been adapted to resemble the Coulomb barrier for electron/hole separation in these kind of materials, see also reference [159] and stem from an explicit calculation of the barrier. In contrast, the Coulomb barrier for the CS states has been constructed from a simple model employing two charged point-like objects with distance r_{ij} and a dielectric constant $\epsilon_r = 3.5$ representative of P3HT (see previous chapter). The fourth and fifth term in equation 10.2 represent the excitonic nearest neighbor coupling as well as the XT-CS coupling, respectively. Next, t describes the transfer integrals that couple heteronuclear charge separated states. The terms $K1$ and $K2$ in equation 10.2 describe the homomolecular exciton dissociation in terms of electron or hole transfer to a neighboring P3HT molecule, respectively. The coupling K in the ninth term of equation 10.2 describes the coupling between the homomolecular CS and the hetermolecular CT state. Finally, the last two terms in equation 10.2 describe the electron and hole transfer within the homomolecular CS state manifold, respectively.

The phonon part of the Hamiltonian is similar to the phonon part shown in the previous section. Again, a linear vibronic coupling model has been assumed, in combination with the previously introduced effective mode approach,

$$\hat{H}_{el-ph} = \sum_{i}^{8} \left(\frac{1}{2}\Omega_i \left(\hat{P}_i^2 + \hat{Q}_i^2 \right) + \sum_{n}^{13} c_{i,n} |XT_n\rangle \langle XT_n| + \sum_{n} c_{i,n} |CT\rangle \langle CT| + \sum c_{i,n} |CS\rangle \langle CS| \right) \tag{10.3}$$

As it has been pointed out earlier, each fragment shown in figure 10.1 has a total of eight degrees of freedom associated with each state, as can be seen from equation 10.3. This leads to a total of 112 degrees of freedom. The number of electronic states has been varied, ranging from a total of 26 electronic states when omitting the CS state manifold, to 27 states when including a single CS state at the interface or to 50 electronic states, where the complete $CS_{n,n\pm1}$ manifold has been included. Furthermore, even simulations with the complete CS state manifold have been done, employing a total of 182 electronic state and 112 degrees of freedom.

10.2 Electronic Structure Calculations

To parametrise the model Hamiltonian introduced in the previous section, several electronic structure calculations had to be carried out. On the one hand, electronic structure calculations were performed to parametrise the electronic part of the Hamiltonian, i.e. equation 10.2. On the other hand, the phonon part of the Hamiltonian in equation 10.3 had to be parametrised. In order to accomplish this, the effective mode approach as outlined in the previous section has been used, employing the third scheme with a truncated Mori chain and a residual bath, see also figure 7.3c. To obtain the effective mode parameters, the normal mode displacements as well as the excited state gradients had to be calculated. From these data, the effective modes can be constructed as outlined in references [125, 176]. Since the studies carried out in this chapter employ a reference Hamiltonian from reference [132], only the differences with respect to the original Hamiltonian will be introduced, notably the diabatic couplings between the XT state and the homomolecular CS states as well as between the homomolecular CS states and the heteromolecular CT states along with the excitation energies to the CS states. Here, the diabatic couplings between homomolecular CS states correspond to the results discussed in the preceding section.

Figure 10.2 shows a sketch of the calculation setup as well as the resulting coupling and excitation energies. Further, the relevant configurations of the system are shown with their molecular orbital configurations. The matrix underneath shows (i) on the diagonal, the respective excitation energy and (ii) as off-diagonal entries, the diabatic coupling to the respective state. As in the case of homomolecular CT state formation in RR-P3HT in the previous section, one can see that the diabatic coupling between the XT states to the homomolecular CS states is very large. In particular, the diabatic coupling describing

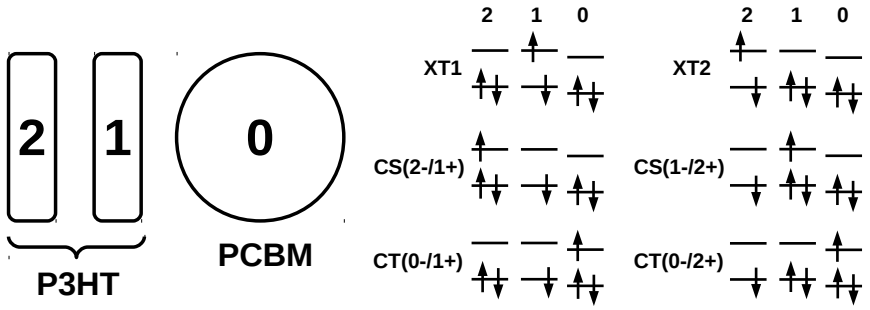

	XT1	XT2	CS(2-/1+)	CS(1-/2+)	CT(0-/1+)	CT(0-/2+)
XT1	0.100	0.100	0.357	0.139	0.119	0.007
XT2		0.100	0.139	0.357	0.014	0.013
CS(2-/1+)			0.722	0.001	0.005	0.002
CS(1-/2+)				0.533	0.019	0.165
CT(0-/1+)					0.000	0.102
CT(0-/2+)						0.140

Figure 10.2: Sketch of the investigated model system as well as the molecular orbital configurations of the electronically excited states under investigation. The table at the bottom shows on the diagonal the on-site energies and on the off-diagonal the diabatic electronic couplings between the respective states.

electron transfer is $\frac{1}{2}$ of the energy spacing between the XT and corresponding CS state. Furthermore, one observes a significant XT to $CT_{0,1}$ coupling. The diabatic XT2 state couples to the homomolecular CS state manifold as well as to the heteromolecular $CT_{0,1}$ and $CT_{0,2}$ state. One can also see that the homomolecular $CS_{1,2}$ state, where the electron is located on the P3HT/PCBM interface, exhibits a large coupling to the heteromolecular $CT_{0,2}$ state. This leads to the conclusion that spatially extended $CT_{0,i}$ states can be directly populated from the $CS_{j,i}$ manifold, which is a mechanism that was not included in the previous study published in [132]. The transfer integrals for the hole transport between $CT_{0,1}$ and $CT_{0,2}$ are also fairly large and on the same order of magnitude as the energy gap between both states, indicating an efficient hole transport along the stacking direction. From this analysis, it is clear that additional charge separation pathways are available due to the participation of the homomolecular CS states.

Three different simulation protocols with a varying number of electronic states were implemented. For the simulation that employed the total $CS_{i,j}$ state manifold, a Coulomb barrier for the homomolecular CS states was introduced as follows,

$$E_{\mu\nu}^{CS} = e_0 - \frac{1}{4\pi\epsilon_0\epsilon_r r_{\mu\nu}} \tag{10.4}$$

similarly to [113] and various other studies. Here, e_0 is the exciton binding energy and is chosen such that $E_{\mu=i,\nu=i} = 0$ for a XT state configuration, and $r_{\mu\nu}$ describes the distance between electron and hole within the homomolecular CS state manifold. In addition to the homomolecular CS Coulomb barrier, which is only relevant for the simulation with the complete CS state manifold, a Coulomb barrier for the heteromolecular CT state manifold is present in all simulations. This barrier has been calculated explicitly with *ab initio* methods, as discussed in reference [132].

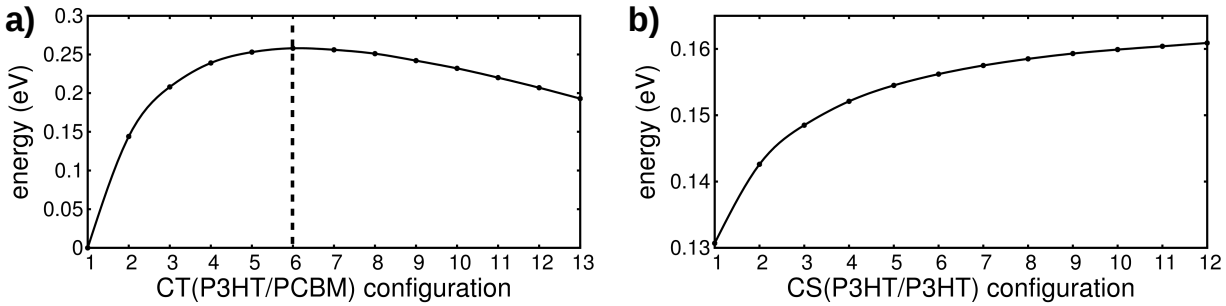

Figure 10.3: Coulomb barriers used for the quantum dynamics simulations. a) Coulomb barrier between the P3HT and PCBM molecules. b) Coulomb barrier within the RR-P3HT stack. The barrier has been obtained using equation 10.4 with $\epsilon_r = 4$.

Figures 10.3a and b show the calculated Coulomb barriers for the heteromolecular CT states and for the homomolecular CS state manifold, respectively. In figure 10.3a, the x-axis shows the respective $CT_{0,i}$ configuration, with i labeling the different P3HT monomers, see also figure 10.1. At the beginning of the Coulomb barrier, a steep increase of the energy of the respective $CT_{0,i}$ configuraton can be seen. If the electron-hole separation corresponds to a distance of four monomer units, the barrier begins to get shallower. After the electron-hole distance reaches a distance of six monomer units, the maximum of the energetic barrier is reached and the energy decreases again. CT configurations corresponding to a $CT_{0,i}$ with $i > 6$ correspond to so called free charge carrier configurations, which is also indicated by the vertical dashed line.

The Coulomb barrier for the homomolecular CS state manifold has been calculated with the aid of equation 10.4. Here, the x-axis corresponds to the $CS_{1,i+1}$ configuration, i.e. $i = 1$ corresponds to a $CS_{1,2}$ configuration. In contrast to the Coulomb barrier presented in figure 10.3a, the energy rises continously, which is due to the neglect of an external electric field, differently from the calculations for the heteromolecular Coulomb barrier.

10.3 Quantum Dynamics Simulations

Quantum dynamical simulations have been carried out with three different simulation setups:

- First, only a single $CS_{1,2}$ state configuration at the P3HT/PCBM interface has been employed, which is coupled directly to the $CT_{0,2}$ state, leading to a total of 27 electronic states.
- Second, a CS manifold with an electron-hole distance of one monomer unit has been included. This leads to a total of 50 electronic states.
- Finally, the complete CS state manifold with all possible configurations has been employed, yielding a total of 182 electronic states.

All simulation setups featured a total of 13 P3HT monomers as electron donating material and a single PCBM monomer as an electron accepting material. The total number of degrees of freedom is 112 for all three simulation setups. With respect to the initial conditions, three different cases for all simulation setups have been investigated:

- First, the intitial XT wave packet has been placed on the P3HT-1 fragment, close to the P3HT/PCBM interface.
- Second, the XT wave packet has been placed on the P3HT-2 fragment.
- As a last initial condition, a delocalised wave packet prepared in the bright H-aggregated state has been used.

In the following, we discuss the results obtained for the three scenarios described above.

10.3.1 Single $CS_{1,2}$ State

The simulations employing a single $CS_{1,2}$ state at the P3HT/PCBM interface feature a total of 27 electronic states. Of these 27 electronic states, 13 belong to the P3HT XT manifold, 13 belong to the $CT_{0,i}$ manifold and the remaining electronic configuration belongs to the $CS_{1,2}$ state. The adiabatic energy of the $CS_{1,2}$ state has been scaled by factor of four, which resembles typical values for the dielectric constant ϵ_r found in organic photovoltaic devices.

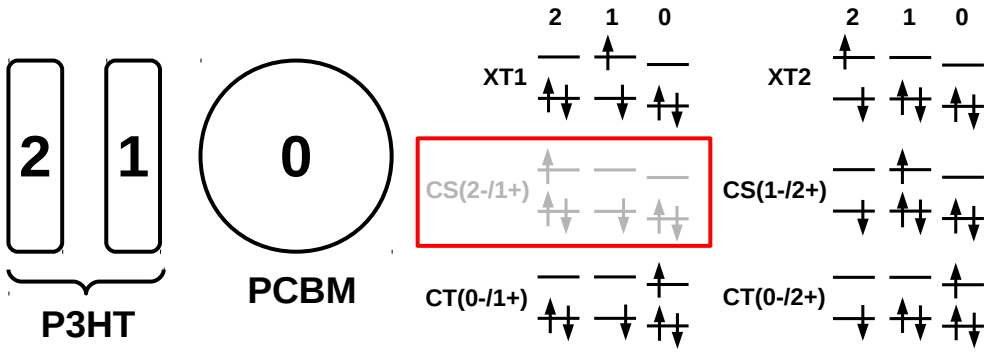

	XT1	XT2	CS(1-/2+)	CT(0-/1+)	CT(0-/2+)
XT1	0.100	0.100	0.139	0.119	0.007
XT2		0.100	0.357	0.014	0.013
CS(1-/2+)			0.133	0.019	0.165
CT(0-/1+)				0.000	0.102
CT(0-/2+)					0.140

Figure 10.4: Sketch of the model system as well as the molecular orbital configurations of the states used for the quantum dynamics simulations. The $CS_{2,1}$ state has been omitted from the dynamical treatment. The table at the bottom shows the relevant diagonal on-site energies as well as the diabatic couplings.

Figure 10.4 sums up the simulation setup for the interfacial area between P3HT and PCBM. As compared to the electronic structure analysis of figure 10.2, the $CS_{1,2}$ state configuration has now been neglected. Since the $CS_{1,2}$ state is not able to couple to the $CT_{0,2}$ state directly, its presence can be seen as a loss process for the overall CT state population. Hence, this state has been omitted from the investigation in the present simulation set up.

For the quantum dynamical simulations, different initially localised states have been used. First, a localised excitation has been placed at the P3HT/PCBM interface, i.e. the initial excitation is located on the P3HT-1 fragment. Complementary to this simulation, a localised excitation has been placed on the P3HT-2 fragment. From figure 10.4 it is obvious that both the XT1 and XT2 state can lead to a heteromolecular $CT_{0,i}$ state configuration. Finally, a delocalised excitation representing an H-type aggregate wave function has been used.

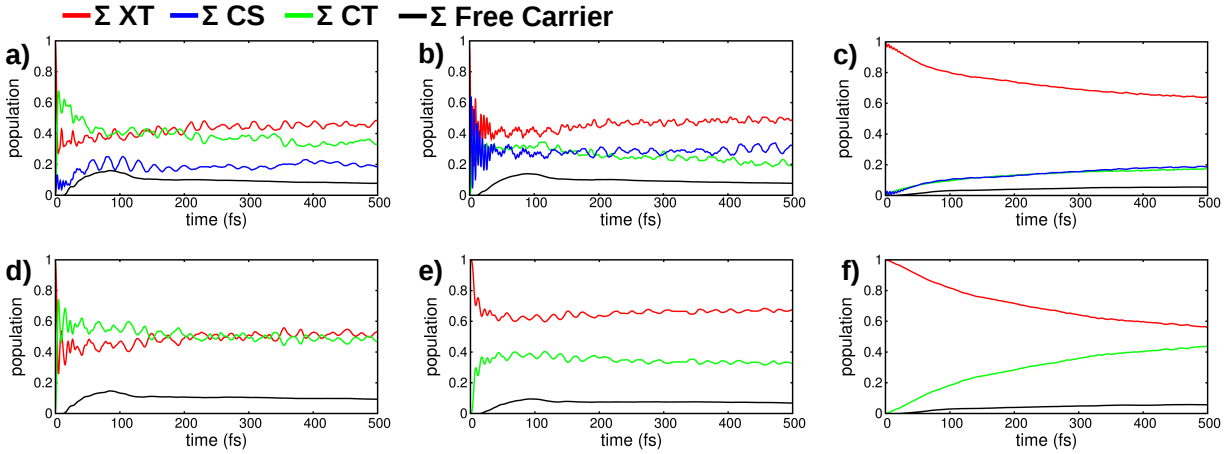

Figure 10.5: Electronic populations of the different states under investigation. a-c show the populations of a simulation with a singe P3HT/P3HT $CS_{1,2}$ state, whereas d-f show the results from a simulation without the P3HT/P3HT $CS_{1,2}$ state. a and d: Initial condition localised on P3HT-1. b and e: Initial condition localised on P3HT-2. c and f: Initial condition prepared in the bright delocalised state.

Figures 10.5a-f show the time-dependent populations for the simulation employing homomolecular CS states (a-c) and in the absence of homomolecular CS states (d-f). By comparing figures 10.5a and d one can see that the introduction of the homomolecular $CS_{1,2}$ state does not significantly affect the generation of free charge carriers. The overall population of the XT and heteromolecular $CT_{0,i}$ states is also lower than for the simulation without the homomolecular CS state. A more interesting result is obtained for the initial condition placed on the P3HT-2 fragment, shown in figures 10.5b and e. In contrast to the results shown in figures 10.5a and d, one can see a strong coherent transfer between the XT and homomolecular CS state, emphasized by the fast oscillations during the first 50 femtoseconds. Afterwards, a slower oscillatory pattern with a frequency of about 23 femtoseconds is visible. This slower oscillatory signal can also be seen in the simulation

employing a localised initial condition on the P3HT-1 fragment. More interesting is the increase in population of the free charge carriers by about 50 %. For the simulation employing a delocalised H-aggregate wave function, the population dynamics with the inclusion of a single CS state do not change in comparison with the population dynamics of the simulation in the absence of a single interfacial CS state, see figures 10.5c and f.

The following comparison highlights the free charge carrier populations as well as the population of the interfacial $CT_{0,1}$ state between simulations with and without a P3HT/P3HT $CS_{1,2}$ state.

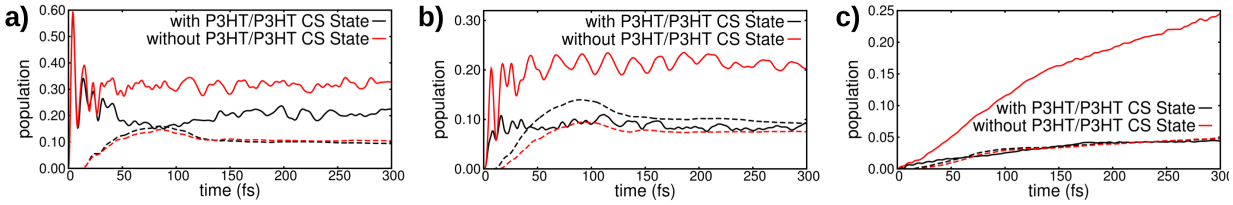

Figure 10.6: Comparison between the population of the interfacial P3HT/PCBM $CT_{0,1}$ state as well as the free charge carriers between a simulation with and without a P3HT/P3HT $CS_{1,2}$ state. Solid lines represent the $CT_{0,1}$ state, dashed lines represent the free charge carriers. a) Localised initial condition on P3HT-1. b) Localised initial condition on P3HT-2. c) Delocalised initial condition.

Here, figure 10.6a shows the initial XT state localised on the P3HT-1 fragment. While the free carrier population, represented by the dashed lines, does not change much upon introduction of the P3HT/P3HT $CS_{1,2}$ state, the population dynamics of the interfacial $CT_{0,1}$ state changes much more. During the first 50 femtoseconds, the rise in population is equal for both simulations performed, i.e. with and without the P3HT/P3HT $CS_{1,2}$ state. While the population of the simulation without the P3HT/P3HT CS state reaches a stationary population with only minor fluctuations, the population dynamics for the simulation with the inclusion of a P3HT/P3HT CS state are different. Here, the population of the interfacial $CT_{0,1}$ state decreases after approximately 50 femtoseconds and oscillates around this stationary value.

The results from the simulation with the XT initial condition localised on the P3HT-2 fragment are shown in figure 10.6b. The free carrier populations shown with dashed lines show a higher population for the simulation employing a P3HT/P3HT $CS_{1,2}$ state at the interface. More dramatic is the change in the population of the interfacial P3HT/PCBM

$CT_{0,1}$ state. While for both simulations the $CT_{0,1}$ population reaches a stationary value after about 50 femtoseconds with only minor fluctuations, the population of the $CT_{0,1}$ state with a P3HT/P3HT $CS_{1,2}$ state is only half of the population without the additional $CS_{1,2}$ state.

In figure 10.6c, the results for a delocalised initial condition are shown. Again, the dashed line shows the free carrier population, which is fairly symmetric for both simulations performed. On the other hand, the population dynamics for the interfacial $CT_{0,1}$ state are very different. While the population of the P3HT/PCBM $CT_{0,1}$ state in the absence of a P3HT/P3HT $CS_{1,2}$ state increases monotonically during the time of the simulation, the $CT_{0,1}$ state in the presence of a $CS_{1,2}$ state shows a much lower population.

10.3.2 $CS_{i,i\pm1}$ State Manifold

For the simulation employing a homomolecular $CS_{i,i+1}$ and $CS_{i+1,i}$ state manifold, the same simulation setup has been used, i.e. 13 P3HT monomers act as an electron donating material and a single PCBM monomer acts as an electron acceptor. With the introduction of the $CS_{i,i+1}$ & $CS_{i+1,i}$ state manifold, the total number of electronic states rises from 27 to 50. Again, three different initial conditions have been used, with the initial wave function localised either on the P3HT-1 or the P3HT-2 fragment. Furthermore, a delocalised H-aggregate wave function has been used. With respect to the diabatic electronic couplings, the scheme provided in figure 10.2 has been used as a guideline for the electronic couplings.

Figures 10.7a-f show the diabatic populations obtained for the simulation in the presence of a homomolecular CS state manifold (a-c) and in the absence of the CS state manifold (d-f). Due to the computational demanding nature of the simulation setup, only 300 femtoseconds have been propagated, as opposed to 500 femtoseconds for the previous simulation setup. For all three initial conditions shown in figures 10.7a-c one can see that the dynamics reaches a stationary state after approximately 100 femtoseconds and only small fluctuations can be seen in the populations. Interestingly, the time scale of the low frequency oscillations on top of the homomolecular CS state and XT state populations is the same as for the investigations of the intrastack CT state formation in the previous chapter. These oscillations are present for all three initial conditions under investigation. Further, one can see a very fast component during the first 30 femtoseconds of the sim-

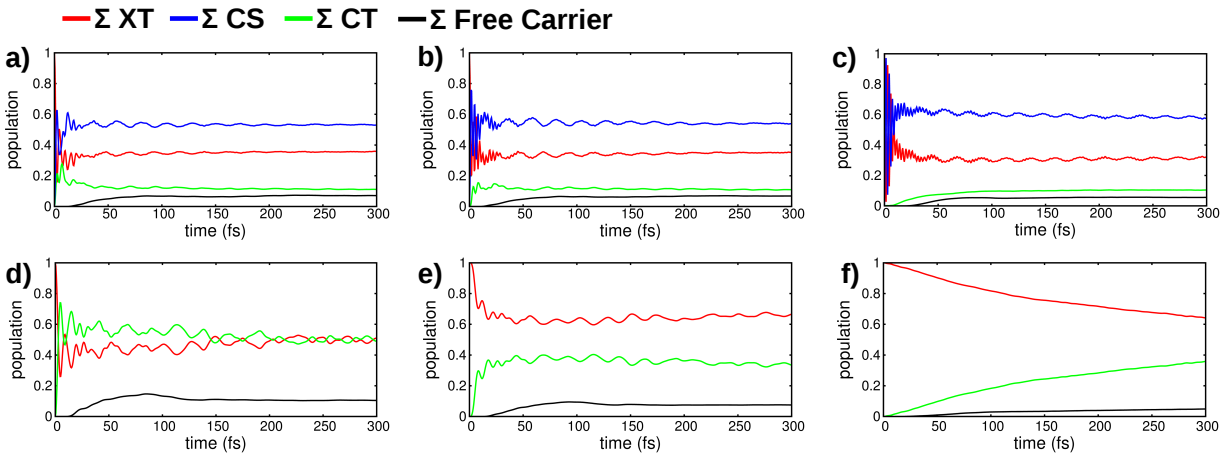

Figure 10.7: Electronic populations of the different states under investigation. a-c show the populations of a simulation with homomolecular P3HT/P3HT CS states, whereas d-f show the results from a simulation without P3HT/P3HT CS states. a and d: Initial condition localised on P3HT-1. b and e: Initial condition localised on P3HT-2. c and f: Initial condition prepared in the bright delocalised state.

ulation, which is responsible for the ultrafast transfer from the XT state manifold to the homomolecular P3HT/P3HT CS state manifold. Comparing the amount of generated free charge carriers for the simulation employing a homomolecular CS state manifold (i.e. figures 10.7a-c) to the simulation without a CS state manifold (i.e. 10.7d-f), one can see for the localised initial conditions on fragment P3HT-1 and P3HT-2 that the amount of free carriers is less for the simulations with a CS state manifold than without a CS state manifold. In contrast, the simulation employing a delocalised H-aggregate wave function shows the opposite dynamics.

Again, the free charge carriers as well as the population of the P3HT/PCBM interfacial $CT_{0,1}$ state with respect to the presence and absence of a P3HT/P3HT $CS_{1,2}$ state will be shown.

Figure 10.8a shows the results for a simulation with the initial condition localised on the P3HT-1 fragment. While the free charge carrier populations, shown with dashed lines, are nearly the same for long times, the dynamics of the $CT_{0,1}$ state are very different. For both simulation setups, i.e. with and without P3HT/P3HT $CS_{i,i+1}$ and $CS_{i+1,i}$ states, the P3HT/PCBM $CT_{0,1}$ state shows a strong increase during the first few femtoseconds of the simulation. In contrast to the simulation without P3HT/P3HT CS states, where a

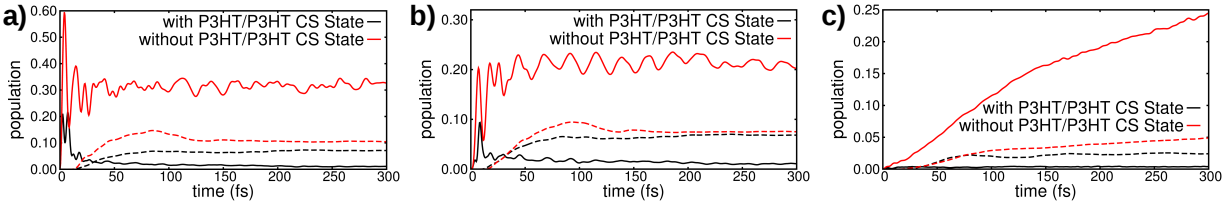

Figure 10.8: Comparison between the population of the interfacial P3HT/PCBM $CT_{0,1}$ state as well as the free charge carriers between a simulation with and without a P3HT/P3HT $CS_{i,i+1}$ and $CS_{i+1,i}$ state manifold. Solid lines represent the $CT_{0,1}$ state, dashed lines represent the free charge carriers. a) Localised initial condition on P3HT-1. b) Localised initial condition on P3HT-2. c) Delocalised initial condition.

steady state population of the $CT_{0,1}$ state after 50 femtoseconds is reached, the $CT_{0,1}$ state in the presence of P3HT/P3HT CS states decays from the initially high value to nearly zero.

For the simulation with the XT initial condition localised on the P3HT-2 fragment, the same observation as for the initial condition localised on the P3HT-1 fragment can be made. Again, the population of the free charge carriers approach the same steady state value for longer simulation times. Opposed to that, the interfacial P3HT/PCBM $CT_{0,1}$ state dynamics are very different. Most notable is the change in overall population for longer times, where the $CT_{0,1}$ state population in the presence of a $CS_{i,i\pm1}$ state manifold decays nearly completely for long simulation times. There is also a difference in the short time dynamics, where one can see that the population of the $CT_{0,1}$ state is delayed by a couple of femtoseconds, as compared to the simulation without the P3HT/P3HT $CS_{1,2}$ state.

The results for the simulation with a delocalised initial condition are shown in figure 10.8c. Interestingly, the presence of a P3HT/P3HT $CS_{i,i+1}$ and $CS_{i+1,i}$ manifold does not only influence the population dynamics of the interfacial $CT_{0,1}$ state, but that of the free charge carriers as well. While for the previous initial conditions the behaviour of the free charge carrier dynamics were fairly symmetric, this is not true for the delocalised initial condition. Here, one can see that the presence of the $CS_{i,i+1}$ and $CS_{i+1,i}$ state manifold leads to a faster creation of free charge carriers and also to a more steady population. In contrast, the free charge carrier populations in the absense of a $CS_{i,i+1}$ and $CS_{i+1,i}$ state manifold increases monotonically with the progression in simulation time. The population dynamics of the interfacial $CT_{0,1}$ state are very different again, with a steady increase of

population for the simulation without the $CS_{i,i+1}$ and $CS_{i+1,i}$ state manifold and a steady state of the $CT_{0,1}$ population in the presence of the $CS_{i,i+1}$ and $CS_{i+1,i}$ state manifold. Also the overall value of the P3HT/PCBM $CT_{0,1}$ state is very different.

10.3.3 Full $CS_{i,j}$ State Manifold

The simulations employing the full $CS_{i,j}$ state manifold contain a total of 182 electronic states in addition to the 112 degrees of freedom. The energetics of the homomolecular CS state configurations have been adapted to a simple Coulomb model, as in figure 10.3b. Due to the large number of configurations, only up to 200 femtoseconds have been propagated. As it could be seen from the previous simulations, 200 femtoseconds should be sufficient enough to account for the ultrafast exciton dissociation mechanism and hence, contain all relevant information about the quantum dynamics after photoexcitation. In the following, first the results for the different state configurations will be compared to the results without the homomolecular P3HT/P3HT CS state manifold. Then, the influence of the presence of the homomolecular P3HT/P3HT CS states on the dynamics of the free charge carriers and the interfacial P3HT/PCBM CT state will be investigated.

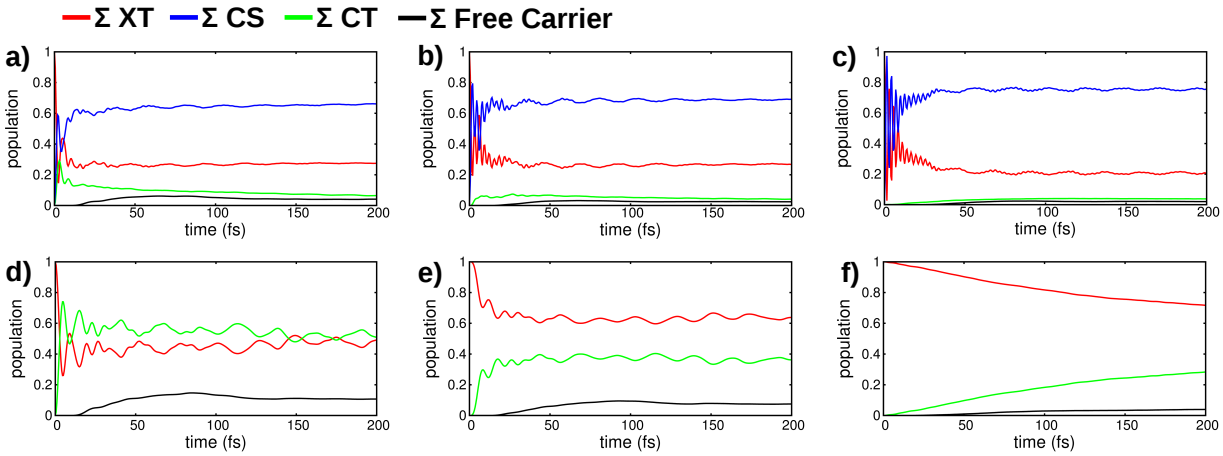

Figure 10.9: Electronic populations of the different states under investigation. a-c show the populations of a simulation with homomolecular P3HT/P3HT CS states, whereas d-f show the results from a simulation without P3HT/P3HT CS states. a and d: Initial condition localised on P3HT-1. b and e: Initial condition localised on P3HT-2. c and f: Initial condition prepared in the bright delocalised state.

Figure 10.9a-f show the diabatic electronic populations for simulations with the complete homomolecular P3HT/P3HT CS state manifold, i.e. 182 electronic states along with

112 phonon degrees of freedom in a harmonic approximation. Here, figures 10.9a-c show the results from the simulation in the presence of the P3HT/P3HT CS state manifold, whereas figures 10.9d-f show the same simulation protocol but in the absence of the P3HT/P3HT CS state manifold. As in the simulation of the P3HT/P3HT $CS_{i,i\pm1}$ state manifold, one can see a very fast and efficient transfer from the initial XT state manifold to the homomolecular P3HT/P3HT CS state manifold for all three initial conditions under investigation. While for the other simulation setups with either a P3HT/P3HT CS state located at the P3HT/PCBM interface or with a P3HT/P3HT $CS_{i,i\pm1}$ state manifold periodic oscillations were observable, these oscillations are still present, but have a much weaker amplitude. Considering the fact that even more state crossings are present for the current simulation etup than for the other simulation setups, this behaviour seems to be plausible. Further, one can see that the amount of P3HT/PCBM charge transfer is comparable for all three initial conditions. Also, as in the simulation employing a P3HT/P3HT $CS_{i,i\pm1}$ state manifold, one can see very fast oscillations during the first few femtoseconds of the simulation, which vanish completely after approx. 30 femtoseconds. Since after these 30 femtoseconds no more changes in the population between XT and P3HT/P3HT CS states occur, it can be stated that the fast oscillatory signal stems from the XT to CS state transfer.

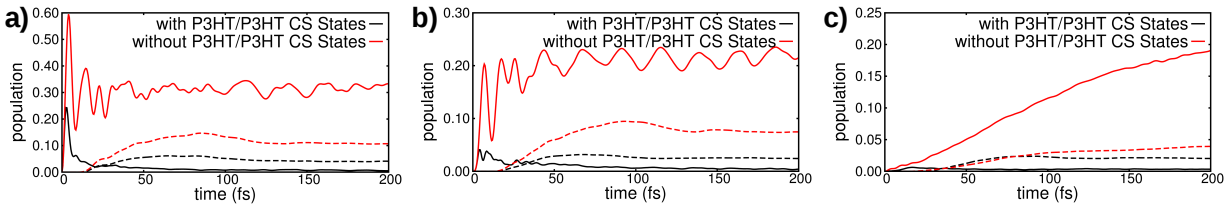

Figure 10.10: Comparison between the population of the interfacial P3HT/PCBM $CT_{0,1}$ state as well as the free charge carriers between a simulation with and without a P3HT/P3HT $CS_{i,j}$ state manifold. Solid lines represent the $CT_{0,1}$ state, dashed lines represent the free charge carriers. a) Localised initial condition on P3HT-1. b) Localised initial condition on P3HT-2. c) Delocalised initial condition.

Figures 10.10a-c show the population of the free charge carriers and the interfacial P3HT/PCBM $CT_{0,1}$ state for simulations with and without the homomolecuar P3HT/P3HT CS state manifold for different initial conditions. For all three initial conditions investigated, one can see huge differences in the excited state behaviour with respect to the interfacial P3HT/PCBM $CT_{0,1}$ state. For the initial condition localised on the P3HT-1 fragment, shown in figure 10.10a, one can see a strong increase in population of the $CT_{0,1}$

state on a very fast timescale. While the population of this state is at approx. 0.3 for the simulation without the P3HT/P3HT CS state manifold, it decreases dramatically for the simulation with the P3HT/P3HT CS state manifold. The free charge carrier generation, shown with dashed lines in figure 10.10a is not as much affected by the presence of the CS state manifold.

The same behaviour for the initial condition localised on the P3HT-2 fragment, shown in figure 10.10b, as for the simulation with the initial condition localised on the P3HT-1 fragment can be observed. Again, one can see a very different dynamical behaviour of the population dynamics of the interfacial P3HT/PCBM $CT_{0,1}$ state. In contrast to the previously analysed population dynamics, the free charge carrier populations in this case are more affected due to the presence of the homomolecular P3HT/P3HT CS state manifold.

Finally, the population dynamics with a delocalised initial condition have been analysed as well, shown in figure 10.10c. As in the dynamics employing a P3HT/P3HT $CS_{i,i\pm1}$ state manifold in the previous section, the excited state dynamics upon photoexcitation are very different. While for the simulation without the P3HT/P3HT CS state manifold, the population of the interfacial $CT_{0,1}$ state increases steadily, the same charge transfer configuration remains nearly unpopulated for the simulation with the homomolecular P3HT/P3HT CS state manifold. Interestingly, the overall population of the free charge carriers are nearly identical as well. These results indicate that an alternative pathway of exciton dissociation is opened due to the presence of the CS states, besides the dissocation pathway at the donor/acceptor interface.

10.3.4 Summary and Conclusion

Building upon previous studies on the charge separation dynamics in P3HT/PCBM systems [131, 175], the model Hamiltonian of reference [131] has been augmented by the inclusion of mixed Frenkel/charge-transfer states in the regioregular donor phase, in line with the results of the previous section. To reduce the very large number of degrees of freedom in the system, an effective mode decomposition of the full normal mode representation, employing a truncated Mori chain representation, has been used. This leads to a reduction from 3N-6 normal modes to 8 effective modes per fragment, resulting in a total of 112 degrees of freedom and several electronic states for a system consisting of 13 P3HT

and a single PCBM monomer.

Electronic structure calculations have been performed with a model system consisting of two P3HT monomers and a single PCBM "super-site". The analysis of the diabatic electronic couplings and the on-site energies of the different states, i.e. XT states located on P3HT, CS states between two P3HT monomers, and CT states between P3HT and PCBM units, indicate an efficient charge separation process of the XT wave function into either the CS or CT states. Furthermore a non-negligible electronic coupling between the CS and CT states is observed.

Employing quantum dynamical simulations based on the ML-MCTDH method, we have addressed three different dynamical scenarios: First, a P3HT/P3HT CS state has been allowed only at the interface, which couples subsequently to the P3HT/PCBM CT state. Second, a manifold of CS states has been included in the model Hamiltonian, with the constraint that the electron hole separation distance within the CS manifold was only allowed for nearest neighbors. The third model system consists of the full homomolecular P3HT/P3HT CS state manifold, where the energetics of the CS state manifold have been modeled according to a simple Coulomb type description. This results in a total of 27 electronic states for the first model, i.e. 13 XT states, 13 P3HT/PCBM CT states and one P3HT/P3HT CS state, 50 electronic states for the second model and 182 electronic configurations for the third model.

From the results of the quantum dynamical simulations it is clear that the P3HT/P3HT CS states strongly influence the interfacial P3HT/PCBM CT state formation, and reduce the participation of the interfacial CT state. The free charge carrier populations is affected to a lesser extent - but clearly in such a way that the presence of the CS states leads to a reduction of te free carrier yield. With the current parametrization, it therefore turns out that the CS states act as an effective trap, even though more exciton dissociation channels are available.

In summary, it turns out that the inclusion of homomolecular P3HT/P3HT CS states leads to additional, competing charge separation pathways in functional BHJ nanomaterials. While the first results presented in this thesis seem to be promising in terms of the overall understanding of free charge carrier generation, there are still open issues. In par-

ticular, it is not yet clear under which circumstances an increase of free carrier generation would be expected. One should point out that the current model Hamiltonian does not include microelectrostatic effects, neither does it treat the surrounding environment via an explicit or implicit type of description. Furthermore, real world photovoltaic devices use an applied external electric field, enhancing exciton dissociation and the transport of electrons and holes towards their respective electrode. Nevertheless, the present study makes first steps towards a realistic quantum dynamical study of the charge carrier generation including the effect of charge transfer excitons in the donor phase.

Part III

Kinetic Monte Carlo Modeling of Exciton and Charge Carrier Dynamics

The studies of exciton migration and charge transfer presented in the previous chapters have been performed employing a deterministic quantum dynamical approach. As has been pointed out in part **I** of this thesis, this is a highly accurate methodology, which is, however, only suitable for short length and time scales. In order to obtain an overall understanding of the processes of a given material after photoexcitation, not only the short time dynamics are important, but also the long time dynamical behaviour. After the characteristic quantum effects induced by photoexcitation – i.e., coherent wavepacket motion, vibronically hot states, multiple nonadiabatic crossings – are over, a long time thermodynamically and kinetically driven dynamics sets in that can largely be treated by classical-statistical methods. In this context, one obtains macroscopic observables such as charge density distributions and charge carrier mobilites, which can be directly compared to experimental results. Especially the Kinetic Monte Carlo (KMC) method has been successfully applied to study a variety of nanoscaled systems used for photovoltaic devices [178–181]. This is, therefore, the method of choice for the studies reported in this chapter.

This study prepares the ground for an in-depth analysis of a second-generation donor-acceptor system devised by the Strasbourg group, which has been introduced in section 8.5. In this system, charge separation occurs on a time scale of tens to hundreds of picoseconds, such that a quantum dynamical treatment is not appropriate. Preliminary results for the carrier dynamics in this system will be reported below.

The remainder of the chapter is divided as follows. First, the KMC program that has been written in the frmework of this thesis will be introduced. Then, the calculation of rates will be explained, connecting to the first part of this thesis. Finally, the results obtained from the KMC method will be presented.

11 — Program Overview

The theoretical methodology and the algorithm employed to solve the Master Equation has already been presented in the first part of this thesis. Here, we outline the implementation of the KMC method into an efficient Fortran90 code, along with the principal workflow and steps of the program.

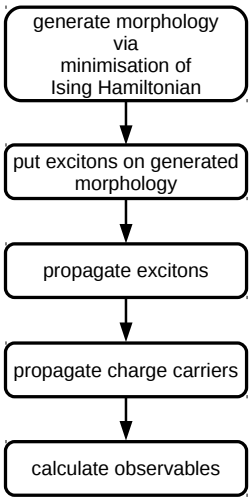

Figure 11.1: Overview and necessary prerequisites to perform simulations with the Kinetic Monte Carlo code.

Figure 11.1 shows a graphical overview over the most important steps in the KMC simulation. A suitable morphology has been generated with the Ising Hamiltonian, following reference [139]. To briefly summarize the generation of the morphology:

1. A random distribution of donors and acceptors is generated, and each of these sites has an energy ϵ associated to it.

2. Sites are switched to minimize the energy of the overall system, which is done by successively switching sites depending on the number of neighboring monomers and calculating the corresponding energy, i.e.

$$\Delta\epsilon = -\Delta N_1 J - \Delta N_2 \frac{J}{\sqrt{2}}. \tag{11.1}$$

Here, ΔN_1 and ΔN_2 account for the change of the numbers of first nearest neighbor and second nearest neighbor bonds, respectively. J is the interaction energy and controls whether interactions between identical monomers or between different monomers are benficial. Thus, the choice of J leads either to phase separation or phase aggregation, as demonstrated in the following example. The generated morphology can then be used for subsequent KMC simulations.

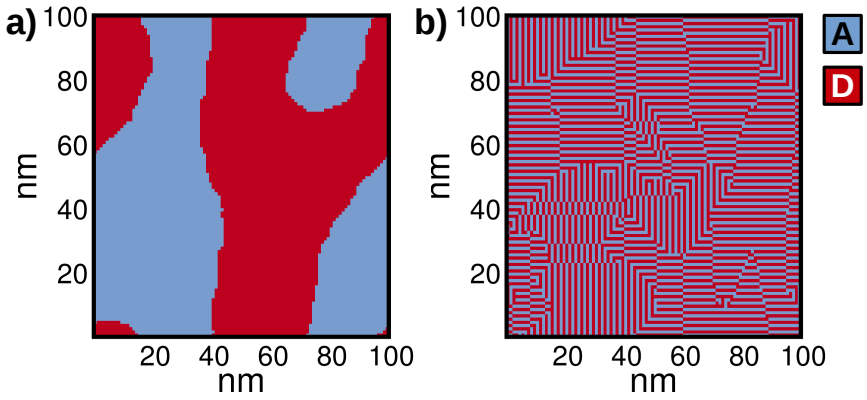

Figure 11.2: Morphologies obtained from energy minimisation of the Ising Hamiltonian. a) Phase aggregated morphology. b) Phase mixed morphology.

Figures 11.2a and b show two different morphologies obtained from energy mimization of the Ising Hamiltonian. Figure 11.2a has been obtained with a positive interaction energy J and resembles typical BHJ nano morphologies. Here, one has large domain sizes of either electron donating (red) or electron accepting (blue) material. For a negative value of the interaction energy J, a mostly phase mixed structure is being obtained, as it can be seen from figure 11.2b. Again, red marks the electron donating material while blue represents the electron accepting material. It is obvious that due to the phase separation of the different materials, one obtains a very large interfacial area.

The generated morphologies can then be used to propagate excitons and charge carriers via the KMC approach. Excitons are generated at random sites within the electron donating material and can propagate without an external force freely within the respective material. The timescale of the individual hops depends on the resonant energy tansfer (RET) rate, see the discussion given in the first part of this thesis. In particular, the rate expression looks as follows:

$$k_{RET} = k_0 \left(\frac{R_0}{r_{ij}} \right)^6 f_1 \left(\Delta E_{ij} \right) \tag{11.2}$$

with

$$f_1(\Delta E_{ij}) = \begin{cases} exp(-\frac{\Delta E_{ij}}{kT}) & \Delta E_{ij} > 0 \\ 1 & \Delta E_{ij} \leq 0 \end{cases} \tag{11.3}$$

Equation 11.2 is comparable to the standard FRET rate introduced in the first part of this thesis. Here, k_0 is the exciton hopping coefficient and can be interpreted as the inverse exciton lifetime [110, 173]. R_0 is the lattice spacing and r_{ij} is the distance between sites. The last term $f_1 \left(\Delta E_{ij} \right)$ stems from the Metropolis ansatz [182] which determines whether a Boltzmann factor is included in the calculation or not, depending on the energy difference of the initial and final site. In the following simulations, all site energies are subjected to random fluctuations caused by a Gaussian energy distribution. The parameters for the width of the energy distributions, i.e. $\sigma_{D/A}$, have been taken from experiments in reference [68] and are summarized in the following table.

Table 11.1: Parameters used for the calculation of the RET rates.

k_0	σ_D	σ_A	E_D	E_A
2 ps^{-1}	75 meV	65 meV	3.75 eV	3.25 eV

If the exciton reaches the donor-acceptor interface, exciton dissociation is switched on, besides the possibility of a RET step from the donor to the acceptor material. The rate for exciton dissociation is based on Miller-Abrahams theory [183].

$$k_{ex-diss} = k_0 e^{(-2\gamma r_{ij})} f_1 \left(\Delta E_{ij} \right) \tag{11.4}$$

Again, k_0 is the exciton dissociation coefficient. In the following simulations, k_0 is set to $10^{15}s^{-1}$ in order to highly favor the exciton dissociation in comparison to the RET process. γ is the inverse exciton localisation parameter [110], r_{ij} is the distance between sites and $f_1(\Delta E_{ij})$ is the same function as defined in equation 11.3. While the difference in energy for the RET process was just based on the difference in site energies, the change in energy for exciton dissociation depends on multiple parameters.

$$\Delta E_{ij} = E_{LUMO_{D,i}} - E_{LUMO_{A,j}} + E_B - E_{GP}(r_{ij}) + Fy \tag{11.5}$$

In equation 11.5, the first and second term are the energies of the HOMO and LUMO energy levels of the donor and acceptor, respectively, E_B is the exciton binding energy and has been taken from the optical gap of RR-P3HT, as experimentally determined in reference [184]. The last two terms are the geminate pair binding energy ($E_{GP}(r_{ij})$), which is a function of the site distance, and the energy gradient F, induced by the applied external electric field in the y direction of the material. The geminate pair binding energy is defined as follows,

$$E_{GP}(r_{ij}) = \frac{e^2}{4\pi\epsilon_r\epsilon_0 r_{ij}} \tag{11.6}$$

The geminate pair binding energy strongly depends on the relative dielectric constant of the material ϵ_r and the distance between sites r_{ij}. All relevant parameters are subsumed in the following table.

Table 11.2: Parameters used for the calculation of the exciton dissociation rates.

k_0	γ	$E_{LUMO,D}$	$E_{LUMO,A}$	E_B	ϵ_r
10^{15} s^{-1}	1 nm^{-1}	-2.68 eV	-4.20 eV	0.7 eV	3

If the exciton dissociates at the donor-acceptor interface, the charge carrier transport rates have to be evaluated. In the present thesis, charge carrier transport is based on Marcus-Levich-Jortner (MLJ) rates. (In other publications on KMC simulations for pho-

tovoltaic devices, the Miller-Abrahams rate has also been successfully applied to study charge carrier dynamics [68, 110, 111]). The MLJ rate reads as follows,

$$k_{MLJ} = \frac{2\pi}{\hbar}\frac{|V_{ij}|^2}{\sqrt{4\pi k_B T \lambda_s}}\sum_{N=0}^{\infty}\frac{(\frac{\lambda_i}{\hbar\omega})^N}{N!}exp\left(-\frac{\lambda_i}{\hbar\omega}\right)exp\left(-\frac{(\Delta E_{ij}+\lambda_S+N\hbar\omega_{intra})^2}{4\lambda_S k_B T}\right) \quad (11.7)$$

Equation 11.7 shows the rate equation for charge carrier transport with the MLJ rate equation (see also figure 3.7c). Here, V_{ij} is the transfer integral, λ_i and λ_S are the internal and environment reorganisation energy, respectively. The internal reorganisation energies λ_i for electron and hole transfer have been calculated according to the scheme provided in reference [185], whereas the environmental reorganisation energy is difficult to calculate [186, 187]. Thus, the environmental reorganisation energy has been approximated to be smaller than the internal reorganisation energy. The term $\hbar\omega$ corresponds to the vibrational quantum of a generalised intramolecular coordinate – treated within a harmonic approximation – and is taken to be 0.2 eV.

The difference in energy ΔE_{ij} does not depend soleley on the LUMO and HOMO energy levels for electron and hole transfer, respectively, but also on the external electric and field and the Coulombic energy created by the remaining charge carriers in the system,

$$\Delta E_{ij} = E_j - E_i + E_{Field} + E_{Coulomb} \quad (11.8)$$

Depending on the direction in which the charge carrier, i.e. electron or hole, is hopping, the E_{Field} term can be either positive or negative. If one of the charge carriers in the system reaches an electrode, it will get extracted immedately and the simulation is stopped. Finally, the charge carrier mobility of the respective particle is evaluated as shown in equation 6.28. The final parameters used for the calculation of the Marcus-Levich-Jortner rates are shown in the following table.

Table 11.3: Parameters used for the calculation of the Marcus-Levich-Jortner rates.

V_e	V_h	λ_e	λ_h	λ_s	$\hbar\omega$
0.5 meV	13 meV	0.3 eV	0.4 eV	0.1 eV	0.2 eV

The final simulation setup for the propagation of exctions and charges then looks as follows.

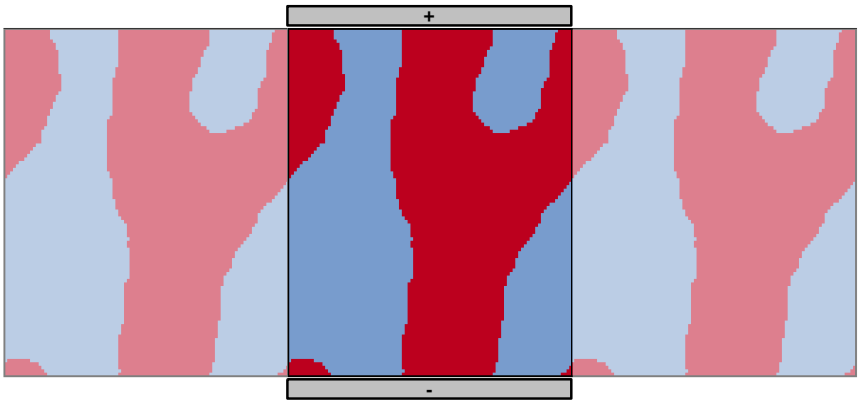

Figure 11.3: Simulation setup of the morphology for a Kinetic Monte Carlo trajectory with indicated electrodes and periodic boundary conditions.

Here, the central panel shows the generated morphology that is used for the KMC simulations. At the top and bottom are the electrodes, which are responsible for the externally applied field and for charge carrier collection. To each of the sides of the simulation box, periodic boundary conditions have been applied, which is illustrated by the transparent repetition of the morphology. This means that if a particle leaves the simulation box to one side, a particle with the same charge will enter the simulation box from the opposite side.

As an extension to typical KMC simulations, a mechanism leading to exciton delocalisation has been implemented. While typical KMC simulations do not treat delocalisation at all or only in a very crude fashion [110], an explicit mechanism for exciton delocalisation has been implemented into the KMC scheme. After the exciton has been localised on a single site, the adjacent sites are ordered by energy until a certain delocalisation length has been reached. The following delocalisation happens into the direction of the smallest energy barrier and is supposed to be instantaneous, i.e. it does not account for an advance in time t. Then, the rates for exciton migration or exciton dissociation are calculated and the fastest process will be executed, according to the KMC scheme. Pictorially, the process looks as follows

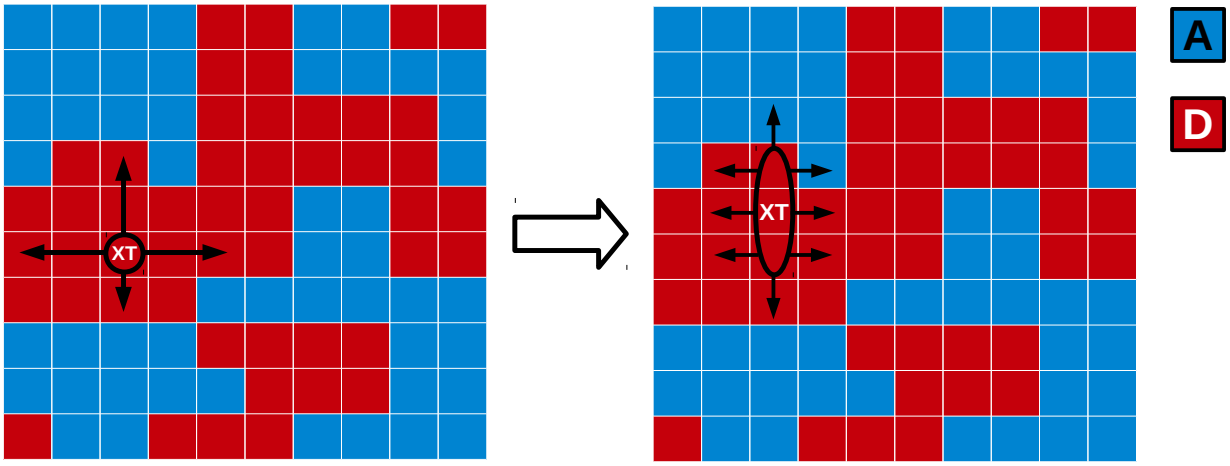

Figure 11.4: Sketch of the implemented delocalisation mechanism of an excitonic point-like object. The delocalisation does not have a favoured direction. Red corresponds to the Donor phase, blue corresponds to the acceptor phase.

Here, red corresponds to the electron donating material while blue corresponds to the electron accepting material. After an exciton has been created randomly on a electron donating site, it will instantaneously delocalise in the direction of the smallest energetic barrier. In the example, the delocalisation is fixed to a width of three sites. After the delocalisation, all possible processes will be evaluated and associated with its characteristic time scales. As one can see from figure 11.4b, the delocalisation leads to an increase in possible events.

12 — Results

In the following, the results obtained by our Kinetic Monte Carlo simulations will be presented. First, the macroscopic charge carrier mobilities for the electrons will be shown for three different idealised BHJ morphologies. Therefore, simulations employing an increasing number of charge carriers have been propagated according to the FRM algorithm. As soon as one of these charges has been extracted at the electrodes, the corresponding charge carrier mobility has been calculated and the simulation has been stopped. Afterwards, a new trajectory with the same number of charge carriers has been started in order to obtain reasonable statistics. For each generated idealised BHJ morphology, simulations have been performed with and without Coulombic forces between the particles. Simulations without the influence of the Coulombic forces can be seen as a simulation of an idealised electron gas.

After the discussion of the results employing the idealised BHJ structures, simulations for a randomly generated structure according to the Ising Hamiltonian will be presented. Here, two different morphological realisations of a mixed DA BHJ nanodevices will be presented. For one morphology, a maximal aggregation with distinct donor and acceptor domains was generated and for the second morphology a strongly mixed donor/acceptor system was generated. Again, simulations with and without Coulombic forces have been carried out, in addition to simulations featuring multiple charge carriers or a single charge carrier.

Finally, a coarse-graining approach to model the charge carrier dynamics in the second generation donor-acceptor system of the Strasbourg group, introduced in section 8.5, is detailed, along with the subsequent KMC dynamics for the generated structure. The coarse graining has been done based on an X-ray structure of the thin-film architecture of the second generation donor-acceptor system, as reported in references [36, 163].

12.1 Idealised BHJ Nanomorphologies

As pointed out earlier, idealised BHJ nanomorphologies have been created and used for subsequent KMC simulations. The simulations employ a varying number of charge carriers, ranging from as few as two particles to as many as 15. As soon as one of these particles has been extracted, the corresponding charge carrier mobility was calculated, the current simulation was stopped and a new simulation was initiated. This has been done in order to have the same number of particles for each simulation and for the corresponding calculation of the charge carrier mobility.

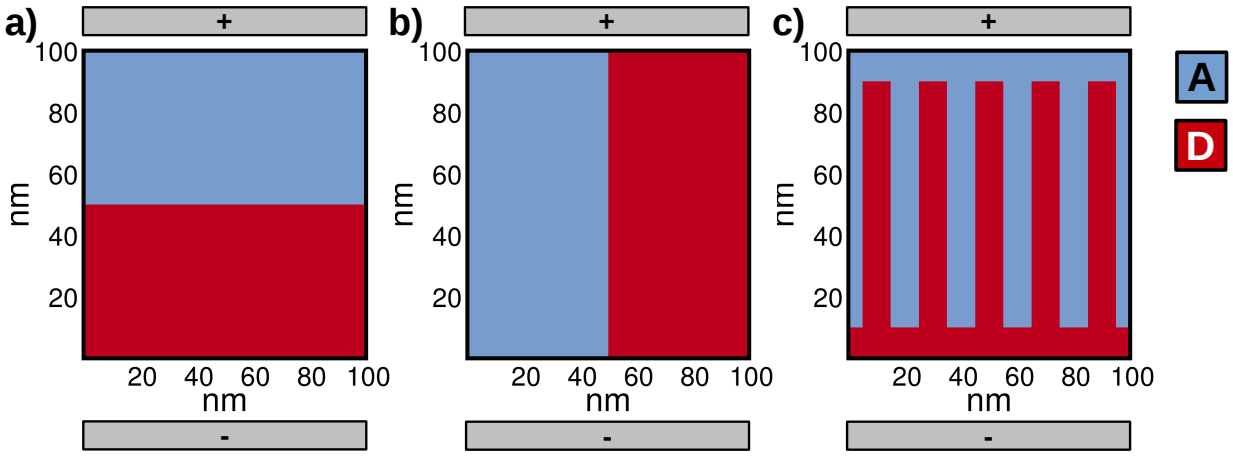

Figure 12.1: Idealised BHJ nanomorphologies used for the subsequent following Kinetic Monte Carlo simulations. a) Horizontally separated BHJ morphology. b) Vertically separated BHJ morphology. c) Columnwise phase separated BHJ morphology.

Figures 12.1a-c show the generated idealised BHJ nanomorphologies. In all three cases studied, the anode has been placed on top, while the cathode has been placed at the bottom. As soon as a charge carrier reached either the top or bottom of the device, the simulation was stopped. On the other hand, periodic boundary conditions have been applied to the left and right side of the device.

From the morphology presented in figure 12.1a it is obvious that all the generated charge carriers will have to travel the same distance to reach the anode or cathode, respectively. Therefore, in the absence of Coulombic forces, one can expect that the charge carrier mobility will have the same value independently of the number of charge carriers.

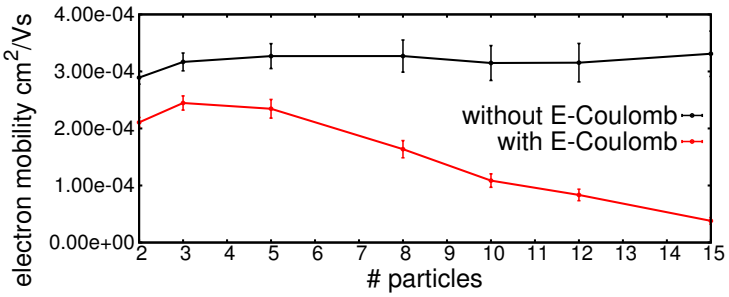

Figure 12.2: Electron mobility as a function of the number of particles for structure 12.1a.

Figure 12.2 compares the resulting charge carrier mobilities for a simulation employing the BHJ structure from figure 12.1a with and without Coulombic forces. For the simulation without Coulombic forces, one can see that the electron mobility adopts a constant value with some minor fluctutations.

For the simulation with Coulombic forces one can see that at first the electron mobility slightly increases, followed by a steady decrease. The steady decrease of the mobility can be explained by the fact that with an increase in the number of simulated particles, the charge carrier density also increases. Since the Coulombic forces acting on each particle increase with increasing charge carrier density, the particles will first start to drift away from each other, minimising the influence from the Coulombic repulsion. Therefore, it can happen that charges perform a hop to an energetically unfavourable site.

Next, the results employing the idealised BHJ structure from figure 12.1b will be shown.

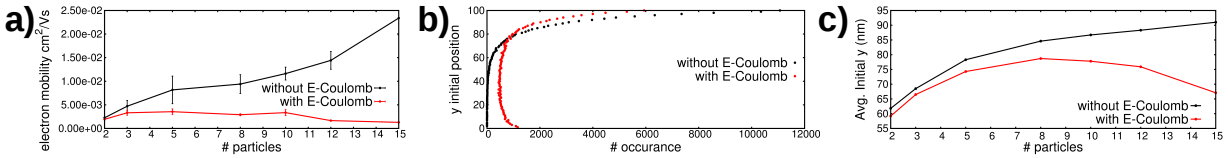

Figure 12.3: a) Electron mobility as a function of the number of particles for structure 12.1b. b) Initial position of the extracted charge carrier with and without Coulombic forces. c) Average starting position of the extracted charge carrier as a function of the number of particles.

Again, in figure 12.3a the results from a simulation employing Coulombic forces (with reference calculations without Coulombic forces) have been plotted. For the simulation

without Coulombic forces, the result is very different from the results shown in figure 12.2. Here, one can see a steady increase in electron mobility. The reason for this steady increase of the mobility is that the distribution of initial positions of the charge carriers along the y dimension of the morphology extends with increasing number of particles. Therefore, with an increasing number of particles it is more likely that the extracted charge carrier has to travel a short distance in a short amount of time, resulting in an increase of the charge carrier mobility.

For the simulation employing Coulomb repulsion between the charge carriers, one can see a slow but steady decrease of the electron mobility. The reason for this behaviour can be explained with the aid of figure 12.3b. Here, one can see the initial positions of the extracted charges for a simulation with 15 charge carriers and a total of 10^5 individual trajectories. Upon inclusion of the Coulomb repulsion, one can see that an increase of exctracted charges stems from the bottom region of the device. These charges experience a huge Coulombic repulsion. In order to avoid regions with a high repulsive potential, the charges will diffuse along the x axis towards a region with lower Coulomb repulsion, followed by a diffusion towards the electrodes. Since the calculated electron mobility is the average over all these single charge carrier mobilities, the effective charge carrier mobility will be lowered.

In figure 12.3c, the average initial position of the extracted charge carrier is shown as a function of the number of particles in the simulation. It is obvious that in the simulation without Coulombic forces, the average starting position of the extracted charge moves towards the anode with an increasing number of particles. On the other hand, when Coulombic forces are present, the average starting position starts to move more towards the anode, but at a certain charge carrier density, falls off again. This behavior can be explained by the diffusion of the extracted charge in a lateral direction, in order to avoid areas with high Coulombic forces.

Finally, the results for the idealised BHJ structure in figure 12.1c will be shown. Figure 12.4a shows the electron mobilities for a simulation with and without Coulombic forces between the charge carriers. It is obvious that both simulations give the same trend and behaviour of the charge carrier mobilities, unlike for the simulation of the other morphologies shown in figures 12.1a and b. The reason for the nearly same mobility values in both

simulations can be seen from figure 12.4b. Here, the distribution of the initial position of the extracted charge carrier is shown. Again, both simulations reveal nearly the same distribution of the initial positions of the extracted electrons. Therefore, one can say that due to the unique characteristic of the morphology shown in figure 12.1c, the particles behave nearly as an idealised electron gas. Due to the spatial separation of different blocks of donor and acceptor material, the particles can move without much influence from the other charges.

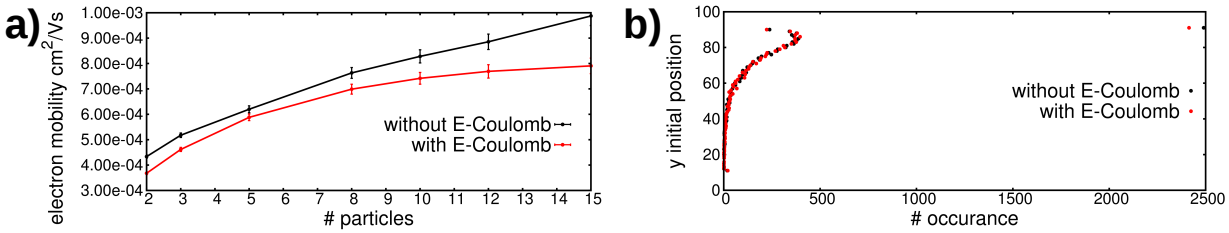

Figure 12.4: a) Electron mobility as a function of the number of particles for structure 12.1c. b) Initial position of the extracted charge carrier with and without Coulombic forces.

The following table compares the average initial starting position in the direction of the electrodes for the different morphologies. The results have been obtained from simulations employing 15 particles and 10^5 trajectories.

Table 12.1: Average initial position of the extracted charge for the different idealised morphologies under investigation. See also figures 12.1a-c.

Morphology	with E-Coulomb	without E-Coulomb
A	51	51
B	68	91
C	80	80

One can see that for the morphology shown in figure 12.1a and c, the average starting position of the extracted electron does not depend on the Coulombic forces. However, only the structure shown in figure 12.1c does show the same mobilities with and without Coulombic forces between the individual charge carriers. Due to the unique structure of the morphology, isolated domains of electron conducting material are obtained, in which the charge carriers can move nearly without any disturbances due to other charge carriers

in the system. The unique alignment also facilitates the transport of the electrons into the direction of the field and to the anode. This is not the case for structure 12.1a, where single columns of isolated electron or hole transport materials are not present. Here, the charge carriers can not be treated as isolated particles and hence, Coulombic forces influence the charge carrier mobilities. While for low charge carrier densities, the resulting mobiltiy is nearly the same for simulations with and without Coulombic forces, this is not true anymore for higher charge densities. The obtained electron mobilities for structure 12.1b is very much influenced by the number of charge carriers in the system. As it has been pointed out earlier, with an increase of charge carriers simulated, the average starting position of the extracted charge will shift to the bottom of the device. Then, the charge starts to drift laterally towards an area with lower Coulombic forces, followed up by a diffusion towards the anode.

12.2 Randomly Generated BHJ Nanomorphologies

In addition to the simulations carried out for idealised BHJ nanomorphologies in the previous section, calculations for randomly generated structures were performed as well. These structures should resemble a much more realistic picture of commonly used BHJ nanodevices and have been created via the previously introduced Ising Hamiltonian. This method has already been used succesfully in the generation of BHJ nanomorpologies for KMC simulations [111, 139]. However, there are also other methods in order to generate a suitable starting morphology, which are based on an improved Cahn-Hilliard diffusion equation formalism in conjunction with field theoretical methods [66, 188]. The remainder of the section is organised as follows. First, the results from a phase aggregated, randomly generated structure will be shown. Afterwards the results from a maximal phase separated structure will be analysed. Furthermore, simulations featuring a single particle have also been done for both morphologies in order to study exciton dissociation efficiencies as a function of the temperature T and the energetic disorder parameter σ. The energetic disorder parameter describes the deviation of the energies of the different sites according to a gaussian based energy distribution. This approach has also been successfully applied to various Kinetic Monte Carlo simulations [188, 189]. Also the mobility of a single charge carrier as a function of the applied external electric field has been studied.

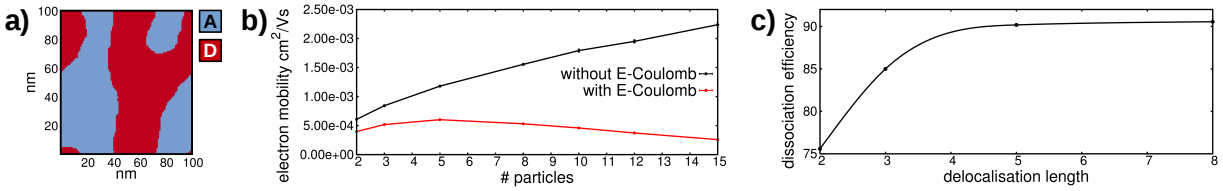

Figure 12.5: a) Phase aggregated BHJ morphology. b) Electron mobilities as a function of the number of particles with and without Coulombic forces. c) Dissociation efficiency as a function of the maximum allowed delocalisation length.

Figures 12.5a and b show the generated structure for the phase aggregated simulations and the results obtained from different many particle simulations of the generated structure, respectively. The structure shown in panel a) has been obtained using the Ising Hamiltonian with a positive sign of the coupling J, as it has been pointed out earlier. 50000 KMC steps have been performed to obtain the shown structure. The results shown in panel b) have been obtained from simulations employing a total of $n_{particles}$ x $n_{trajectories} = 10^6$, meaning that both the number of particles and the number of trajectories has been variied. Once a particle has been extracted, the simulation has been stopped and the charge carrier mobility of the respective extracted particle has been calculated. One can see for low charge carrier densities that the simulation with and without Coulombic forces follow the same trend, i.e. an increase in electron mobility. Once the density of the charge carriers reaches a certain value, the electron mobility for the simulation with Coulombic forces decreases. This is the same trend that was obtained from the simulation of the idealised morphology in figure 12.1b and the subsequent simulation in figure 12.3a. By comparing the morphologies in figure 12.5a and 12.1b one can see that the two morphologies are quite similar, i.e. both featuring an anode to cathode donor and acceptor domain. Therefore, the same argumentation for the electron mobilities is valid. For the simulation without Coulombic forces, the initial position of the extracted charge shifts more toward the anode with increasing number of particles, while for the simulation with Coulombic forces and high charge carriers, the charges will first laterally drift away from regions of high Coulombic density and then move towards the anode. Figure 12.5c shows the exciton dissociation efficiency for different lengths of delocalisation. Upon increasing the delocalisation length, the exciton dissociation efficiency increases. However, it seems to reach an asymptotic value at around 90 %. While the delocalisation of the excitons increases the overall exciton dissociation efficiency, the unique morphology of the phase aggregated structure also leads to about 10 % of loss processes, i.e. exciton recombination within the donor material and

resonant energy transfer from the donor to the acceptor.

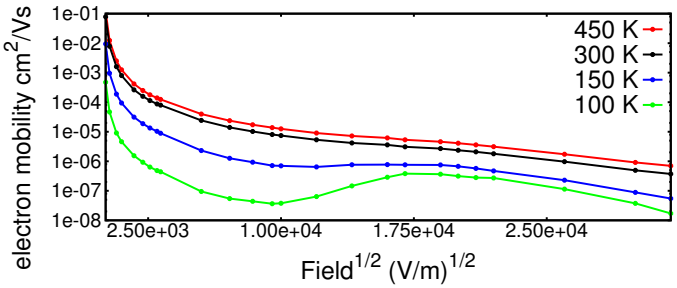

Figure 12.6: Electron mobilities as a function of the temperature T and the electric field for a phase aggregated morphology.

Table 12.2: Exciton dissociation efficiencies as a function of temperature T and energetic disorder σ

	$\frac{1}{4}\sigma$	σ	$2\ \sigma$
450 K	73.8 %	64.5 %	51.6 %
300 K	73.2 %	58.8 %	37.8 %
150 K	68.2 %	36.9 %	24.7 %
100 K	63.4 %	27.3 %	25.5 %

Figure 12.6 shows the electron mobilities for a single particle simulation for varying external electric fields and temperatures. For all four cases studied, the electron mobility decreases with increasing field strength. Since the electric field strength stands in the denominator for the calculation of the mobility, increasing fields will lead to a reduction of the mobility. While the obtained mobilities for the 450 K and 300 K simulations are fairly even, the simulation at low temperature start to deviate from the high temperature simulations. For the 150 K simulation one can see for external electric fields between $1.0 \cdot 10^8$ and $4.0 \cdot 10^8$ V/m that the mobility is nearly stationary and does not deviate much. For higher electric fields, the mobility decreases again. This behaviour is more apparent for the simulation at 100 K. Here one can see a strong increase in mobility between $1.0 \cdot 10^8$ and $3.0 \cdot 10^8$ V/m, with a decrease following afterwards. In recent literature this behaviour is explained by the Frenkel-Poole behaviour [119, 190]. At the beginning of the simulation, the disorder of the material is larger than the energetic gradient induced by the electric field, which leads to a decrease in mobility. The area with increasing mobilities is called the normal region, where the natural logarithm of the field is proportional to the square root of the field, hence also the abscissa is in units of the square root of the electric field. The subsequent decrease in mobility is related to the field being much larger than the disorder of the material. The hopping rate can not increase anymore. While the field does increase, the mobility decreases since the field strength needed for the calculation of the mobility is in the denominator, see also equation 6.28.

Table 12.2 above shows the exciton dissociation efficiencies as a function of the temperature T and the energetic disorder parameter σ. One can see for all three values of σ that with increasing temperature, the exciton dissociation efficiency increases. Additionally, for a given temperature, the exciton dissociation efficiency decreases with increasing energetic disorder σ. This behaviour is plausible if one considers the energetic disorder σ as a measure for energetically trapped states. For high energetic disorder for a given material, a lot of local energetic minima are apparent, which lead to an increase in trapped excitonic states and hence to a higher ground state recombination probability. On the other hand, for low energetic disorder, the generated excitons can move along the lattice without much hinderance and hence, reach the donor/acceptor interfacial area before the recombination to the ground state occurs.

Following the discussion of the phase-aggregated structure, the results from the phase-separated structure will be discussed.

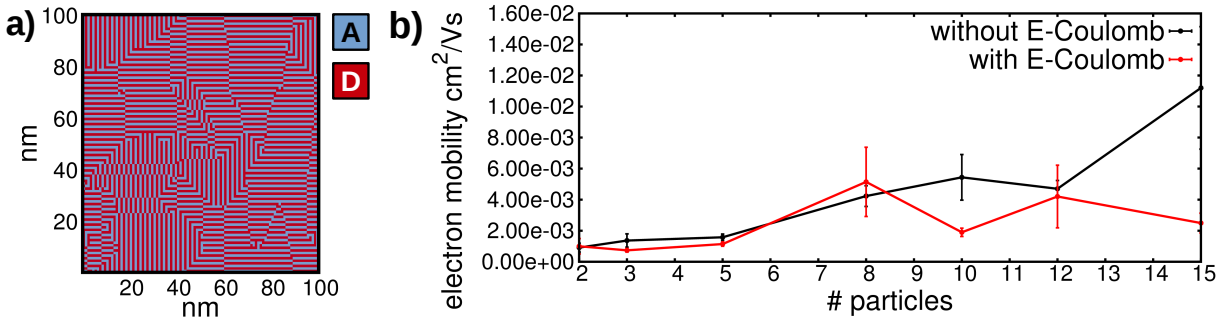

Figure 12.7: a) Phase separated BHJ morphology. b) Electron mobilities as a function of the number of particles with and without Coulombic forces.

Figure 12.7a shows the morphology used for the simulations of a phase separated donor-acceptor BHJ nanomaterial. Again, the morphology has been obtained by using the Ising Hamiltonian with a negtive J coupling between the sites, leading to a maximal phase separated structure. One can see that within the material, distinguishable domains with different orientations are present, where the charge carriers can either travel parallel or perpendicular to the applied external electric field. Also, the structure resembles typical morphologies for self-organised donor/acceptor systems in a liquid crystalline material, like it has been found for an improved version of the bisthiophene/perylenediimide donor/acceptor system studied in chapter 6 of this thesis [36]. The resulting electron mobil-

ities for simulations employing different numbers of particles is shown in figure 12.7b. As for the simulation for the phase aggregated morphology, a total of $n_{particles}$ x $n_{trajectories} = 10^6$ simulations per datapoint has been carried out. In contrast to the results shown in figure 12.5b, the results in 12.7b have a higher error bar due to higher statistical fluctuations. Furthermore, the simulations with and without Coulombic forces seem to be more identical than for the simulation of the phase aggregated morphology. The reason is that due to the high interfacial area of the material, the generated electrons can diffuse within independent acceptor domains. Also due to the unique structure, the charge carriers can only diffuse in two directions, as to the four directions in the phase aggregated morphology. Both of these effects contribute to the very similar electron mobilities for the simulation with and without Coulombic forces.

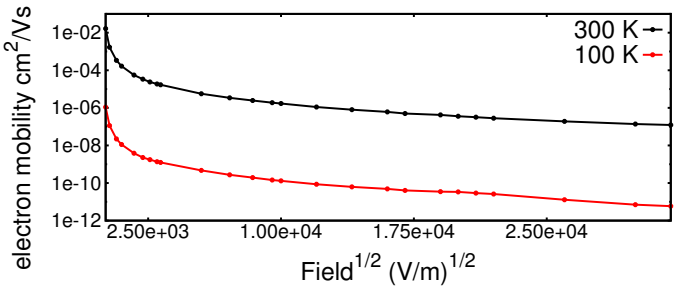

Figure 12.8: Electron mobilities as a function of the temperature T and the electric field for a phase separated morphology.

Table 12.3: Exciton dissociation efficiencies as a function of temperature T and energetic disorder σ

	$\frac{1}{4}\sigma$	σ	2 σ
450 K	97.7 %	98.0 %	99.8 %
300 K	97.9 %	97.7 %	99.3 %
150 K	97.5 %	97.7 %	98.2 %
100 K	97.8 %	97.7 %	98.4 %

Figure 12.8 shows the electron mobility for a single charge propagated in the phase separated morphology shown in figure 12.7a as a function of the applied external electric field. In contrast to the same simulation carried out for the phase aggregated simulation, the low temperature regime does not show the typical Poole-Frenkel behaviour, as compared to figure 12.6. The reason is that the electron is partially diffusing in domains with a component perpendicular to the field. Following equation 6.28, the parameter t in the denominator rises while the distance, measured as the part parallel to the field, remains constant. Therefore, the mobility should decrease monotonically. The temperature plays the same role as for the simulation in the phase aggregated morphology, i.e. high temperatures lead to a higher electron mobility.

Table 12.3 shows the exciton dissociation efficiences as a function of the temperature T and the energetic disorder parameter σ. In contrast to the observations made for the phase aggregated structure, the exciton dissociation efficiency has a very high overall value and it does neither depend on the temperature nor on the energetic disorder very much. Interestingly, the exciton dissociation efficiency even seems to increase with increasing energetic disorder, as opposed to the trend seen for the phase aggregated morphology simulations in table 12.2. This behaviour can be explained with the high interfacial area. Since the excitons are always located at an interface between donor and acceptor, it always has the possibility to either dissociate into free charge carriers or perform a resonant energy transfer within the donor regime or into the acceptor regime. For high energetic disordering, it is more likely to dissociate than to propagate within the donor material or perform a resonant energy transfer to the acceptor, resulting in slightly higher exciton dissociation efficiencies.

12.3 Coarse Graining and Modeling of 2nd Generation DA Systems

The coarse graining approach for a second generation donor-acceptor system, which has been experimentally synthesised and investigated by S. Méry et al. [35, 36, 163], has been done on the basis of a crystallographically resolved structure and the visual molecular dynamics (vmd) package [191]. With information about the unit cell, which has been obtained from X-rray crystallography, a simulation box for subsequent Kinetic Monte Carlo simulations could be generated. Of particular interest and in order to validate the chosen model system and parameter settings, the electron mobilities as a function of the particle density ρ, applied external electric field F and electron transfer integrals t_e have been calculated. The following figure will show a sketch of the coarse graining approach to obtain the model morphology for the Kinetic Monte Carlo scheme.

Figure 12.9a shows an excerpt of the crystallographically resolved structure of the full atomistic representation along the crystallographic b-axis with highlighted unit cell. One can see that along the crystallographic a-axis, the donor molecules, consisting of a modified bisthiophene derivative, are separated by a void due to their hexyl side chains. The acceptor molecules, consisting of a perylene-diimide core, are followed by another acceptor moiety, with a separation distance of approximately 12 Å. Along the crystallographic

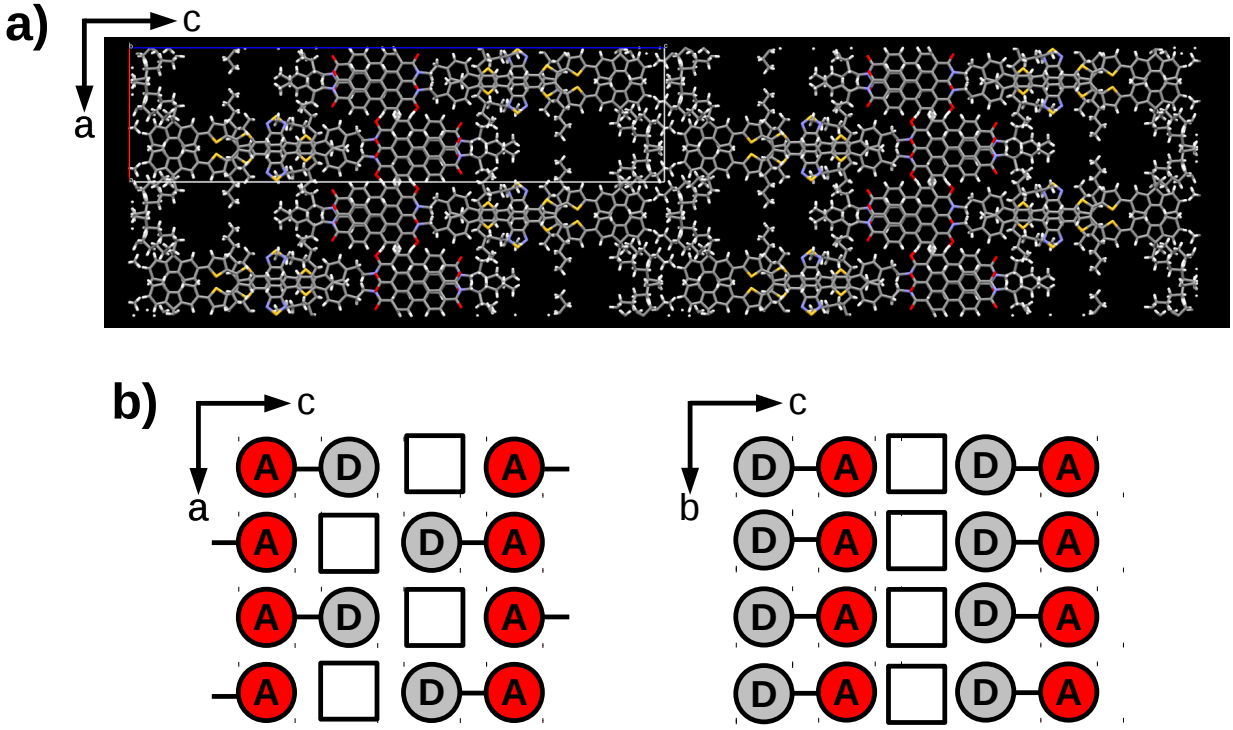

Figure 12.9: a) Full atomistic representation of the second generation donor-acceptor system with highlighted unit cell. b) Schematic representation of the coarse grained beads along different crystallographic axes.

c-axis, there are two different ordering patterns. Once, there is the ordering of A-D, while every other row features a bonding pattern of D-A molecules. The distance between the centroid of two donor or acceptor molecules is approximately 70 Å, while the distance between the different layers of donor-acceptor molecules is about 4.4 Å. A schematic representation of the ordering pattern along the a- and b-axis can be found in figure 12.9b. The view along the schematic b-axis is similar to the full atomistic representation shown in figure 12.9a. From the view along the schematic a-axis one can see the strong π-stacking of the acceptor moieties. Additionally, the donor molecules are also π-stacked. From the sketch of the coarse grained structure one can already infer that a hole transfer is mainly one dimensional along the crystallographic b-axis, perpendicular to the π-stacking of the donor molecules. The electron transfer on the other hand is at least two dimensional, with possible transfer directions along the crystallographic a- and b-axis.

The parametrisation of the Kinetic Monte Carlo scheme has been done mostly using information from quantum chemical calculations. The most important parameters for the simulations performed are listed in the following table.

Table 12.4: Important parameters for the Kinetic Monte Carlo simulations. $\hbar\omega$ and σ can be adjusted accordingly, while other parameters have been obtained from *ab-initio* calculations. All values are in eV.

$\hbar\omega$	LUMO	σ	λ_i	$\lambda_{s,a}$	$\lambda_{s,b}$	$\lambda_{s,ab}$
0.2	-2.29	0.065	0.27	0.52	0.49	0.52

Table 12.4 shows the most important parameters which remain unchanged in the following simulations. $\hbar\omega$ is a chosen frequency needed for the rate calculation via the Marcus-Levich-Jortner formalism, see also equation 11.7. The LUMO energy along with σ are responsible for the energetic fluctuations in the system, caused by the gaussian disordered energy ansatz. While the LUMO energy has been taken from quantum chemical calculations employing the CAM-B3LYP functional, the energetic disorder parameter σ has been taken from experimental investigations on PCBM electron acceptors [68]. The internal reorganisation energy λ_i has been calculated according to the scheme provided in reference [185]. The solvent reorganisation energies $\lambda_{s,jk}$ for an electron hop in the different directions has been calculated using the Born-Hush approach [192].

$$\lambda_s = \frac{e^2}{4\pi\epsilon_0}\left(\frac{1}{2r^{(j)}} + \frac{1}{2r^{(k)}} - \frac{1}{R_{CC}}\right)\left(\frac{1}{n^2} - \frac{1}{\epsilon}\right) \tag{12.1}$$

In equation 12.1 $r^{(j)}$ and $r^{(k)}$ are the radii of electron densities on the different fragments j and k and R_{CC} is the centroid-centroid distance of the hopped particle. n and ϵ are the refractive index and the dielectric constant of the solvent, respectively. For the present calculation of the solvent reorganisation energies, $n \approx 1.5$ and $\epsilon \approx 3.5$, as both resemble typical values for organic photovoltaic devices.

The proposed coarse grained model and parametrisation has been used for subsequent Kinetic Monte Carlo modeling. Therefore, simulations with different external applied electric fields, transfer integrals and particle densities have been carried out. Experimentally, typical applied external electric fields range from $10^6 - 10^8 \frac{V}{m}$ [193], while typical particle densities are on the magnitude of $\rho\left[\frac{1}{cm^3}\right] \approx 10^{15}$ [194–197]. Since the transfer integrals are

a function of the overlap between adjacent molecular orbitals, these values depend critically on the intermolecular distance between two molecules [198]. Nevertheless, transfer integrals have been calculated employing the fragment charge difference scheme (FCD), as it has been outlined in references [199, 200]. A suitable implementation of the FCD scheme can be found at reference [201], which also features an online service for the calculation of transfer integrals. Following this scheme, one obtains the following electron transfer integrals.

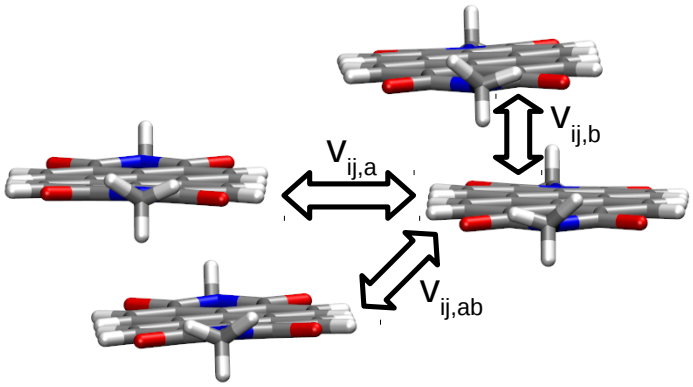

Figure 12.10: Definition of the three types of transfer integrals used for the calculation via the FCD approach.

Table 12.5: Numerical values of the electron transfer integrals calculated via the FCD approach. All values in eV.

$v_{ij,a}$	$v_{ij,b}$	$v_{ij,ab}$
$1.3e^{-5}$	0.1	0.002

Figure 12.10 shows an atomistic representation of the stacking of the acceptor moieties. As it has been pointed out above, the value of the transfer integrals depends on the overlap of the molecular orbitals. Along with figure 12.10, one can deduce that the electronic coupling $v_{ij,b}$ will have the highest value and that a charge will be transfered along this direction. Conversely, the transfer integrals $v_{ij,a}$ and $v_{ij,ab}$ will have much smaller values and thus, a transfer along these directions will be less probable. Table 12.5 shows the calculated numerical values according to the FCD method and the implemented version of reference [201].

Kinetic Monte Carlo simulations have been carried out using the coarse grained structure from X-ray crystallography and the calculated electron transfer integrals. Further, an external electric field has been applied in the crystallographic b direction, with a magnitude of $F = 10^7 V/m$. The number of charge carriers simulated at the same time has been

varied, to obtain charge carrier mobilities for low charge carrier densities and high charge carrier densities.

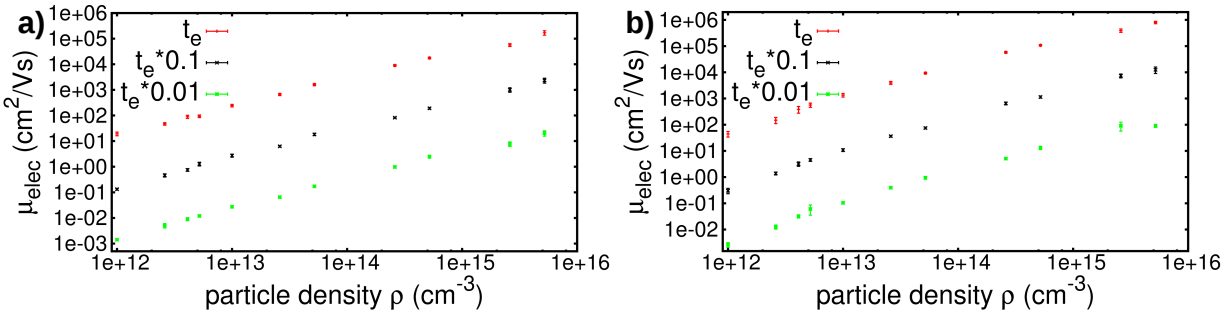

Figure 12.11: Calculated mobilities as a function of particle density for the coarse grained structure of the second generation DA system. An external electric field of $F = 10^7 V/m$ has been applied in both cases. a) $\sigma = 65$ meV. b) $\sigma = 130$ meV

Figures 12.11a and b show the obtained charge carrier mobilities calculated with equation 6.28. A double logarithmic representation of the calculated mobilities with respect to the particle density has been chosen in order to obtain a linear dependence between the electron mobility μ_{elec} and the particle density ρ. As it has been mentioned earlier, typical charge carrier densities in photovoltaic devices are on the order of $\rho \left[\frac{1}{cm^3}\right] \approx 10^{15}$. In that region, the electron mobilities are varying between 10^{-3} to $10^{+5} \frac{cm^2}{Vs}$, depending on the chosen magnitude of the transfer integrals. One can also see that the ratio for the charge carrier mobilities between the different simulation set ups is approximately 10^2, which is in agreement with the definition of the rate calculation in Marcus-Levich-Jortner theory, see also equation 11.7. Here, the rate depends quadratically on the electronic coupling. The reason for the steady increase in charge carrier mobility can be adressed to the chosen coarse grained structure, see also figures 12.9a and b. For the transfer of the electrons within the acceptor domain, one basically has a two dimensional model. Due to the 50 times higher transfer integrals along the crystallographic b direction, see also table 12.5, this two dimensional model is effectively reduced to a one dimensional transfer path. The applicaiton of an external electric field along the crystallographic b direction also enhances the transfer along this singular pathway. With an increase in charge carrier densities, the particles which are the closest to the electrode will also be pushed further towards the detection electrode by the remaining charges behind them. All of these effects lead to the steady increase in charge carrier mobilities. The reason for the marginal difference with respect to the charge carrier mobilities between figures 12.11a and b can also

be explained by the high value of the electron transfer integrals. While the simulations in figure 12.11b employing the transfer integral from table 12.5 are not very different from the corresponding simulation shown in figure 12.11a, the simulations with smaller transfer integrals, i.e. t_ex0.01, show some deviations for high charge carrier densities. One can see that the electron mobility seems to reach a steady value for these kind of simulations.

12.4 Summary and Conclusion

In comparison to the results presented in the previous chapters, this chapterwas dealing with a statistical approach to understand the processes infunctional organic materials. Here, the mesoscopic time and length scale hasbeen explored along with the long-time dynamics and macroscopic observables such as charge carrier mobilities. Based on the Ising Hamiltonian and the first reaction method (FRM), a Fortran90 code has been written for Kinetic Monte Carlo simulations on functional organic polymer materials. In contrast to standard KMC simulations on photovoltaic devices, exciton delocalisation has been explicitly taken into account via a new approach.

The subsequently performed simulations have been carried out for two different kinds of morphological realisations. On one hand, different idealised BHJ nanomorphologies have been created, where minimal structural defects were present. On the other hand, randomly generated BHJ nanomorphologies with either a phase aggregated structure or a maximum phase separated structure have been created via the Ising Hamiltonian. Every simulation has been carried out either with a real electron gas, i.e. with Coulombic forces acting between the particles, or with an idealised electron gas, where no interactions between the charged particles were allowed. The simulations on the idealised morphologies lead to diverging results. Idealised morphology **a** showed that the introduction of Coulomb interaction leads to a decrease in mobility as a function of the particle density, while in the absence of Coulombic forces, the electron mobility remained constant. In contrast, morphology **b** showed that the electron mobility rises with increasing particle density, but only in the absense of Coulomb interaction. If Coulomb interactions were allowed between the particles, the mobility decreased slightly. It has turned out that for the simulation of the idealised electron gas, the starting position of the extracted electron shifted towards the anode with increasing particle density, leading to a shorter distance and time until the extraction happens. For the real electron gas, i.e. the simulation with Coulombic

interactions, a minority of the extracted charge carriers was generated at the bottom of the device. Therefore, the electron first had to avoid areas of high Coulombic density and hence, the time until the extraction at the anode happens was highly enhanced. For the idealised morphology **c**, electron moblities for the idealised and real electron gas were nearly identical, which is due to the unique structure of distinctive donor and acceptor columns and hence, leading to a nearly ideal behaviour of the real electron gas.

For the randomly generated BHJ nanomorphologies, two distinct cases were investigated. As a first, a maximally phase aggregated and a maximally phase separated structure was studied. The phase aggregated structure looks similar to the ideal morphology **b** and hence, the trend of the mobilities with and without Coulombic interactions are similar to the mobilities of idealised morphology **b**. Furthermore, single particle simulations have been carried out as well to study the mobility as a function of the external electric field and the temperature. Here, one could see that for low temperatures, a Poole-Frenkel behaviour of the electron mobility could be detected, which has also been reported experimentally for several photovoltaic devices. Additionally, the exciton dissociation efficiency as a function of the temperature and the energetic disorder has been investigated. Here, one could see that the exciton dissociation efficiency increases with increasing temperature and with decreasing energetic disorder, leading to the conclusion that devices with less structural defects are beneficial.

The results from the simulation of the phase separated structure are somewhat different. Here, one can see that the mobilities for the simulation of the real and ideal electron gas are similar, indicating that the real electron gas behaves nearly ideal. This is due to the unique structural organisation, where individual donor and acceptor domains are present. Interestingly, the single particle simulations of the electron mobility do not show a Poole-Frenkel type behaviour, even for low temperatures. Also the mobility in general is much lower due to the unique structure of the BHJ nanodevice. The exciton dissociation efficiency has also been investigated as a function of the temperature and the energetic disorder, showing nearly no dependence of these parameters. This can be explained by the high interfacial area of the material, leading to a very high dissociation efficiency in general without much loss processes.

In addition to the results on idealised and randomly generated morphologies, simulations for a coarse grained structure of a covalently bonded donor-acceptor system have been presented. This system is the second-generation variant of the donor-acceptor systems developoed by the Strasbourg group, see also the discussion of section 8.5. The coarse grained structure has been obtained from crystallographic X-ray measurements and molecular modeling techniques. The performed Kinetic Monte Carlo simulations were used to identify the impact of the charge carrier density on the resulting electron mobilities. In order to obtain highly accurate transfer rates, the Marcus-Levich-Jortner formalism has been used, with parameters obtained from quantum chemical calculations. The subsequently obtained results show a steady increase of the charge carrier mobility with the particle density, even for simulations with higher energetic disorder. This behaviour can be explained by the unique structure of the coarse grained system along with its transfer integrals. Ultimately, the high transfer integrals lead to a one dimensional transfer pathway throughout the entire coarse grained structure, due to the 50 times higher transfer integrals along the π stacking direction as compared to any other direction. Simulations with a higher energetic disorder show the same behaviour for high values of the transfer integrals. The obtained charge carrier mobilities for smaller transfer integrals and high particle densities show a steady charge carrier mobility.

To conclude, it can be said that the Kinetic Monte Carlo simulations presented in this chapter provide an interesting insight into the macroscopic observables and the mesoscopic length and time scales of BHJ nanodevices. While these results might be interesting in terms of the time scale they cover, the quantum regime of these processes is not captured and can have a significant influence on the dynamics. For the simulations for the idealised and randomly generated morphologies, the presented simulations have been carried out for a two dimensional structure. Here, real devices are usually three dimensional, implying that the results might be altered by the additional spatial dimensionality in future studies. The results from the coarse grained structure lack structural disorder, which may lead to an overestimation of charge carrier mobilities. Further, the simultaneous treatment of electron and hole dynamics are also missing, which may also influence the particle mobilities.

13 — Conclusion and Outlook

Live [...] That Is All I Can Tell You

Naomi Hunter

The work presented in this thesis opens new avenues to the theoretical understanding of the fundamental processes in functional organic nanomaterials. The description of these processes on a microscopic scale, i.e., on length scales up to tens of Angstroms and time scales of femtoseconds to picoseconds, can be achieved at a full quantum mechanical level of description. To this end, we employ electron-hole lattice models parametrized from first principles – i.e., using a detailed electronic structure characterization of the relevant fragments – together with high-dimensional wavepacket propagation methods, notably the Multi-Layer Multiconfiguration Time-Dependent Hartree (ML-MCTDH) approach. This level of analysis is able to capture coherent short-time transients while taking into account the delocalization of excitonic and carrier species. Since the relevant elementary processes are often ultrafast, this approach is a unique tool to understand the elementary steps of exciton dissociation and carrier transport. However, the generation of charge carriers represents a typical multiscale problem, and processes on longer time scales and in macromolecular assemblies equally play a crucial role in the determination of the efficiency of organic solar cell devices. Therefore, simulations on the mesoscopic scale, relating to length scales of nanometers and time scales from picoseconds to microseconds, were also performed, using statistical methods of Kinetic Monte Carlo (KMC) type. Eventually, these two ends of the spectrum should be combined in a multiscale modeling approach.

The first project presented in this thesis was based on a collaboration with the groups of Dr. S. Méry and Prof. S. Haacke from Strasbourg University. Experimental investigations of a novel perylene diimide based block-co-oligomer donor-acceptor (DA) combination via time resolved UV-vis spectroscopy revealed major differences in the charge transfer dynam-

ics, depending on whether the DA system in solution or in a liquid crystalline phase was studied. In order to interpret these results, an electron-hole type model Hamiltonian was employed, in conjunction with high-level ADC(2) calculations and a quasi-diabatization scheme, and quantum dynamical calculations were carried out for up to 156 states and 48 modes. This analysis shows that an intermolecular charge transfer channel opens in the liquid crystalline phase, explaining the pronounced difference to DA system in solution. This charge transfer pathway is due to a unique DA stacking resulting from a strongly tilted alignment in the liquid crystalline phase. Moreover, our studies show that despite an initial, ultrafast charge separation, long-range carrier generation is inefficient due to small transfer integrals for electron (hole) transfer along with a high Coulomb barrier. In agreement with this analysis, the experiment shows a high recombination rate.

The second project was based on recent experimental investigations of neat regioregular P3HT, where long lived periodic oscillations were detected and attributed to the formation of polaron pairs. To understand the electronic or vibrational origin of these oscillations, we carried out simulations for three and five stacked tetrathiophene (OT-4) units, including a large number of normal modes exhibiting non-zero vibronic couplings. For the stacked trimer aggregate, calculations for seven states and 120 modes were performed, showing that charge transfer exciton formation sets in within tens of femtoseconds, due to strong electronic couplings. In line with previous studies, a significant mixture of excitonic and charge transfer states was indeed observed in our electronic structure calculations, at the ADC(2) level. Oscillatory signals in the experimentally observed range are found – around 1600 cm^{-1} – which can be attributed to a combination of high-frequency CC stretch type modes and excitonic couplings in the same energy range.

Based on the results of the second project, we investigated whether the formation of charge transfer excitons in neat regioregular poly-3-hexyl-thiophene (P3HT), again modeled by stacked OT-4 species, modifies the carrier generation in a typical organic functional material based on P3HT as electron donating and fullerene (PCBM) as electron accepting materials. To this end, we augmented a parametrized Hamiltonian that was previously developed in the group, such as to include the formation of P3HT charge transfer excitons and their coupling to the exciton dissociation step at the P3HT/PCBM interface. The simulations comprised 13 OT-4 fragments and a single fullerene “super-site”. Several sets of simulations were carried out – for 27, 50 or 182 electronic states – depending on whether

the P3HT charge transfer exciton manifold was partially or fully included. It turns out that the presence of P3HT charge transfer excitons leads to a significant reduction of trapping in the interfacial P3HT/PCBM charge transfer state. At the same time, though, one does not observe an increase in free carrier formation. This can be explained by the fact that the additional charge separated states in the donor domain also act as local traps, impeding more efficient long-range charge separation.

The last project of this thesis deals with the statistical description and the dynamics on longer time scales, i.e. on a mesoscopic scale. Since both short-time and long-time dynamics are important in the overall understanding of functional nanomaterials, a KMC studies of such materials have been carried out. These studies prepare the ground for an in-depth analysis of a second-generation donor-acceptor system devised by the Strasbourg group, whose charge separation dynamics occurs on a time scale of tens to hundreds of picoseconds. To this end, a Fortran90 code employing the *First Reaction Method* algorithm to solve the master equation was developed. Additionally, as non-standard feature, exciton delocalization effects were incorporated into the KMC code. Several representative morphologies were tested, either corresponding to idealized structures like bilayer architectures or else to structures generated from energy minimisation of the Ising Hamiltonian, which yields either maximally phase aggregated or phase separated morphologies. The idealised morphologies and the Ising model based phase separated morphologies show that it is possible to obtain electronic dynamics which nearly resemble the behaviour of an idealised electron gas for low charge carrier densities. From these simulations one can therefore deduce design principles which specifically relate to carrier mobility. The statistical description has also been applied to a coarse grained structure of the second-generation DA system developed by the Strasbourg group, as mentioned above. From KMC simulations for different charge carrier densities, one can infer that electron mobility increases steadily with increasing particle density. This behaviour can be explained by the unique structure of the system, in the absence of any structural disorder. Due to the large transfer integrals along the π stacking direction of the acceptor molecules, a one-dimensional electron transport pathway throughout the entire domain is created. With an increasing number of charges present in the system, the charge closest to the detection electrode will be pushed even more towards this direction. In future work, this mechanism will be verified within a more complete description.

To conclude, this thesis has addressed both ultrashort time scales and long time scales, using efficient and accurate multiconfigurational quantum dynamics methods as well as Kinetic Monte Carlo techniques. From both viewpoints, design criteria and insight into the charge generation and free carrier transport can be gained. To correctly include statistical effects on all time and length scales, a quantum-classical multi-scale approach is necessary which is not yet available to date. The present study prepares the ground in this direction, for representative systems that were studied in close collaboration with experiment.

Part IV

Appendix

ML-MCTDH Partitioning Scheme for chapter 8

As it has been mentioned in chapter 8, the ML-MCTDH method as implemented in the Heidelberg MCTDH package was used to study the ultrafast exciton dissociation in a liquid crystalline donor-acceptor system. The model Hamiltonian featured a total of 156 electronic states and 48 degrees of freedom. As a partitioning of the wave function, a seven layer approach has been chosen, with a varying number of single particle functions (SPF) for each node. With respect to the primitve grid, an harmonic oscillator discrete variable representation (DVR) for all vibrational modes has been used. In particular, the high frequency bond length alternation modes have been described by 32 grid points, the intermolecular mode by 64 grid points and the low frequency torsional degree of freedom by 128 grid points. The following table shows typical numbers of the SPFs used for the dynamical evolution of the system.

Table 13.1: Typical partitioning scheme for the ML-MCTDH calculations employing 156 electronic states and 48 degrees of freedom.

Layer	1	2	3	4	5	6
SPF	[24,156]	[21,7]	[12,12,19]	[6,8]	[4,4,4]	[4,2,3]

Graphically, a partitioning of the wave function can be represented as follows.

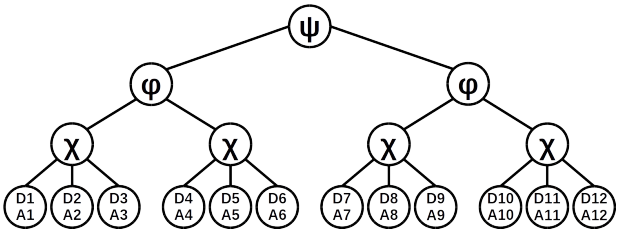

Figure 13.1: Graphical representation of the ML-MCTDH wave function partitioning of chapter 8. The sketch is shown for a four layer realization of the ML-MCTDH partitioning.

ML-MCTDH Partitioning Scheme for chapter 9

The wave function partitioning for the ML-MCTDH calculations performed in chapter 9 are different to the one presented for chapter 8. While for the wave function partitioning

in the previous chapter a site specific partitioning has been used, i.e. modes located on the same site have been assigned to the same layer, this was not the case for the present simulation set up. As it has been outlined in chapter 9, a normal mode ansatz and effective mode decomposition has been used to describe the ultrafast dynamics upon photoexcitation. Therefore, the wave function has been partitioned as to obtain layers with at most three degrees of freedom. The DVR has been represented by an harmonic oscillator representation employing 32 grid points for all phonon modes, irrespective of the normal mode or effective mode ansatz. This partitioning led to a seven layer representation for the normal mode ansatz of the wave function, for which a representative number of SPFs looks as follows.

Table 13.2: Typical partitioning scheme for the ML-MCTDH calculations employing seven electronic states and 117 degrees of freedom of the normal mode ansatz.

Layer	1	2	3	4	5	6
SPF	[27,15]	[23,23,23]	[12,9,9]	[7,7,7]	[7,7]	[5,5,5]

For the effective mode decomposition, the partitionig scheme depends strongly on the number of effective mode layers used for the dynamics. The number of phonon modes is calculated by 7xN, with N being the number of effective mode layers.

Table 13.3: Typical partitioning scheme for the ML-MCTDH calculations employing seven electronic states and 21 degrees of freedom of the effective mode ansatz with three layers.

Layer	1	2	3	4
SPF	[12,30]	[19,19,12]	[9,15,15]	[5,15,9]

Table 13.4: Typical partitioning scheme for the ML-MCTDH calculations employing seven electronic states and 28 degrees of freedom of the effective mode ansatz with four layers.

Layer	1	2	3	4	5
SPF	[18,30]	[19,19]	[27,19]	[9,25,25]	[7,21,21]

Table 13.5: Typical partitioning scheme for the ML-MCTDH calculations employing seven electronic states and 35 degrees of freedom of the effective mode ansatz with five layers.

Layer	1	2	3	4	5
SPF	[18,30]	[16,10]	[25,25,13]	[15,15,15]	[12,12]

One can see that between the different effective mode simulation set ups with an increasing number of phonon modes, the number of SPFs per node is very different and a generalization of an efficient partitioning scheme can not be given.

ML-MCTDH Partitioning Scheme for chapter 10

The wave function partitioning of the dynamics presented in chapter 10 feature the most phonon modes and number of electronic states studied in this thesis. While all simulations employed a total of 112 degrees of freedom, the number of electronic degrees of freedom varied between 27 and 182. This had also influence on number of SPFs needed for the description of phonon modes, since different distributions of active modes would be obtained. In general, a partitioning of the wave function into six layers has been done. The primitive grid has been represented by an harmonic oscillator DVR employing 32 grid points for all phonon modes.

Table 13.6: Typical partitioning scheme for the ML-MCTDH calculations employing 27 electronic states and 112 degrees of freedom.

Layer	1	2	3	4	5	6
SPF	[39,39,27]	[35,35]	[29,29]	[19,19]	[12,12,7]	[4,4,7]

Table 13.7: Typical partitioning scheme for the ML-MCTDH calculations employing 50 electronic states and 112 degrees of freedom.

Layer	1	2	3	4	5	6
SPF	[45,45,50]	[39,35]	[31,31]	[32,32]	[7,12,10]	[4,7,7]

Table 13.8: Typical partitioning scheme for the ML-MCTDH calculations employing 182 electronic states and 112 degrees of freedom.

Layer	1	2	3	4	5	6
SPF	[32,32,182]	[29,29]	[24,24]	[15,15]	[7,7,7]	[4,4,4]

One can see that the simulation employing 182 electronic states uses the least amount of SPFS to describe the different wave function layers, see table 13.8. The reason is that due to the huge number of states, only up to 200 femtoseconds have been propagated, resulting in less SPFs needed to describe the evolution of the system appropriately.

Bibliography

[1] Bundesverband der Energie- und Wasserwirtschaft e.V., Energiewirtschaftliche Entwicklung in Deutschland, http://www.solarify.eu/2013/06/01/bdew-energie-info-fur-erstes-quartal/, **2013**.

[2] J. H. Mercer, *Nature* **1978**, *271*.

[3] M. S. Dresselhaus, I. L. Thomas, *Nature* **2001**, *414*.

[4] T. B. Johansson, H. Kelly, A. K. N. Reddy, R. H. Williams, *Energy Studies Review* **1993**, *4*.

[5] The Norwegian Water Resources and Energy Directorate, Vannkraftpotensialet - NVE, https://www.nve.no/energiforsyning-og-konsesjon/vannkraft/vannkraftpotensialet, **2015**.

[6] Statistics Norway, Lower operating profit for power plants, http://www.ssb.no/en/energi-og-industri/statistikker/elektrisitetaar/aar/2013-03-20?fane=tabell&sort=nummer&tabell=104227, **2015**.

[7] NREL, US Department of Energy, Office of Energy Efficiency and Renewable Energy, http://www.nrel.gov/ncpv/images/efficiency_chart.jpg, **2015**.

[8] S. Pizzini, *Solar Energy Materials and Solar Cells* **2010**, *94*.

[9] B. O'Regan, M. Grätzel, *Nature* **1991**, *353*.

[10] F. C. Krebs, M. Jørgensen, K. Norrman, O. Hagemann, J. Alstrup, T. D. Nielsen, J. Fyenbo, K. Larsen, J. Kristensen, *Solar Energy Materials and Solar Cells*, Processing and Preparation of Polymer and Organic Solar Cells **2009**, *93*.

[11] A. Shah, *Science* **1999**, *285*.

[12] H. Klauk, *Chemical Society Reviews* **2010**, *39*.

[13] Hitachi Ltd. Corporation, High functional materials, `http://www.hitachi.com/environment/showcase/solution/materials/images/img_high_functional/07.jpg`.

[14] S.-J. Xiong, Y. Xiong, Y. Zhao, *The Journal of Chemical Physics* **2012**, *137*.

[15] T. Adachi, G. Lakhwani, M. C. Traub, R. J. Ono, C. W. Bielawski, P. F. Barbara, D. A. Vanden Bout, *The Journal of Physical Chemistry B* **2012**, *116*.

[16] A. Köhler, S. T. Hoffmann, H. Bässler, *Journal of the American Chemical Society* **2012**, *134*.

[17] M. M.-L. Grage, P. W. Wood, A. Ruseckas, T. Pullerits, W. Mitchell, P. L. Burn, I. D. W. Samuel, V. Sundström, *The Journal of Chemical Physics* **2003**, *118*.

[18] A. N. Panda, F. Plasser, A. J. A. Aquino, I. Burghardt, H. Lischka, *The Journal of Physical Chemistry A* **2013**, *117*.

[19] M. Scheidler, U. Lemmer, R. Kersting, S. Karg, W. Riess, B. Cleve, R. F. Mahrt, H. Kurz, H. Bässler, E. O. Göbel, P. Thomas, *Physical Review B* **1996**, *54*.

[20] D. Chen, A. Nakahara, D. Wei, D. Nordlund, T. P. Russell, *Nano Letters* **2011**, *11*.

[21] W. Ma, C. Yang, X. Gong, K. Lee, A. J. Heeger, *Advanced Functional Materials* **2005**, *15*.

[22] M. T. Dang, L. Hirsch, G. Wantz, *Advanced Materials* **2011**, *23*.

[23] P. Vanlaeke, A. Swinnen, I. Haeldermans, G. Vanhoyland, T. Aernouts, D. Cheyns, C. Deibel, J. D'Haen, P. Heremans, J. Poortmans, J. Manca, *Solar Energy Materials and Solar Cells* **2006**, *90*.

[24] J. Davis, A. Rohatgi, R. Hopkins, P. Blais, P. Rai-Choudhury, J. McCormick, H. Mollenkopf, *IEEE Transactions on Electron Devices* **1980**, *27*.

[25] J. Czochralski, *Zeitschrift fuer Physikalische Chemie* **1918**, *92*.

[26] P. Woditsch, W. Koch, *Solar Energy Materials and Solar Cells*, EMRS 2001 Symposium E: Crystalline Silicon for Solar Cells **2002**, *72*.

[27] J. Aleksic, P. Zielke, J. A. Szymczyk, *Annals of the New York Academy of Sciences* **2002**, *972*.

[28] S. Günes, H. Neugebauer, N. S. Sariciftci, *Chemical Reviews* **2007**, *107*.

[29] C. W. Tang, *Applied Physics Letters* **1986**, *48*.

[30] N. S. Sariciftci, L. Smilowitz, A. J. Heeger, F. Wudl, *Science* **1992**, *258*.

[31] G. Yu, J. Gao, J. C. Hummelen, F. Wudl, A. J. Heeger, *Science* **1995**, *270*.

[32] H. M. Heitzer, B. M. Savoie, T. J. Marks, M. A. Ratner, *Angewandte Chemie International Edition* **2014**, *53*.

[33] *Photoresponsive Polymers I*, (Eds.: S. R. Marder, K.-S. Lee), Springer Berlin Heidelberg, Berlin, Heidelberg, **2008**.

[34] *Photoresponsive Polymers II*, (Eds.: S. R. Marder, K.-S. Lee), Springer Berlin Heidelberg, Berlin, Heidelberg, **2008**.

[35] P.-O. Schwartz, L. Biniek, E. Zaborova, B. Heinrich, M. Brinkmann, N. Leclerc, S. Méry, *Journal of the American Chemical Society* **2014**, *136*.

[36] L. Biniek, P.-O. Schwartz, E. Zaborova, B. Heinrich, N. Leclerc, S. Méry, M. Brinkmann, *J. Mater. Chem. C* **2015**, *3*.

[37] J. Frenkel, *Physical Review* **1931**, *37*.

[38] T. J. Magnanelli, A. E. Bragg, *The Journal of Physical Chemistry Letters* **2015**, *6*.

[39] R. Binder, M. Polkehn, T. Ma, I. Burghardt, *Chemical Physics* **2017**, *482*.

[40] T. Förster, *Annalen der Physik* **1948**, *437*.

[41] I. Maqsood, L. D. Cundy, M. Biesecker, J.-H. Kimn, D. Johnson, R. Williams, V. Bommisetty, *The Journal of Physical Chemistry C* **2013**, *117*.

[42] S. Athanasopoulos, E. V. Emelianova, A. B. Walker, D. Beljonne, *Physical Review B* **2009**, *80*.

[43] J. Frenkel, *Zeitschrift für Physik* **1929**, *58*.

[44] K. Feron, X. Zhou, W. J. Belcher, P. C. Dastoor, *Journal of Applied Physics* **2012**, *111*.

[45] G. Grancini, M. Maiuri, D. Fazzi, A. Petrozza, H.-J. Egelhaaf, D. Brida, G. Cerullo, G. Lanzani, *Nature Materials* **2012**, *12*.

[46] H. Iizuka, T. Nakayama, *Japanese Journal of Applied Physics* **2016**, *55*.

[47] I. A. Howard, R. Mauer, M. Meister, F. Laquai, *Journal of the American Chemical Society* **2010**, *132*.

[48] V. D. Mihailetchi, L. J. A. Koster, J. C. Hummelen, P. W. M. Blom, *Physical Review Letters* **2004**, *93*.

[49] D. H. K. Murthy, M. Gao, M. J. W. Vermeulen, L. D. A. Siebbeles, T. J. Savenije, *The Journal of Physical Chemistry C* **2012**, *116*.

[50] G. R. Hutchison, M. A. Ratner, T. J. Marks, *Journal of the American Chemical Society* **2005**, *127*.

[51] J.-S. Lee, M. V. Kovalenko, J. Huang, D. S. Chung, D. V. Talapin, *Nature Nanotechnology* **2011**, *6*.

[52] S. Stafström, *Chemical Society Reviews* **2010**, *39*.

[53] M. Scheele, *Zeitschrift für Physikalische Chemie* **2015**, *229*.

[54] Y. Yamashita, J. Tsurumi, F. Hinkel, Y. Okada, J. Soeda, W. Zajaczkowski, M. Baumgarten, W. Pisula, H. Matsui, K. Müllen, J. Takeya, *Advanced Materials* **2014**, *26*.

[55] R. E. Merrifield, *The Journal of Chemical Physics* **1961**, *34*.

[56] R. E. Merrifield, *The Journal of Chemical Physics* **1963**, *38*.

[57] *Dynamics at Solid State Surfaces and Interfaces: Current Developments*, (Eds.: U. Bovensiepen, H. Petek, M. Wolf), Wiley-VCH Verlag GmbH & Co. KGaA, Weinheim, Germany, **2010**.

[58] R. A. Marcus, *The Journal of Chemical Physics* **1956**, *24*.

[59] S. M. Khopde, K. Priyadarsini, *Biophysical Chemistry* **2000**, *88*.

[60] D. Godovsky, *Organic Electronics* **2011**, *12*.

[61] A. J. Ward, A. Ruseckas, M. M. Kareem, B. Ebenhoch, L. A. Serrano, M. Al-Eid, B. Fitzpatrick, V. M. Rotello, G. Cooke, I. D. W. Samuel, *Advanced Materials* **2015**, *27*.

[62] G. Grampp, *Angewandte Chemie International Edition in English* **1993**, *32*.

[63] V. May, O. Kühn, *Charge and Energy Transfer Dynamics in Molecular Systems*, John Wiley & Sons, **2008**.

[64] W. P. Su, J. R. Schrieffer, A. J. Heeger, *Physical Review Letters* **1979**, *42*.

[65] W. P. Su, J. R. Schrieffer, A. J. Heeger, *Physical Review B* **1980**, *22*.

[66] S. Donets, A. Pershin, M. J. A. Christlmaier, S. A. Baeurle, *The Journal of Chemical Physics* **2013**, *138*.

[67] C. Peter, K. Kremer, *Soft Matter* **2009**, *5*.

[68] C. Deibel, T. Strobel, V. Dyakonov, *Physical Review Letters* **2009**, *103*.

[69] M. L. Jones, R. Dyer, N. Clarke, C. Groves, *Physical Chemistry Chemical Physics* **2014**, *16*.

[70] E. Collini, G. D. Scholes, *Science* **2009**, *323*.

[71] E. Collini, G. D. Scholes, *The Journal of Physical Chemistry A* **2009**, *113*.

[72] I. Hwang, G. D. Scholes, *Chemistry of Materials* **2011**, *23*.

[73] M. Cho, J.-Y. Yu, T. Joo, Y. Nagasawa, S. A. Passino, G. R. Fleming, *The Journal of Physical Chemistry* **1996**, *100*.

[74] X. Yang, T. E. Dykstra, G. D. Scholes, *Physical Review B* **2005**, *71*.

[75] F. Fassioli, A. Nazir, A. Olaya-Castro, *The Journal of Physical Chemistry Letters* **2010**, *1*.

[76] W. Barford, C. D. P. Duffy, *Physical Review B* **2006**, *74*.

[77] A. G. Redfield, *IBM Journal of Research and Development* **1957**, *1*.

[78] E. Schrödinger, *Annalen der Physik* **1926**, *385*.

[79] M. Born, R. Oppenheimer, *Annalen der Physik* **1927**, *389*.

[80] G. A. Worth, L. S. Cederbaum, *Annual Review of Physical Chemistry* **2004**, *55*.

[81] C. A. Mead, D. G. Truhlar, *The Journal of Chemical Physics* **1982**, *77*.

[82] A. Thiel, H. Köppel, *The Journal of Chemical Physics* **1999**, *110*.

[83] H. Nakamura, D. G. Truhlar, *The Journal of Chemical Physics* **2001**, *115*.

[84] H. Choi, K. K. Baeck, T. J. Martinez, *Chemical Physics Letters* **2004**, *398*.

[85] Q. Ou, J. E. Subotnik, *The Journal of Physical Chemistry C* **2013**, *117*.

[86] H. Tamura, *The Journal of Physical Chemistry A* **2016**, *120*.

[87] A. Szabo, N. S. Ostlund, *Modern Quantum Chemistry: Introduction to Advanced Electronic Structure Theory*, Revised ed. edition, Dover Publications, Mineola, N.Y, **1996**.

[88] C. J. Cramer, *Essentials of Computational Chemistry: Theories and Models*, 2 edition, Wiley, West Sussex ; Hoboken, **2004**.

[89] A. P. J. Jansen, *arXiv:cond-mat/0303028* **2003**.

[90] R. M. Dreizler, E. K. U. Gross, *Density Functional Theory: An Approach to the Quantum Many-Body Problem*, Springer, Berlin; New York, **1996**.

[91] A. Dreuw, M. Head-Gordon, *Chemical Reviews* **2005**, *105*.

[92] M. Wormit, PhD thesis.

[93] O. Christiansen, H. Koch, P. Jørgensen, *Chemical Physics Letters* **1995**, *243*.

[94] A. B. Trofimov, J Schirmer, *Journal of Physics B: Atomic Molecular and Optical Physics* **1995**, *28*.

[95] P. Hohenberg, W. Kohn, *Physical Review* **1964**, *136*.

[96] W. Kohn, L. J. Sham, *Physical Review* **1965**, *140*.

[97] A. D. Becke, *The Journal of Chemical Physics* **1993**, *98*.

[98] E. Runge, E. K. U. Gross, *Physical Review Letters* **1984**, *52*.

[99] J. Schirmer, *Physical Review A* **2012**, *86*.

[100] M. E. Casida, *Recent Advances in Density Functional Methods:(Part I)* **1995**, *1*.

[101] C. Moller, M. S. Plesset, *Physical Review* **1934**, *46*.

[102] H. G. Kümmel, *International Journal of Modern Physics B* **2003**, *17*.

[103] A. Dreuw, M. Wormit, *Wiley Interdisciplinary Reviews: Computational Molecular Science* **2015**, *5*.

[104] J. Schirmer, A. B. Trofimov, *The Journal of Chemical Physics* **2004**, *120*.

[105] H.-D. Meyer, U. Manthe, L. Cederbaum, *Chemical Physics Letters* **1990**, *165*.

[106] M Beck, *Physics Reports* **2000**, *324*.

[107] O. Vendrell, H.-D. Meyer, *The Journal of Chemical Physics* **2011**, *134*.

[108] A. P. J. Jansen, *The Journal of Chemical Physics* **1991**, *94*.

[109] C. Groves, *Energy & Environmental Science* **2013**, *6*.

[110] M. C. Heiber, A. Dhinojwala, *The Journal of Chemical Physics* **2012**, *137*.

[111] P. K. Watkins, A. B. Walker, G. L. B. Verschoor, *Nano Letters* **2005**, *5*.

[112] M. V. Fischetti, S. E. Laux, *Physical Review B* **1988**, *38*.

[113] R. Binder, J. Wahl, S. Römer, I. Burghardt, *Faraday Discussions* **2013**, *163*.

[114] S. Mukamel, *Science* **1997**, *277*.

[115] S. Karabunarliev, E. R. Bittner, *The Journal of Chemical Physics* **2003**, *118*.

[116] J. Wahl, R. Binder, I. Burghardt, *Computational and Theoretical Chemistry* **2014**, *1040-1041*.

[117] M. Hoffmann, K. Schmidt, T. Fritz, T. Hasche, V. M. Agranovich, K. Leo, *Chemical Physics* **2000**, *258*.

[118] F. C. Spano, C. Silva, *Annual Review of Physical Chemistry* **2014**, *65*.

[119] J. Frenkel, *Physical Review* **1938**, *54*.

[120] H. Köppel, W. Domcke, L. Cederbaum, *Conical Intersections Vol. 15*, World Scientific, Singapore, **2004**.

[121] H. Köppel, W. Domcke, L. S. Cederbaum in *Advances in Chemical Physics*, *Vol. 57*, (Eds.: I. Prigogine, S. A. Rice), John Wiley & Sons, Inc., Hoboken, NJ, USA, **1984**.

[122] E. U. Condon, *Physical Review* **1928**, *32*.

[123] E. Condon, *Physical Review* **1926**, *28*.

[124] J. Franck, E. G. Dymond, *Transactions of the Faraday Society* **1926**, *21*.

[125] E. Gindensperger, I. Burghardt, L. S. Cederbaum, *The Journal of Chemical Physics* **2006**, *124*.

[126] K. H. Hughes, C. D. Christ, I. Burghardt, *The Journal of Chemical Physics* **2009**, *131*.

[127] H. Mori, *Progress of Theoretical Physics* **1965**, *34*.

[128] H. Tamura, E. R. Bittner, I. Burghardt, *The Journal of Chemical Physics* **2007**, *126*.

[129] H. Tamura, J. G. S. Ramon, E. R. Bittner, I. Burghardt, *Physical Review Letters* **2008**, *100*.

[130] H. Tamura, J. G. S. Ramon, E. R. Bittner, I. Burghardt, *The Journal of Physical Chemistry B* **2008**, *112*.

[131] M. Huix-Rotllant, H. Tamura, I. Burghardt, *The Journal of Physical Chemistry Letters* **2015**, *6*.

[132] H. Tamura, I. Burghardt, *Journal of the American Chemical Society* **2013**, *135*.

[133] E. Ising, *Zeitschrift für Physik* **1925**, *31*.

[134] M. C. Heiber, A. Dhinojwala, *The Journal of Physical Chemistry C* **2013**, *117*.

[135] K. Feron, C. J. Fell, L. J. Rozanski, B. B. Gong, N. Nicolaidis, W. J. Belcher, X. Zhou, E. Sesa, B. V. King, P. C. Dastoor, *Applied Physics Letters* **2012**, *101*.

[136] L. Meng, Y. Shang, Q. Li, Y. Li, X. Zhan, Z. Shuai, R. G. E. Kimber, A. B. Walker, *The Journal of Physical Chemistry B* **2010**, *114*.

[137] R. G. E. Kimber, A. B. Walker, G. E. Schröder-Turk, D. J. Cleaver, *Physical Chemistry Chemical Physics* **2010**, *12*.

[138] *The Journal of Chemical Physics* **2011**, *134*.

[139] M. C. Heiber, A. Dhinojwala, *Physical Review Applied* **2014**, *2*.

[140] T Roland, G. H. Ramirez, J Leonard, S Mery, S Haacke, *Journal of Physics: Conference Series* **2011**, *276*.

[141] T. Roland, J. Leonard, G. Hernandez Ramirez, S. Mery, O. Yurchenko, S. Ludwigs, S. Haacke, *Physical Chemistry Chemical Physics* **2012**, *14*.

[142] G. H. Ramirez, PhD thesis, Université de Strasbourg, **2010**.

[143] K. Hara, M. Kurashige, Y. Dan-oh, C. Kasada, A. Shinpo, S. Suga, K. Sayama, H. Arakawa, *New Journal of Chemistry* **2003**, *27*.

[144] G. Li, R. Zhu, Y. Yang, *Nature Photonics* **2012**, *6*.

[145] Y. Lin, Y. Wang, J. Wang, J. Hou, Y. Li, D. Zhu, X. Zhan, *Advanced Materials* **2014**, *26*.

[146] J. Wenzel, A. Dreuw, I. Burghardt, *Physical Chemistry Chemical Physics* **2013**, *15*.

[147] J.-D. Chai, M. Head-Gordon, *Physical Chemistry Chemical Physics* **2008**, *10*.

[148] A. Schäfer, H. Horn, R. Ahlrichs, *The Journal of Chemical Physics* **1992**, *97*.

[149] A. Schäfer, C. Huber, R. Ahlrichs, *The Journal of Chemical Physics* **1994**, *100*.

[150] M. J. Frisch, G. W. Trucks, H. B. Schlegel, G. E. Scuseria, M. A. Robb, J. R. Cheeseman, G. Scalmani, V. Barone, B. Mennucci, G. A. Petersson, H. Nakatsuji, M. Caricato, X. Li, H. P. Hratchian, A. F. Izmaylov, J. Bloino, G. Zheng, J. L. Sonnenberg, M. Hada, M. Ehara, K. Toyota, R. Fukuda, J. Hasegawa, M. Ishida, T. Nakajima, Y. Honda, O. Kitao, H. Nakai, T. Vreven, J. A. Montgomery, Jr., J. E. Peralta, F. Ogliaro, M. Bearpark, J. J. Heyd, E. Brothers, K. N. Kudin, V. N. Staroverov, R. Kobayashi, J. Normand, K. Raghavachari, A. Rendell, J. C. Burant, S. S. Iyengar, J. Tomasi, M. Cossi, N. Rega, J. M. Millam, M. Klene, J. E. Knox, J. B. Cross, V. Bakken, C. Adamo, J. Jaramillo, R. Gomperts, R. E. Stratmann, O. Yazyev, A. J. Austin, R. Cammi, C. Pomelli, J. W. Ochterski, R. L. Martin, K. Morokuma, V. G. Zakrzewski, G. A. Voth, P. Salvador, J. J. Dannenberg, S. Dapprich, A. D. Daniels, Ö. Farkas, J. B. Foresman, J. V. Ortiz, J. Cioslowski, D. J. Fox, Gaussian09 Revision D.02.

[151] R. Ahlrichs, M. Bär, M. Häser, H. Horn, C. Kölmel, *Chemical Physics Letters* **1989**, *162*.

[152] T. Yanai, D. P. Tew, N. C. Handy, *Chemical Physics Letters* **2004**, *393*.

[153] H. Li, R. Nieman, A. J. A. Aquino, H. Lischka, S. Tretiak, *Journal of Chemical Theory and Computation* **2014**, *10*.

[154] F. Plasser, H. Lischka, *Journal of Chemical Theory and Computation* **2012**, *8*.

[155] F. Plasser, M. Wormit, A. Dreuw, *The Journal of Chemical Physics* **2014**, *141*.

[156] F. Plasser, S. A. Bäppler, M. Wormit, A. Dreuw, *The Journal of Chemical Physics* **2014**, *141*.

[157] R. L. Martin, *The Journal of Chemical Physics* **2003**, *118*.

[158] H. Tamura, I. Burghardt, M. Tsukada, *The Journal of Physical Chemistry C* **2011**, *115*.

[159] H. Tamura, I. Burghardt, *The Journal of Physical Chemistry C* **2013**, *117*.

[160] S. Mukamel, *Principles of nonlinear optical spectroscopy*, Oxford University Press on Demand, **1999**.

[161] F. Würthner, Z. Chen, F. J. M. Hoeben, P. Osswald, C.-C. You, P. Jonkheijm, J. v. Herrikhuyzen, A. P.H. J. Schenning, P. P.A. M. van der Schoot, E. W. Meijer, E. H. A. Beckers, S. C. J. Meskers, R. A. J. Janssen, *Journal of the American Chemical Society* **2004**, *126*.

[162] E. H. A. Beckers, S. C. J. Meskers, A. P.H. J. Schenning, Z. Chen, F. Würthner, P. Marsal, D. Beljonne, J. Cornil, R. A. J. Janssen, *Journal of the American Chemical Society* **2006**, *128*.

[163] B. Grévin, P.-O. Schwartz, L. Biniek, M. Brinkmann, N. Leclerc, E. Zaborova, S. Méry, *Beilstein Journal of Nanotechnology* **2016**, *7*.

[164] L. Liu, P. Eisenbrandt, T. Roland, M. Polkehn, P.-O. Schwartz, K. Bruchlos, B. Omiecienski, S. Ludwigs, N. Leclerc, E. Zaborova, J. Léonard, S. Méry, I. Burghardt, S. Haacke, *Physical Chemistry Chemical Physics* **2016**, *18*.

[165] C. C. Moser, J. M. Keske, K. Warncke, R. S. Farid, P. L. Dutton, *Nature* **1992**, *355*.

[166] R. Mauer, M. Kastler, F. Laquai, *Advanced Functional Materials* **2010**, *20*.

[167] O. G. Reid, R. D. Pensack, Y. Song, G. D. Scholes, G. Rumbles, *Chemistry of Materials* **2014**, *26*.

[168] A. De Sio, F. Troiani, M. Maiuri, J. Réhault, E. Sommer, J. Lim, S. F. Huelga, M. B. Plenio, C. A. Rozzi, G. Cerullo, E. Molinari, C. Lienau, *Nature Communications* **2016**, *7*.

[169] Y. Song, C. Hellmann, N. Stingelin, G. D. Scholes, *The Journal of Chemical Physics* **2015**, *142*.

[170] S. M. Falke, C. A. Rozzi, D. Brida, M. Maiuri, M. Amato, E. Sommer, A. De Sio, A. Rubio, G. Cerullo, E. Molinari, C. Lienau, *Science* **2014**, *344*.

[171] F. Harris, *Proceedings of the IEEE* **1978**, *66*.

[172] MATLAB, *version 9.0.0 (R2016b)*, The MathWorks Inc., Natick, Massachusetts, **2016**.

[173] R. D. Pensack, J. B. Asbury, *Journal of the American Chemical Society* **2009**, *131*.

[174] J. Guo, H. Ohkita, H. Benten, S. Ito, *Journal of the American Chemical Society* **2010**, *132*.

[175] S. Gelinas, A. Rao, A. Kumar, S. L. Smith, A. W. Chin, J. Clark, T. S. van der Poll, G. C. Bazan, R. H. Friend, *Science* **2014**, *343*.

[176] W. Domcke, D. R. Yarkony, H. Köppel, *Conical Intersections: Theory, Computation and Experiment*, WORLD SCIENTIFIC, **2011**.

[177] I. Burghardt, E. R. Bittner, H. Tamura, A. Pereverzev, J. G. S. Ramon in *Energy Transfer Dynamics in Biomaterial Systems*, *Vol. 93*, (Eds.: I. Burghardt, V. May, D. A. Micha, E. R. Bittner), Springer Berlin Heidelberg, Berlin, Heidelberg, **2009**.

[178] S. O. Nielsen, C. F. Lopez, G. Srinivas, M. L. Klein, *Journal of Physics: Condensed Matter* **2004**, *16*.

[179] J. Nelson, J. J. Kwiatkowski, J. Kirkpatrick, J. M. Frost, *Accounts of Chemical Research* **2009**, *42*.

[180] R. G. E. Kimber, E. N. Wright, S. E. J. OKane, A. B. Walker, J. C. Blakesley, *Physical Review B* **2012**, *86*.

[181] M. C. Heiber, PhD thesis, University of Akron, **2012**.

[182] N. Metropolis, A. W. Rosenbluth, M. N. Rosenbluth, A. H. Teller, E. Teller, *The Journal of Chemical Physics* **1953**, *21*.

[183] A. Miller, E. Abrahams, *Physical Review* **1960**, *120*.

[184] C. Deibel, D. Mack, J. Gorenflot, A. Schöll, S. Krause, F. Reinert, D. Rauh, V. Dyakonov, *Physical Review B* **2010**, *81*.

[185] V. Vaissier, P. Barnes, J. Kirkpatrick, J. Nelson, *Physical Chemistry Chemical Physics* **2013**, *15*.

[186] J. J. Kwiatkowski, J. Nelson, H. Li, J. L. Bredas, W. Wenzel, C. Lennartz, *Physical Chemistry Chemical Physics* **2008**, *10*.

[187] D. P. McMahon, A. Troisi, *The Journal of Physical Chemistry Letters* **2010**, *1*.

[188] A. Pershin, S. Donets, S. A. Baeurle, *The Journal of Chemical Physics* **2012**, *136*.

[189] H. Bässler, *physica status solidi (b)* **1993**, *175*.

[190] A. K. Tripathi, Ashish, Y. Mohapatra, *Organic Electronics* **2010**, *11*.

[191] W. Humphrey, A. Dalke, K. Schulten, *Journal of Molecular Graphics* **1996**, *14*.

[192] H. Oevering, M. N. Paddon-Row, M. Heppener, A. M. Oliver, E. Cotsaris, J. W. Verhoeven, N. S. Hush, *Journal of the American Chemical Society* **1987**, *109*.

[193] D. A. Vithanage, A. Devižis, V. Abramavičius, Y. Infahsaeng, D. Abramavičius, R. C. I. MacKenzie, P. E. Keivanidis, A. Yartsev, D. Hertel, J. Nelson, V. Sundström, V. Gulbinas, *Nature Communications* **2013**, *4*.

[194] M. M. Mandoc, L. J. A. Koster, P. W. M. Blom, *Applied Physics Letters* **2007**, *90*.

[195] S. Zhou, J.-x. Sun, *Optik - International Journal for Light and Electron Optics* **2015**, *126*.

[196] C. G. Shuttle, A. Maurano, R. Hamilton, B. O'Regan, J. C. de Mello, J. R. Durrant, *Applied Physics Letters* **2008**, *93*.

[197] C. G. Shuttle, B. O'Regan, A. M. Ballantyne, J. Nelson, D. D. C. Bradley, J. R. Durrant, *Physical Review B* **2008**, *78*.

[198] F. Gao, Y. Zhao, W. Liang, *The Journal of Physical Chemistry B* **2011**, *115*.

[199] A. A. Voityuk, N. Rösch, *The Journal of Chemical Physics* **2002**, *117*.

[200] A. A. Voityuk, *Chemical Physics Letters* **2008**, *451*.

[201] I. Cabeza de Vaca, S. Acebes, V. Guallar, *Journal of Computational Chemistry* **2016**, *37*.

Scientific Contributions

Publications

- R. Binder, M. Polkehn, T. Ma, and I. Burghardt, "*Ultrafast exciton migration in an HJ-aggregate: Potential surfaces and quantum dynamics*", Chem. Phys. (Special Issue L. S. Cederbaum), **2017**, 482, 16

- L. Liu, P. Eisenbrandt, Th. Roland, M. Polkehn, P.-O. Schwartz, K. Bruchlos, B. Omiecienski, S. Ludwigs, N. Leclerc, E. Zaborova, J. Leonard, S. Méry, I. Burghardt, S. Haacke, "*Controlling charge separation and recombination by chemical design in donor-acceptor dyads*", Phys. Chem. Chem. Phys., **2016**, 18, 18536

- M. Polkehn, H. Tamura, P. Eisenbrandt, S. Haacke, S. Méry, I. Burghardt, "*Molecular packing determines charge separation in a liquid crystalline bisthiophene-perylene diimide donor-acceptor material*", J. Phys. Chem. Lett, **2016**, 7, 1327

- M. Polkehn, P. Eisenbrandt, H. Tamura, S. Haacke, S. Méry, I. Burghardt, "*Ultrafast excitonic and charge transfer dynamics in nanostructured organic polymer materials*", Proc. SPIE 9884, Nanophotonics IV, **2016**, 98840O

- A. Dreuw, M. Polkehn, R. Binder, A. Heckel, S. Knippenberg, "*Computational design of improved two-photon active caging compounds based on nitrodibenzofuran*", J. Comp. Chem., **2012**, 33, 1797

Poster Presentations

- "*Exciton Dissociation in Ordered Donor-Acceptor Assemblies*", 7th International Conference on Molecular Electronics Strasbourg/France, **2014**
- "*Exciton Dissociation in Ordered Donor-Acceptor Assemblies*", 12th Femtochemistry Conference Hamburg/Germany, **2015**
- "*Electronic Structure and Quantum Dynamics of an Oligothiophene H-Aggregate*", Quantum Dynamics - From Algorithms to Applications Greifswald/Germany, **2016**

Oral Presentations

- Annual external Seminar of the PTC-Institute, Kleinwalsertal (Austria), **2017**
- Weekly seminar of the Institute of Physical and Theoretical Chemistry, Goethe University, **2016**
- Internal group seminar, Goethe University, **2015**
- Progress report of DFG/ANR project MolNanoMat BU-1032-2, Strasbourg University (France), **2014**
- Internal group seminar, Goethe University, **2013**

Eidesstattliche Erklärung

Ich versichere an Eides statt durch meine eigene Unterschrift, dass ich die vorstehende Arbeit selbständig und ohne fremde Hilfe angefertigt und alle Stellen, die wörtlich oder annähernd wörtlich aus Veröffentlichungen genommen sind, als solche kenntlich gemacht habe. Die Versicherung bezieht sich auch auf in der Arbeit gelieferte Zeichnungen, Skizzen, bildliche Darstellungen und dergleichen.

Ort, Datum	Unterschrift